Molecular Cell

Resource

Rapid UPF1 depletion illuminates the temporal dynamics of the NMD-regulated human transcriptome

Graphical abstract

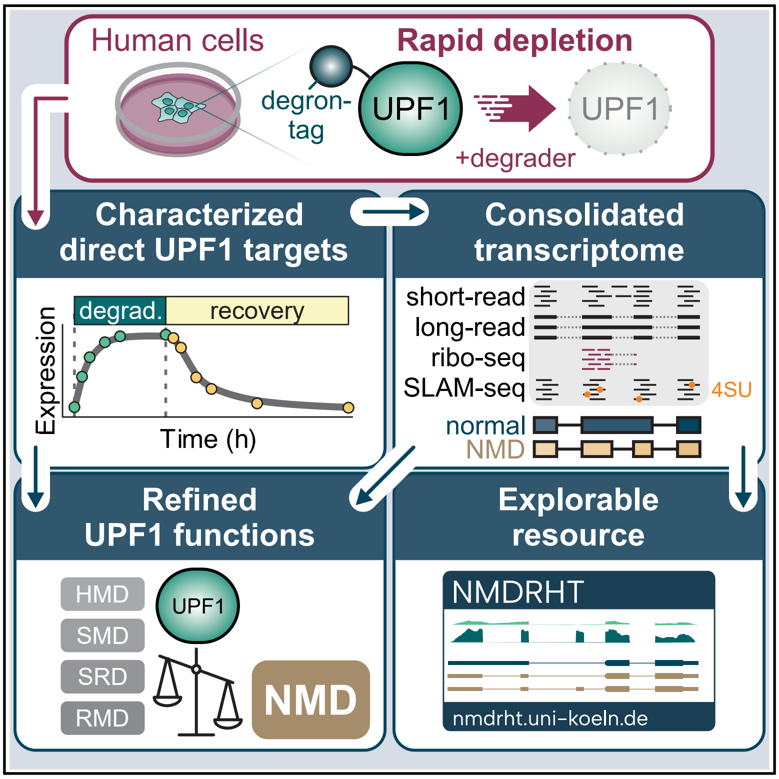

Highlights

- Rapid UPF1 depletion identifies direct targets of nonsense-mediated decay (NMD)
- Combined transcriptomics define an atlas of human NMD-sensitive transcripts
- Alternative splicing is a key driver of NMD-targeted transcript diversity
- Explorable NMD transcriptome resource is available at nmdrht.uni-koeln.de

Authors

Volker Boehm, Damaris Wallmeroth, Paul O. Wulf, ..., Philipp Mertins, Markus Landthaler, Niels H. Gehring

Correspondence

markus.landthaler@mdc-berlin.de (M.L.), ngehring@uni-koeln.de (N.H.G.)

In brief

UPF1 depletion inhibits nonsense-mediated mRNA decay (NMD) and stabilizes direct target transcripts within hours. Boehm et al. use conditional protein degradation and advanced transcriptomics to map the NMD-regulated human transcriptome, highlighting alternative splicing as a major NMD-activating mechanism.

Boehm et al., 2025, Molecular Cell *85*, 1–23
September 18, 2025 © 2025 The Authors. Published by Elsevier Inc.
https://doi.org/10.1016/j.molcel.2025.08.015

CellPress

Please cite this article in press as: Boehm et al., Rapid UPF1 depletion illuminates the temporal dynamics of the NMD-regulated human transcriptome, Molecular Cell (2025), https://doi.org/10.1016/j.molcel.2025.08.015

Molecular Cell

CellPress
OPEN ACCESS

Resource

Rapid UPF1 depletion illuminates the temporal dynamics of the NMD-regulated human transcriptome

Volker Boehm,[1,2] Damaris Wallmeroth,[1,2] Paul O. Wulf,[3] Oliver Popp,[4] Luiz Gustavo Teixeira Alves,[3] Lucie Reinecke,[3] Maximilian Riedel,[3] Emanuel Wyler,[3] Marek Franitza,[5] Kerstin Becker,[5] Karina Polkovnychenko,[1,2] Simone Del Giudice,[3] Nouhad Benlasfer,[3] Philipp Mertins,[4,6] Markus Landthaler,[3,7,*] and Niels H. Gehring[1,2,8,*]

[1]Institute for Genetics, University of Cologne, 50674 Cologne, Germany
[2]Center for Molecular Medicine Cologne (CMMC), University of Cologne, 50937 Cologne, Germany
[3]Max Delbrück Center for Molecular Medicine in the Helmholtz Association (MDC), Berlin Institute for Medical Systems Biology, Berlin, Germany
[4]Max-Delbrück-Center for Molecular Medicine, Berlin, Germany
[5]Cologne Center for Genomics (CCG), Medical Faculty, University of Cologne, 50931 Cologne, Germany
[6]Berlin Institute of Health@Charite, Berlin, Germany
[7]Institute of Biology, Humboldt-Universität zu Berlin, Berlin, Germany
[8]Lead contact
*Correspondence: markus.landthaler@mdc-berlin.de (M.L.), ngehring@uni-koeln.de (N.H.G.)

https://doi.org/10.1016/j.molcel.2025.08.015

SUMMARY

The RNA helicase UPF1 shapes the transcriptome as the core factor of nonsense-mediated mRNA decay (NMD). The essential role of UPF1 in human cells has impeded efforts to delineate its directly regulated transcripts and molecular function. To investigate the effects of rapid UPF1 depletion, we engineered human cell lines with endogenous UPF1 fused to conditional degron tags. Temporal-resolution transcriptomic analyses identified direct target mRNAs, consisting predominantly of NMD substrates that are mostly stabilized within hours of UPF1 depletion. By integrating long-read sequencing and ribosome profiling data, we defined the consolidated NMD-regulated human transcriptome (NMDRHT), uncovering previously unannotated transcripts and establishing alternative splicing as a major contributor of NMD-targeted mRNAs. Additionally, we identified non-canonical NMD events that lack indication of being driven by other UPF1-dependent degradation routes. Our work refines the role of the post-transcriptional regulator UPF1 and introduces an experimentally validated NMD-regulated transcriptome as a navigable resource at https://nmdrht.uni-koeln.de.

INTRODUCTION

Quality control mechanisms continuously monitor the transcriptome in eukaryotic cells to ensure the expression of correct gene products.[1] Translation-coupled surveillance pathways are particularly important,[2] as they eliminate aberrant transcripts that have escaped previous checkpoints. Nonsense-mediated decay (NMD) is a translation-coupled process that targets mRNAs harboring premature termination codons (PTCs).[3] PTCs introduced by mutations may cause genetic disorders,[4] as they halt protein synthesis prematurely, resulting in the production of potentially dysfunctional or toxic C-terminally truncated proteins.[5,6] NMD ensures that mRNAs containing PTCs are promptly eliminated to prevent the accumulation of detrimental proteins.[7]

In mammalian cells, PTCs are recognized through the exon junction complex (EJC). EJCs are multiprotein complexes formed during pre-mRNA splicing that demarcate exon boundaries.[8–10] When a ribosome terminates more than 50 nucleotides (nt) upstream of the last exon-exon junction, the downstream EJC initiates the assembly of NMD complexes.[11–13] This 50-nt rule[14] is used to annotate transcript isoforms as biotype "NMD" in reference databases such as Ensembl and GENCODE.[15,16] The EJC's capacity to activate NMD explains the tendency for regular stop codons to be predominantly located in the final exon.

The widespread use of alternative splicing (AS) by mammalian cells, while expanding the coding potential of the genome,[17,18] concurrently becomes a significant source of NMD substrates.[19–23] For example, AS events that alter the reading frame frequently result in "unproductive" transcripts harboring PTCs.[24] Additionally, regulated inclusion of PTC-encoding exons ("poison exons") contributes to the AS coupled to NMD (AS-NMD).[25] Therefore, NMD is not only a quality control but also a general gene expression regulatory mechanism. Consequently, alternatively spliced mRNAs constitute a large portion of endogenous NMD substrates.[26,27] Other NMD substrates include mRNAs with long 3′ UTRs, upstream open reading frames

(ORFs), and 3′ UTR introns.[28] While often NMD is triggered by an EJC, it is not required for long 3′ UTR NMD.[29,30]

Prematurely terminating ribosomes activate NMD complex formation centered around the key NMD factor UPF1.[31] NMD activation immobilizes the RNA-dependent helicase UPF1 in the vicinity of the termination codon. Subsequently, the kinase SMG1 phosphorylates multiple SQ or TQ motifs in the unstructured N- and C-terminal regions of UPF1.[32] Phosphorylated UPF1 then recruits the heterodimer SMG5 and SMG7, enabling SMG6 to endonucleolytically cleave the mRNA in close proximity to the PTC.[26,33–37]

The NMD core machinery, including UPF1, is required for proper embryogenesis and development of many model organisms.[38–43] A meta-analysis identified UPF1 in a core set of 188 common essential genes in mice, human cell culture, and the human population.[44] Moreover, the Cancer Dependency Map (DepMap) classifies UPF1 as “common essential” across >1,000 cancer cell lines.[45–50]

UPF1 also participates in other mRNA degradation pathways,[51,52] including Staufen (STAU)-mediated mRNA decay (SMD), replication-dependent histone mRNA decay (HMD), glucocorticoid-induced mRNA decay (GMD), and structure-mediated mRNA decay (SRD).[53–56] In these degradation pathways, UPF1 is recruited to target transcripts by interactions with various RNA-binding proteins.[51,52] Apart from SMD, for which biochemical insights exist,[57] UPF1’s mechanistic role in other pathways remains unclear.

Despite extensive study, UPF1’s essentiality limits experimental analysis in mammalian cells. Here, we employ auxin- and degradation tag (dTAG)-degron-mediated rapid depletion of UPF1 protein in human cells to characterize the UPF1-regulated transcriptome. UPF1 degradation resulted in strong NMD inhibition within 12 h of treatment, surpassing the effects of long-term knockdowns (KDs). Directly targeted mRNAs were identified by temporally resolved transcriptomics complemented by metabolic labeling data. Comprehensive transcriptome assembly and read-to-transcript aware quantification confirmed UPF1’s primary role in regulating NMD-targeted transcripts. Notably, UPF1 depletion had no detectable effect on replication-dependent HMD. At the proteome level, we detected NMD-transcript-encoded proteins/peptides with potentially lost or altered functionality. These data illustrate that acute degradation enables high-resolution analyses of RNA decay and gene expression regulation. The transcriptomic data can be interactively explored at https://nmdrht.uni-koeln.de.

RESULTS

The RNA helicase UPF1 monitors the transcriptome by non-specifically binding to mRNAs,[58–60] dissociating from non-target transcripts,[61] and initiating degradation of target RNAs via diverse pathways such as NMD (Figures 1A and S1A). Loss of function of UPF1 and several other NMD and EJC factors is not tolerated in cancer cells or the human population (Figure S1B).[47,62] This renders studies of UPF1 challenging, as conventional CRISPR-Cas9 knockout (KO) results in lethality. Therefore, RNA interference-based KD is commonly used to transiently deplete UPF1 protein (Figure 1B) and inactivate NMD. However, prolonged KD often causes reduced proliferation, cell cycle arrest, or apoptosis.[63–66]

We compared UPF1-KD (Figure 1B) with the combined SMG6 and SMG7 downregulation, which strongly inhibits NMD activity.[26,67–69] UPF1 was downregulated in human embryonic kidney cells (HEK293) and the colon cancer cell line HCT116 using either an established small interfering RNA (siRNA)[70] or a high complexity siRNA pool (siPOOL) to minimize off-target effects[71] (Figures 1C and S1C). We observed stronger accumulation of the alternatively spliced NMD-target SRSF2[72] and NMD-sensitive long non-coding RNAs (lncRNAs) ZFAS1 and GAS5[73] in SMG6 + SMG7-KD cells compared with either UPF1-KD (Figures 1C and S1C). Despite strongly reduced UPF1 levels, residual UPF1 appears to sustain partial NMD activity, particularly at early time points. This aligns with published mass spectrometry data[74,75] indicating high UPF1 abundance and a long half-life ($T1/2 \geq 48$ h) in human tissues (Figures S1D and S1E). By contrast, SMG6 and SMG7 are less abundant and degrade faster, explaining the quicker NMD inhibition following their KD.

Characterizing conditional degron systems for rapid and functional UPF1 depletion

Given the lethality of UPF1-KO and the moderate effects of UPF1-KDs, we explored conditional degradation systems for selective UPF1 protein depletion. We utilized the auxin-inducible degron (AID) system to conditionally degrade UPF1 in HCT116 cells,[76] which express *At*AFB2 from the AAVS1 locus.[77] The cells were engineered with an N-terminal or C-terminal V5-AID-tag at the UPF1 locus (Figure 1D; Table S1).

Following treatment with 500 μM indole-3-acetic acid (IAA) for various time points, RNA sequencing (RNA-seq) revealed a time-dependent accumulation of differentially regulated transcripts in AID-tagged cells, but not in control cells (Figure S1F). We selected the N-terminally AID-tagged cell line for subsequent experiments, since it consistently showed stronger effects (Figure S1F). Proteomic analyses confirmed efficient UPF1 depletion after 6–24 h of IAA treatment (Figures S1G and S1H), with minimal effects on other NMD/EJC/SMD factors (Figures 1E and S1I). Thus, UPF1 degron cells enable rapid, specific, and time-resolved UPF1 depletion with minimal off-target effects.

Next, we performed an extended UPF1 depletion time course up to 48 h, including an early 2-h time point (Figure S1J). Western blot confirmed UPF1 depletion by 2 h post-IAA treatment (Figure 1F), and selected NMD-sensitive transcripts accumulated over time with seemingly different kinetics (Figure 1F). These variations likely reflect differences in transcription, processing, and translation rates, and/or NMD efficiency, highlighting the inherent heterogeneity of NMD-sensitive transcripts.

We utilized the reversibility of the AID system[76] for studying transcripts recovering from NMD inhibition. We removed IAA after 24-h treatment and recovered over 48 h (Figure S1J). UPF1 protein returned to control levels within 24–48 h of IAA withdrawal (Figure 1G), and accumulated NMD targets gradually normalized over time following UPF1 recovery (Figure 1G).

To assess the broader applicability of UPF1 depletion, we tested a different conditional degron tag, dTAG ($FKBP12^{F36V}$),[78] in HCT116 and HEK293 cells (Figure S1K). Following 12 h of

Please cite this article in press as: Boehm et al., Rapid UPF1 depletion illuminates the temporal dynamics of the NMD-regulated human transcriptome, Molecular Cell (2025), https://doi.org/10.1016/j.molcel.2025.08.015

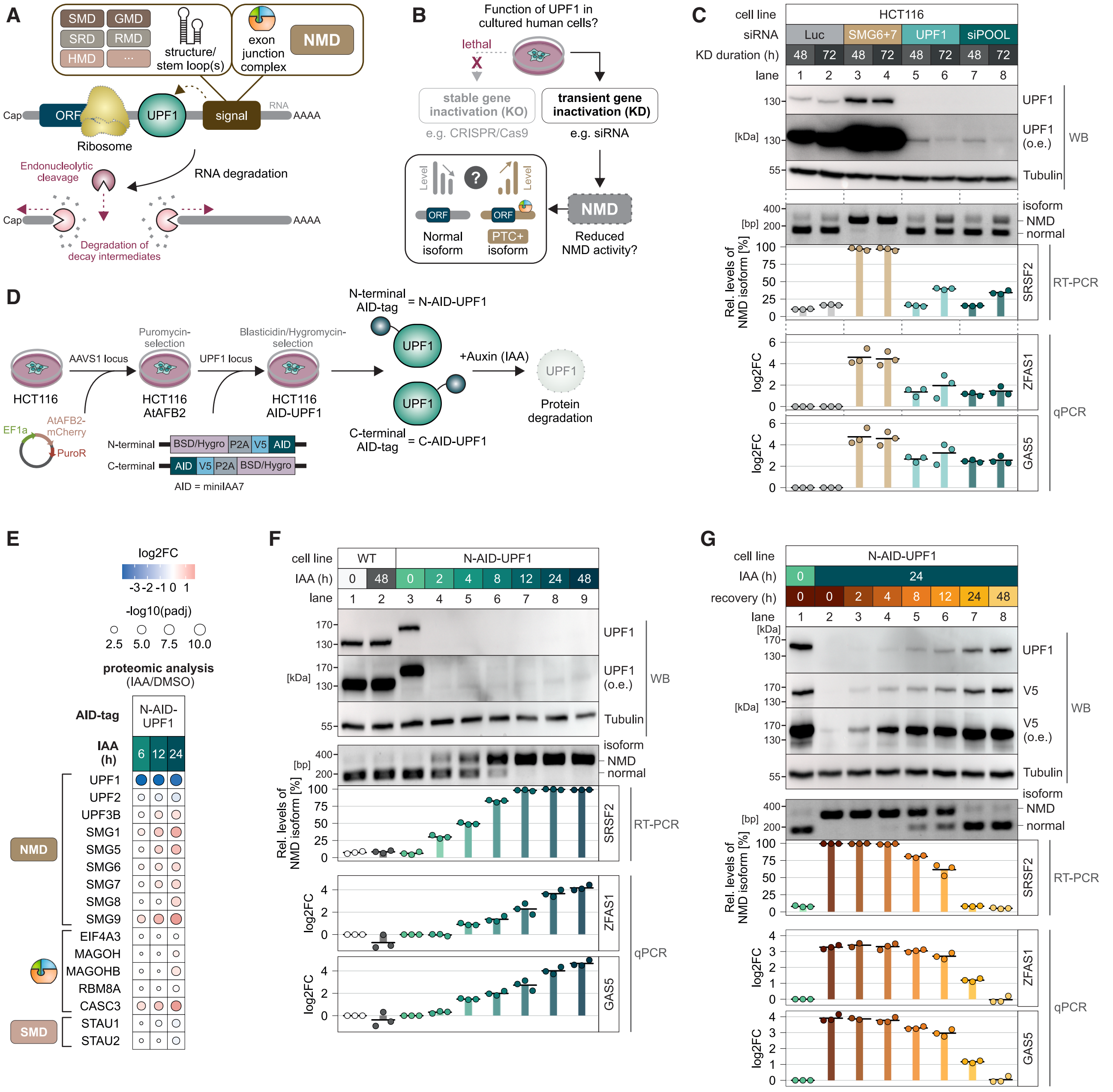

Figure 1. Rapid depletion of UPF1 via the AID system inhibits NMD

(A) Overview of UPF1-mediated RNA degradation pathways activated by signals (e.g., stem loops and EJC) in the 3′ UTR.

(B) Workflow for studying UPF1 in human cells.

(C) (Top) Western blot of UPF1 protein after siRNA KD in HCT116 cells, and tubulin serves as a loading control; o.e., overexposure. (Middle) End-point quantitative reverse-transcription PCR (RT-qPCR) of SRSF2: relative levels of SRSF2 isoforms were quantified. (Bottom) qPCR of NMD targets ZFAS1 and GAS5, shown as $\log_2$ fold change ($\log_2$FC). Individual data points and mean (bars) are shown (*n* = 3).

(D) Cell line generation for auxin-inducible (indole-3-acetic acid [IAA]) UPF1 depletion.

(E) Mass spectrometry of NMD/EJC/SMD proteins in cells ± IAA.

(F) Western blot, RT-qPCR, and qPCR analyses of N-terminal AID-tagged UPF1 HCT116 cell lines treated with 500 μM IAA for the indicated time (visualized as in C).

(G) Western blot, RT-qPCR, and qPCR analyses of N-terminal AID-tagged UPF1 HCT116 cell lines treated with 500 μM IAA for the indicated time and incubated for the recovery time without auxin (visualized as in C). V5-AID-tagged UPF1 was also detected via V5 antibodies.

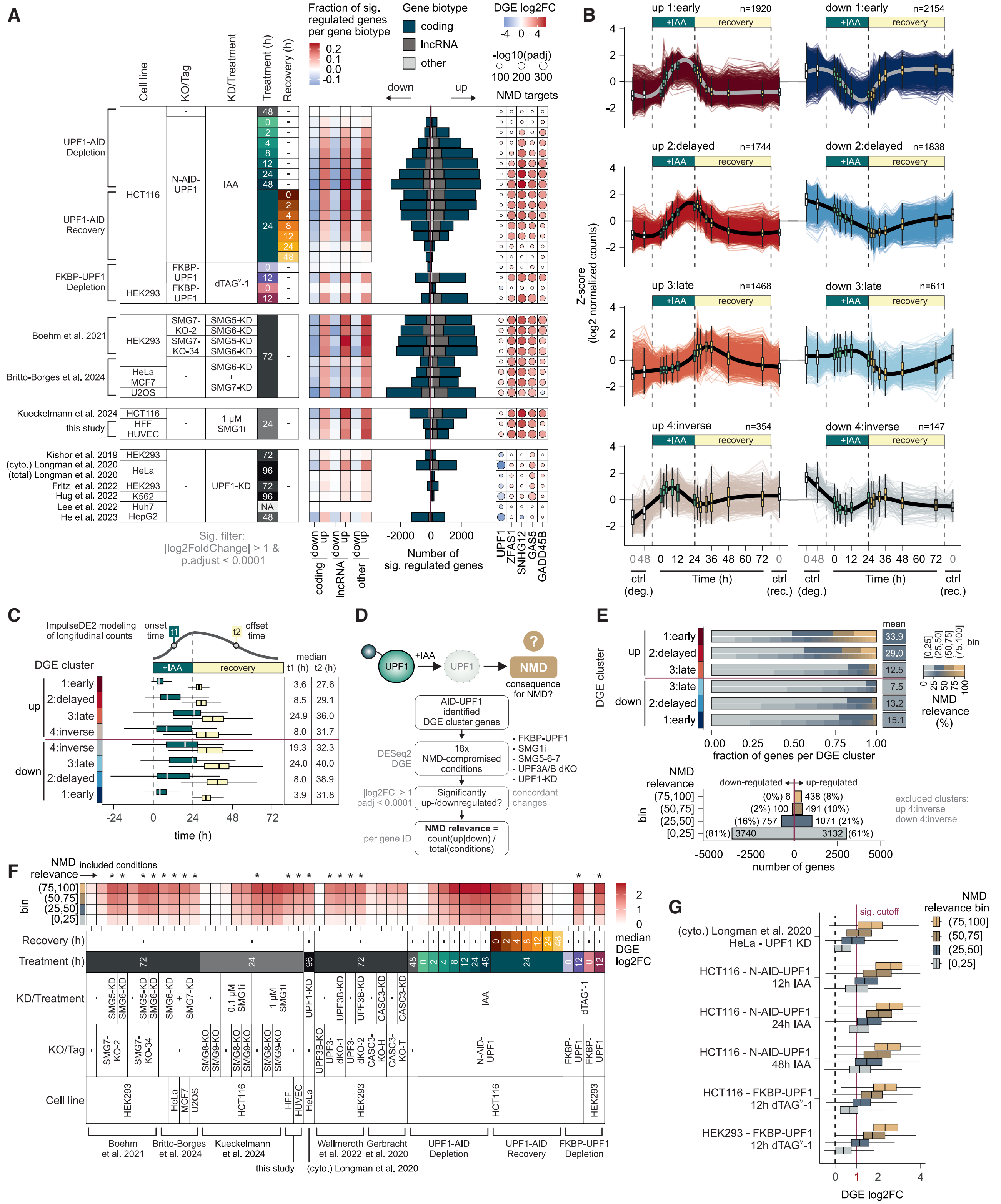

(legend on next page)

Please cite this article in press as: Boehm et al., Rapid UPF1 depletion illuminates the temporal dynamics of the NMD-regulated human transcriptome, Molecular Cell (2025), https://doi.org/10.1016/j.molcel.2025.08.015

dTAG^V-1 treatment, which recruits the von Hippel-Lindau (VHL) E3 ligase complex,[79] UPF1 was efficiently depleted (Figure S1L), and NMD-sensitive transcripts (SRSF2, ZFAS1, and GAS5) accumulated strongly (Figure S1L). Thus, both AID and dTAG systems allow for the efficient and specific depletion of UPF1, effectively inhibiting NMD.

Directly UPF1-regulated genes are enriched for NMD targets

To investigate transcriptome-wide changes upon UPF1 depletion, we performed deep mRNA-seq of the AID-mediated degradation and recovery time course samples and dTAG conditions (Figures S1J and S2A). Differential gene expression (DGE) analysis revealed pronounced UPF1- and time-dependent changes in thousands of genes across all GENCODE-annotated biotypes, including the accumulation of known NMD targets[80] (Figure 2A). After 12 h of UPF1 depletion, DGE effects were comparable to or stronger than those observed in severe NMD-inhibited conditions, such as SMG5/SMG6/SMG7 downregulation in various cell lines[26,69] or SMG1i inhibitor (SMG1i)[81] treatment of human foreskin fibroblast (HFF), human umbilical vein endothelial cells (HUVECs), or HCT116 cells[82] (Figure 2A; Table S2). By contrast, recently published RNA-seq datasets of UPF1-KD exhibited generally fewer and weaker gene expression changes,[83–88] except for the dataset with the strongest reduction of UPF1 mRNA levels.[84] Collectively, rapid UPF1 depletion via conditional degron tags outperforms RNA interference approaches and elicits strong transcriptome-wide effects.

Using the AID-UPF1 degradation and recovery time course, we aimed to distinguish direct UPF1-dependent consequences from indirect secondary effects.[89] Principal component analysis revealed that the most pronounced changes occur within the first 12 h of AID-UPF1 depletion or recovery (Figure S2B), suggesting that immediate UPF1-dependent effects predominantly arise during this time. To test this hypothesis, we performed hierarchical clustering of genes that were significantly up- or downregulated at least at one time point compared with the respective control condition. We identified four distinct clusters, categorized by their expression patterns as “early,” “delayed,” “late,” and “inverse” (Figures 2B and S2C). Most significantly altered genes clustered as early or delayed, mirroring profiles of previously analyzed targets such as SRSF2 (early) and GAS5/ZFAS1 (delayed) (Figures 1F, 1G, and 2B). By contrast, genes in the inverse clusters showed mis-regulation at 0 h IAA treatment, suggesting clone-specific variation due to genetic drift during clone selection (Figure 2B). Consequently, we excluded these clusters from subsequent analyses.

To validate the cluster classification, we applied ImpulseDE2 to model RNA-seq counts for each gene.[90] Most genes showed a transient (impulse model) expression pattern, confirming the reversibility of their expression changes[91] (Figures S2D and S2E). We extracted onset (t1) and offset (t2) times for each gene (Figure S2D) and re-evaluated the clusters. Onset times closely matched our previous classification, especially for the early ($\tilde{x}$ = 3.6 h), delayed ($\tilde{x}$ = 8.5 h), and late ($\tilde{x}$ = 24.9 h) upregulated clusters (Figure 2C). Early and delayed clusters exhibited similar short offset times ($\tilde{x}$ = 27.6 and 29.1 h), suggesting their rapid degradation by recovering UPF1. In conclusion, genes in the early and delayed upregulated clusters are likely direct UPF1 targets, while secondary effects presumably drive late cluster genes.

As UPF1 is the central component of the NMD machinery, we expected numerous bona fide NMD targets among the upregulated classified cluster genes. Due to the lack of a ground truth for NMD-targeted transcripts, we assessed “NMD relevance” empirically by examining significant regulation across 18 strongly NMD-inhibited RNA-seq conditions (Figure 2D). Genes in the upregulated early and delayed clusters showed higher NMD relevance, while the late and downregulated clusters scored lower (Figure 2E). 61% of UPF1-dependent upregulated genes showed low NMD relevance (Figure 2E). However, we observed generally lower effect strengths in the low NMD relevance bin (Figure 2F), suggesting that those apparently NMD-irrelevant genes exhibit weak gene expression changes. To test this, we analyzed the strongest UPF1-KD dataset,[84] and the FKBP-UPF1 depletion conditions. Most low NMD relevance genes fall below our standard cutoff ($\log_2$ fold change [$\log_2$FC] < 1) (Figure 2G), whereas high NMD relevance genes exhibited the strongest expression changes across conditions (Figure 2G).

To validate our NMD-related findings, we used two datasets: (1) NMD factor KD/rescue meta-analysis[67] and (2) phospho-UPF1-enriched RNA immunoprecipitation sequencing (RIP-seq).[92] Early and delayed upregulated clusters and high NMD relevance genes were enriched in both datasets (Figures S2F and S2G). We conclude that the rapid and pronounced

Figure 2. Identification and characterization of UPF1-regulated genes

(A) (Left) Comparison of multiple RNA-seq data regarding the fraction of significantly differentially expressed genes (separated by up-/downregulation) versus all detected genes per GENCODE biotype. (Middle) Absolute number of significantly regulated genes stratified by GENCODE biotype. (Right) Expression changes of UPF1 or individual NMD-target genes.

(B) Z-scaled $\log_2$-transformed gene-level counts of combined degradation and recovery N-AID-UPF1 RNA-seq data over IAA treatment/recovery time. Control samples are shown at the terminal ends of the *x* axis. Upregulated (left column) or downregulated (right column) clusters after hierarchical clustering (k = 4) are depicted.

(C) Boxplot of modeled onset (t1) and offset (t2) time parameters for differential gene expression (DGE) cluster genes (outliers are not displayed).

(D) Workflow for NMD relevance assignment of DGE cluster genes.

(E) (Top) NMD relevance as a fraction of genes per DGE cluster, depicted as binned (upper bars) or absolute percentage (lower bars). (Bottom) Absolute number of genes per binned NMD relevance, separated by up-/downregulation. Inverse clusters were excluded.

(F) Median $\log_2$FC of upregulated DGE cluster genes (excluding inverse cluster) per NMD relevance bin in RNA-seq datasets. Asterisks designate the 18 conditions included for NMD relevance determination.

(G) Boxplot of $\log_2$FC of upregulated DGE cluster genes (excluding inverse cluster) of UPF1-depleted RNA-seq conditions, stratified by NMD relevance bin. The default significance cutoff ($\log_2$FC > 1) is shown, and outliers of the boxplot are not displayed.

Please cite this article in press as: Boehm et al., Rapid UPF1 depletion illuminates the temporal dynamics of the NMD-regulated human transcriptome, Molecular Cell (2025), https://doi.org/10.1016/j.molcel.2025.08.015

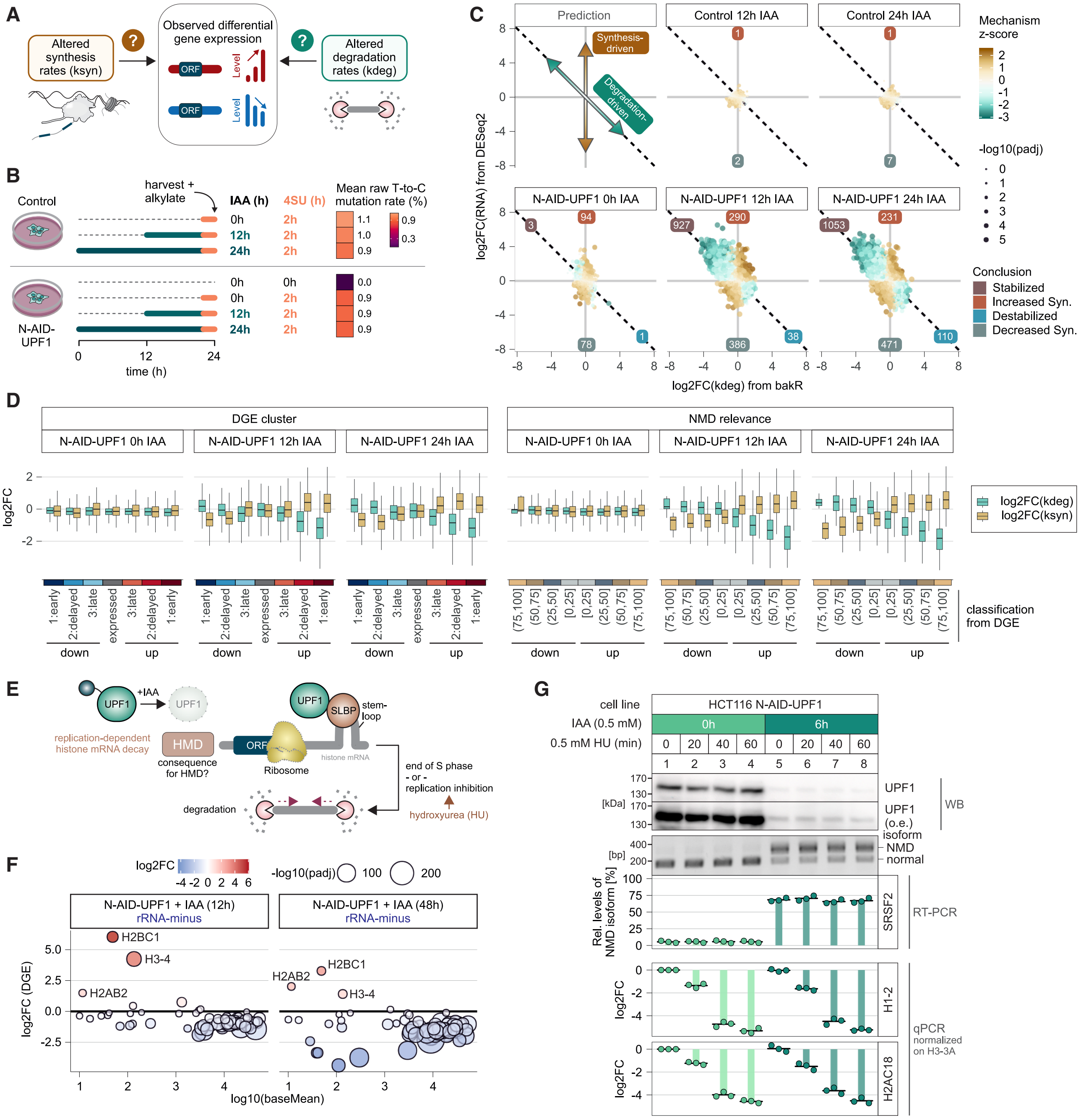

Figure 3. UPF1 destabilizes target mRNAs and is not required for HMD

(A) Model of mechanism for gene expression changes upon UPF1 depletion.

(B) Labeling strategy for SLAM-seq of control or N-AID-UPF1 HCT116 cells with 4-thiouridine (4SU). Mean raw T-to-C mutation rates are shown.

(C) Mechanistic dissection of SLAM-seq data by integrating the detected changes in RNA levels (log$_2$FC(RNA) by DESeq2) and degradation rate (log$_2$(kdeg) by bakR) in each condition compared with control 0 h IAA HCT116 cells. The size of points indicates the statistical significance of mechanism scores, and the mechanism score *Z* score (fill color) indicates degradation-driven (negative values) or synthesis-driven (positive values) expression changes. Conclusions are based on parameters defined in the STAR Methods section.

(D) Boxplot of log$_2$FC of differential degradation (kdeg) or synthesis (ksyn) rate constants per DGE clusters (left) or NMD relevance bins (right), stratified by DGE up-/downregulation. Outliers of the boxplot are not displayed.

(E) Scheme of UPF1's role in replication-dependent HMD.

(legend continued on next page)

upregulation of transcripts upon UPF1 depletion correlated with greater NMD relevance, supporting the critical role of UPF1 in NMD.

Transcriptome changes in UPF1-depleted cells result from mRNA stabilization

To explain the temporal clustering of UPF1-regulated transcripts, we considered RNA metabolism parameters such as synthesis, processing, and degradation rates. Using data from HEK293 cells,[93] we observed that upregulated gene clusters, particularly early genes, exhibited higher degradation rates and reduced cytoplasmic accumulation (Figure S3A), suggesting that UPF1 promotes the degradation of its direct targets.

To further characterize direct UPF1 targets, we performed thiol(SH)-linked alkylation for the metabolic sequencing of RNA (SLAM-seq) of control and AID-UPF1 cells at 0, 12, and 24 h of IAA treatment with 4-thiouridine (4SU) labeling (Figures 3A and 3B).[94] T-to-C conversion rates were consistent (≈1%), allowing analysis using bakR (Figure 3B).[95,96] By calculating $\log_2$FCs in the degradation rate constant [$\log_2$FC(k_{deg})], combined with differential RNA expression level analysis from DESeq2 [$\log_2$FC (RNA)], we classified genes as either synthesis-driven or degradation-driven (Figure 3C). UPF1 depletion resulted in transcript stabilization in 927 and 1,053 genes at 12 and 24 h, respectively (Figure 3C). Of note, IAA treatment for 12 and 24 h also resulted in synthesis-driven expression changes of about 700 genes. Gene Ontology analyses at 12 h revealed downregulation of energy/respiration-related genes and increased expression of stress- and metabolism-related genes (Figure S3B), suggesting that transcriptional responses contribute to the altered transcriptome. Integrating SLAM-seq results with DGE clustering and NMD relevance bins showed that the upregulated early and delayed clusters, as well as the upregulated high NMD relevance genes, have reduced degradation rates (Figure 3D). These results confirm that UPF1 actively promotes the destabilization of direct NMD-sensitive target transcripts.

Given the translation-dependent nature of UPF1-dependent mRNA degradation,[52] we next examined the translatome of untreated or 12 h UPF1-depleted cells by Ribo-seq. Ribo-seQC[97] analysis showed that reads primarily mapped to annotated coding sequence (CDS) with a 3-nt periodicity and 75% reading frame preference (Figure S3C). Genes with significant changes upon UPF1 depletion were mostly upregulated in both Ribo-seq and mRNA-seq, as well as stabilized (Figures S3D and S3E). Accordingly, ribosome occupancy increased for the upregulated early and delayed clusters and high NMD relevance genes (Figure S3F), supporting the predominantly translation-dependent mechanism of regulation by UPF1.

Lack of evidence for a major role of UPF1 in HMD

UPF1 has been implicated in multiple decay pathways, including replication-dependent HMD (Figure 3E).[56] These histone mRNAs lack poly(A) tails and undergo rapid degradation at the end of the S phase (Figure 3E). They were underrepresented in our previous UPF1-depleted RNA-seq datasets that were generated using poly(A)-selected library preparation (Figure S3G). Therefore, we re-sequenced rRNA-depleted RNA from N-AID-UPF1 cells, allowing the detection of 73 out of 118 HUGO Gene Nomenclature Committee (HGNC)-annotated histone genes (Figure S3G). Of these mRNAs, only three were significantly upregulated (H2BC1, H2AB2, and H3-4) after 12 or 48 h of UPF1 depletion (Figure 3F), while most histone genes showed reduced expression, suggesting cell cycle alterations[63] rather than a direct role for UPF1 in HMD.

To further examine the role of UPF1 in HMD, we used hydroxyurea (HU) to inhibit replication and trigger replication-dependent HMD (Figure 3E).[56,98] N-AID-UPF1 HCT116 cells treated for up to 60 min with 0.5 mM HU exhibited time-dependent reduction of replication-dependent H1-2 and H2AC18 mRNAs (normalized to replication-independent H3-3A; Figure 3G). However, UPF1 depletion, whether for a short (6 h; Figure 3G) or extended period (12–48 h; Figure S3H), had no effect on the HU-induced degradation of both histone mRNAs, despite clear effects on NMD. Compared with NMD, where UPF1 is a key factor and its depletion has a marked impact on NMD substrates, our data suggest that it has little to no involvement in replication-dependent HMD.

Definition of the NMDRHT

Until now, our analyses of UPF1-regulated transcriptomes relied on gene-level aggregated counts (Figure S4A) and the GENCODE annotation.[15] While this approach is computationally robust,[99] it oversimplifies the complexity of the human transcriptome. AS can generate isoforms with distinct NMD sensitivities, which may be overlooked by gene-level analyses. At the transcript level, GENCODE (V42) includes >250,000 annotated transcript isoforms, many of which have low or missing transcript support levels (TSLs), particularly among NMD- and lncRNA-annotated mRNAs (Figures S4B and S4C). This annotation uncertainty, with the inherent read-to-transcript ambiguity (RTA) in short-read RNA-seq quantification,[100] complicates NMD-relevant transcript-level analyses. Furthermore, novel transcript isoforms not annotated in GENCODE will be missed.

To address this, we established a consolidated NMD-regulated human transcriptome (NMDRHT) by integrating long-read- and short-read-based transcriptome assemblies (Figures 4A and S4D; see STAR Methods for full details). We sequenced untreated or 12 h IAA-treated N-AID-UPF1 cells with the DirectRNA (**Oxford Nanopore Technologies**) as well as the Kinnex full-length RNA kit (PacBio) (Figure S4E). GENCODE-guided and *de novo* transcriptome annotations were assembled with three benchmarked tools (Figure S4D).[101–106] In addition, we incorporated short-read RNA-seq transcript annotations from other cell lines, NMD inhibition methods, and library preparations (Figure S4D).

(F) Expression levels of HGNC-annotated histone mRNAs as baseMean from DESeq2 plotted versus expression changes (DGE) of 12 h (left) or 48 h (right) UPF1 depletion, with rRNA depletion library preparation.

(G) (Top) Western blot of UPF1 from N-terminal AID-tagged UPF1 HCT116 cells, treated with 500 μM IAA and 500 μM hydroxyurea (HU) for the indicated time; o.e., overexposure. (Middle) End-point RT-qPCR of SRSF2 (as in Figure 1C). (Bottom) qPCR of replication-dependent histone mRNAs H1-2 and H2AC18, normalized to replication-independent histone mRNA H3-3A as $\log_2$ fold change ($\log_2$FC). Individual data points and mean (bars) are shown (n = 3).

Please cite this article in press as: Boehm et al., Rapid UPF1 depletion illuminates the temporal dynamics of the NMD-regulated human transcriptome, Molecular Cell (2025), https://doi.org/10.1016/j.molcel.2025.08.015

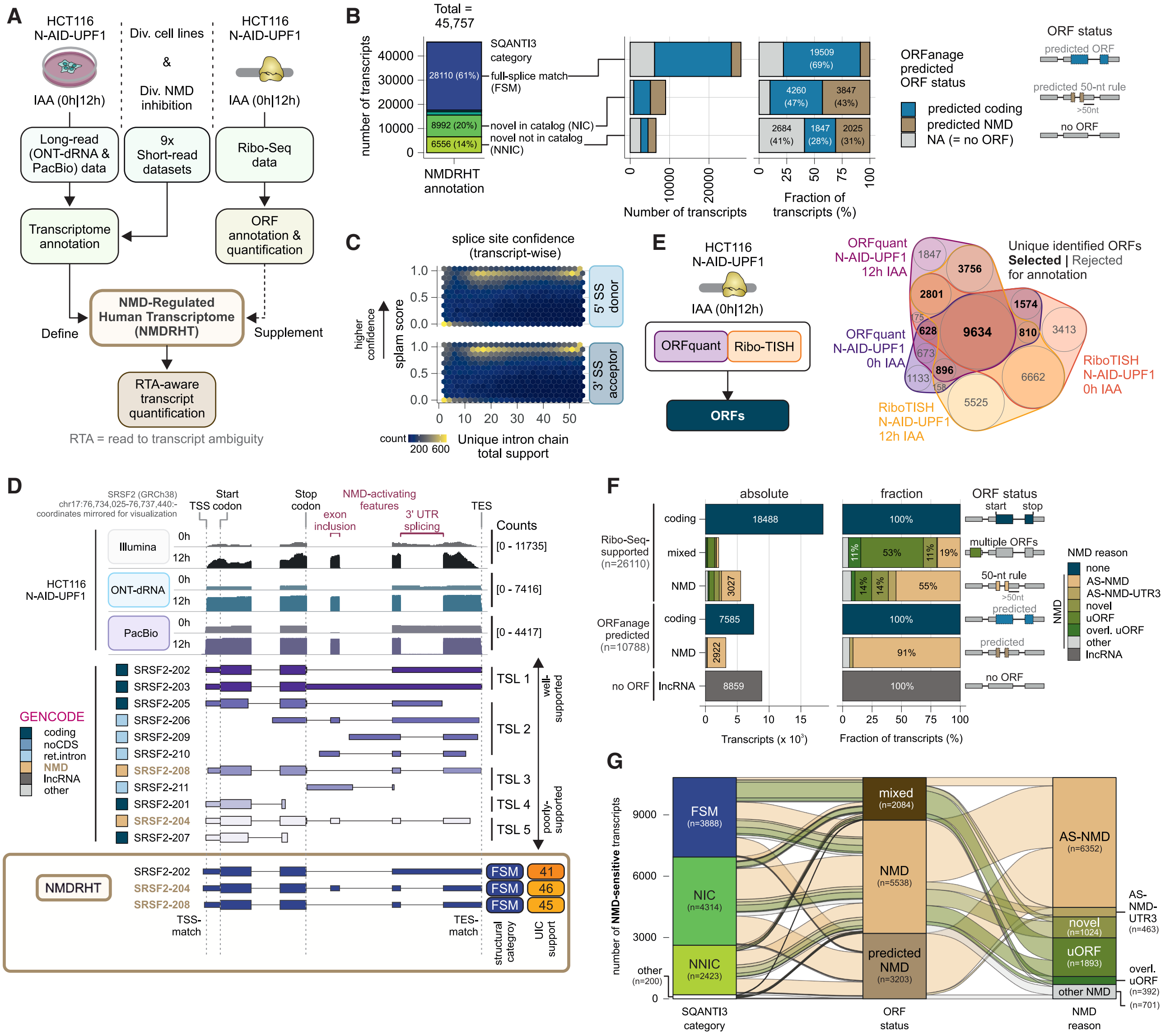

Figure 4. Defining the NMDRHT

(A) Scheme for integrating data sources to generate the NMD-regulated human transcriptome (NMDRHT).

(B) (Left) Number of NMDRHT-annotated transcripts by SQANTI3 categories in relation to the GENCODE reference annotation. Abbreviations are explained in the STAR Methods section. (Right) Absolute number or fraction of NMDRHT-annotated transcripts according to their predicted ORF status.

(C) Aggregated transcript-wise splice site confidence (splam score) per intron chain.

(D) (Top) Integrative Genomics Viewer (IGV) snapshot of SRSF2 RNA-seq (short- and long-read) coverage from untreated or 12 h UPF1-depleted cells. (Middle) GENCODE-annotated transcripts with their transcript biotype and transcript support level (TSL). (Bottom) NMDRHT-annotated SRSF2 transcript isoforms with their SQANTI3 category and unique intron chain (UIC) support. Coordinates of SRSF2 were mirrored for visualization.

(E) (Left) Scheme of ORF identification. (Right) nVenn plot depicting the overlap between ORFquant and Ribo-TISH detected ORFs, and those selected for NMDRHT-supplementation are in bold font.

(F) Absolute number and fraction of transcripts by ORF status and NMD reason, stratified by Ribo-seq-supported or ORFanage-predicted ORFs. Transcripts with no detected/predicted ORFs were labeled as lncRNAs.

(G) Alluvial plot of NMDRHT-annotated NMD-sensitive transcripts with SQANTI3 categories, ORF status, and NMD reason as nodes. Streams are colored according to NMD reason.

Across 54 transcriptomes we assembled in total 2.1 × 10^6 transcripts, with 48% matching the reference annotation and 41% containing novel intron chains (Figure S4F).[107] Comparing all transcriptomes, we identified 405,428 unique intron chains (UICs), of which the vast majority was supported (=detected) in only a few transcriptomes (Figures S4D and S4G). A two-phase gene-wise filtering strategy selected UICs from well-supported genes (high filter level), followed by otherwise missed genes

Please cite this article in press as: Boehm et al., Rapid UPF1 depletion illuminates the temporal dynamics of the NMD-regulated human transcriptome, Molecular Cell (2025), https://doi.org/10.1016/j.molcel.2025.08.015

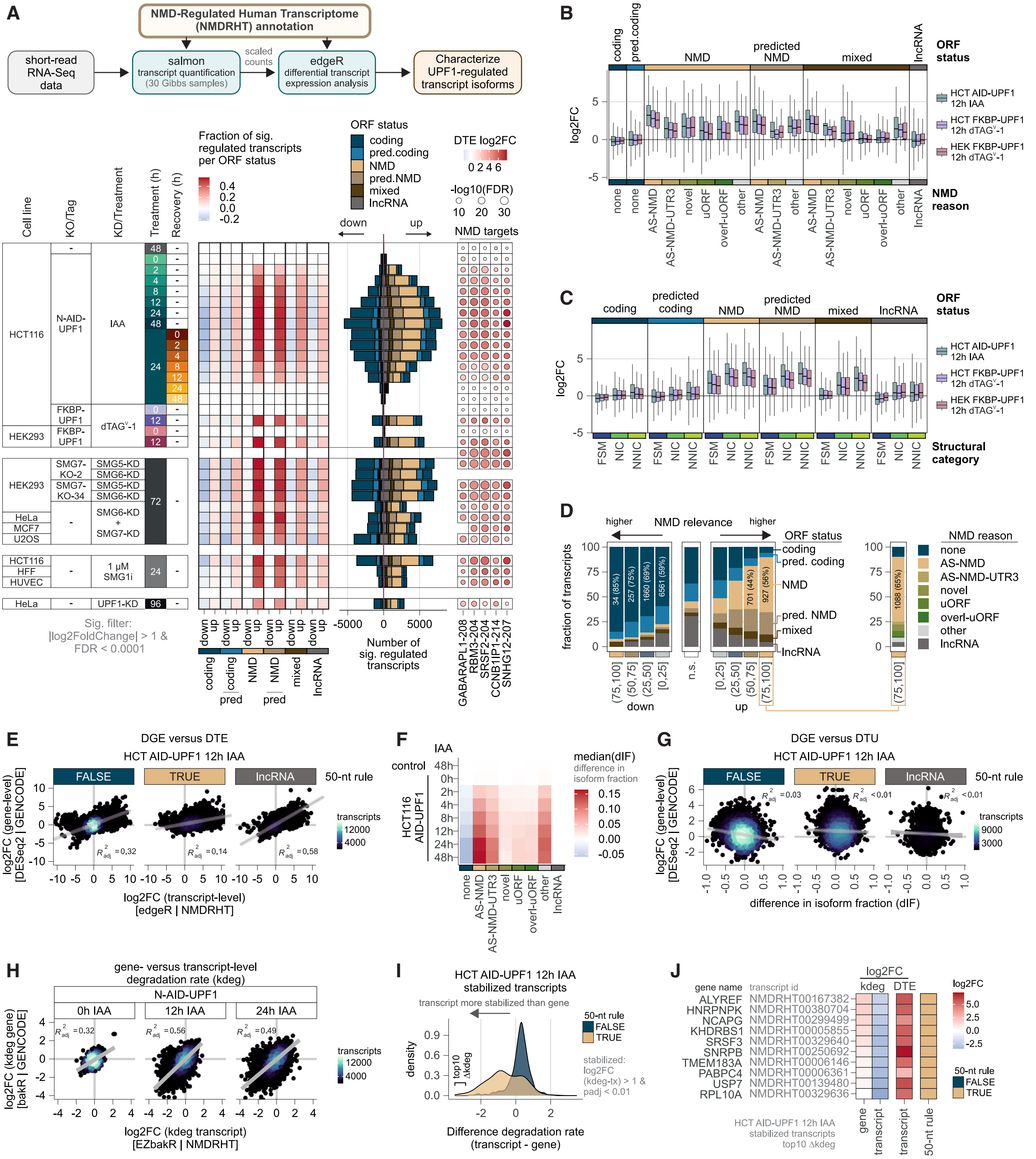

Figure 5. UPF1 regulates primarily alternatively spliced NMD-targeted transcripts

(A) (Top) Scheme for RTA-aware transcript quantification and differential transcript expression (DTE) analysis. (Bottom) Comparison across RNA-seq data regarding the fraction of significantly differentially expressed NMDRHT-annotated transcripts (separated by up-/downregulation) versus all detected transcripts per ORF status (left), the absolute number of significantly regulated transcripts stratified by ORF status (middle), as well as expression changes of individual NMD-target mRNAs (right).

(B) Boxplot of DTE $\log_2$FC from 12 h UPF1-depleted conditions, stratified by ORF status (top) and NMD reason (bottom).

(C) Boxplot of DTE $\log_2$FC from 12 h UPF1-depleted conditions, stratified by ORF status (top) and SQANTI3 categories (bottom).

(legend continued on next page)

with low-supported UICs (low filter level; Figure S4H). Finally, we annotated 45,747 transcripts as the NMDRHT. This dataset contains both normal, non-NMD-targeted isoforms and those likely regulated by NMD. For further characterization, we determined transcript boundaries by majority voting, recovered ORF information (Figure S4I), and predicted NMD sensitivity using the 50-nt rule (Figure 4B). Transcripts with predicted stop codons >50-nt upstream of the last exon-exon junction were classified as NMD-activating, accounting for ≈18% of all NMDRHT transcripts. About one-third of NMDRHT-annotated transcripts contained novel intron chains, which were more frequently predicted to elicit NMD (Figure 4B).

NMDRHT transcriptome boundaries generally matched reference annotations, with greater 5′ end variability in low support and "novel not in catalog" (NNIC) transcripts (Figure S4J). 3′ ends aligned closely with reference positions. Splam-based[108] splicing confidence was high for well-supported transcripts (Figure 4C), comparable to GENCODE TSL 1 (Figure S4K), but lower for NNIC or low-support transcripts.

As an example, we visualized the NMD-targeted gene SRSF2 (Figure 4D). Of 11 GENCODE isoforms, only three (matching SRSF2-202, -204, and -208) remained after filtering in the NMDRHT annotation (Figures 4D and S4L). The protein-coding isoform SRSF2-202 predominates under control conditions, while the NMD-target SRSF2-204 strongly accumulated upon UPF1 depletion (Figure 4D). These findings demonstrate that the NMDRHT annotation captures the most relevant mRNA isoforms for NMD-related studies.

ORF annotation reveals NMD-activating features

The 50-nt rule predicts NMD sensitivity based on the distance between the stop codon and the last exon-exon junction.[109–111] However, the accurate application of this rule requires transcript-specific knowledge of translated ORFs, which is suboptimal in our GENCODE-based ORF recovery approach. To refine ORF annotation and properly account for novel isoforms and/or ORFs, we leveraged our Ribo-seq data and performed ORF annotation with two software packages (Figures 4A, 4E, and S4M).[112,113] Only ORFs identified by both ORFquant and Ribo-TISH in each condition (0 or 12 h IAA) were considered (Figures 4E and S4N).

Next, we determined the transcript-specific ORF status and identified the NMD-activating feature, judged by length-normalized ORF usage (Figures 4F and S4M; see STAR Methods for details). Ribo-seq-supported ORFs were assigned to ∼60% of NMDRHT-annotated transcripts, with 71% classified as NMD-insensitive (= "coding"). By contrast, 5,538 transcripts were classified as NMD-sensitive (= NMD), and 2,084 contained multiple ORFs, with at least one predicted to trigger NMD (= "mixed"; Figure 4G). Interestingly, upstream ORFs (uORFs) primarily contributed to NMD sensitivity in mixed transcripts, whereas AS-NMD was the predominant mechanism in NMD-classified transcripts (Figures 4F and 4G). 3′ UTR splicing events (AS-NMD-UTR3), where the ORF remains unchanged (e.g., SRSF2), were less frequent. Novel ORFs (e.g., ZFAS1) accounted for 10%–15% in mixed and NMD transcripts. For NMDRHT-annotated transcripts lacking Ribo-seq-supported ORFs, we retained the predicted ORF status (= predicted coding/predicted NMD) or assigned "lncRNA" when no ORF information was available (Figure 4F). Collectively, these results define a high-quality, data-driven, and consolidated NMDRHT transcriptome, distinguishing NMD-sensitive and -insensitive human transcript isoforms.

Stabilization of NMD-sensitive transcript isoforms

Next, we evaluated how GENCODE or NMDRHT annotation influences transcript isoform quantification of UPF1-depletion short-read RNA-seq datasets. While read mapping fractions were similar, NMDRHT yielded fewer transcript equivalence classes[114] and lower gene-wise overdispersion, improving quantification accuracy (Figure S5A). For example, NMDRHT improved quantification accuracy of SRSF2 isoforms (Figure S5B). Consequently, the NMDRHT annotation was used for all subsequent transcript isoform analyses.

Global differential transcript expression (DTE) analysis across multiple NMD-compromised RNA-seq datasets revealed strong and specific upregulation of NMD-sensitive transcripts (Figure 5A; Table S3). Both Ribo-seq-supported and predicted NMD-targeted transcripts are upregulated, whereas mixed and lncRNA transcripts showed weaker expression changes. All NMD-activating features resulted in increased transcript isoform levels upon UPF1 depletion for 12 h (Figure 5B), with AS-NMD having the most pronounced effects. Mixed transcripts containing uORFs exhibited a milder response, while novel transcript isoforms (NIC and NNIC) were also markedly upregulated, highlighting NMDRHT's ability to identify previously unannotated UPF1- and NMD-dependent transcript isoforms (Figure 5C).

To further characterize these dynamics, we performed hierarchical clustering, impulse modeling, and NMD relevance analysis on the transcript level, similarly to our earlier gene-level analyses (Figures S5C–S5E). This approach identified thousands of transcripts in early and delayed upregulated clusters (Figures S5C and S5D), many of which exhibited strong NMD relevance

(D) (Left) Fraction of NMDRHT-annotated transcripts per ORF status and NMD relevance bin. (Right) Fraction of upregulated, high NMD relevance NMDRHT transcripts per NMD reason.

(E) Correlation between gene (DGE and DESeq2; GENCODE-based) and transcript (DTE, edgeR; NMDRHT-based) expression changes in 12 h UPF1-depleted cells, stratified by 50-nt rule. The adjusted R^2 from the linear fit is indicated.

(F) Heatmap of median difference in isoform fraction (dIF) of NMDRHT-annotated transcripts, stratified by UPF1 depletion time and NMD reason.

(G) Correlation between gene (DGE, DESeq2; GENCODE-based) expression changes and differential transcript usage (DTU, IsoformSwitchAnalyzeR; NMDRHT-based) in 12 h UPF1-depleted cells, stratified by 50-nt rule. The adjusted R^2 from the linear fit is indicated.

(H) Correlation between gene- and transcript-level degradation rates (kdeg).

(I) Difference between transcript- and gene-level degradation rates of stabilized transcripts in 12 h UPF1-depleted HCT116 cells, stratified by the 50-nt rule.

(J) Gene and transcript degradation rates, transcript expression levels, and NMD-sensitivity characteristics of the top 10 different (kdeg) transcripts (indicated in I).

Please cite this article in press as: Boehm et al., Rapid UPF1 depletion illuminates the temporal dynamics of the NMD-regulated human transcriptome, Molecular Cell (2025), https://doi.org/10.1016/j.molcel.2025.08.015

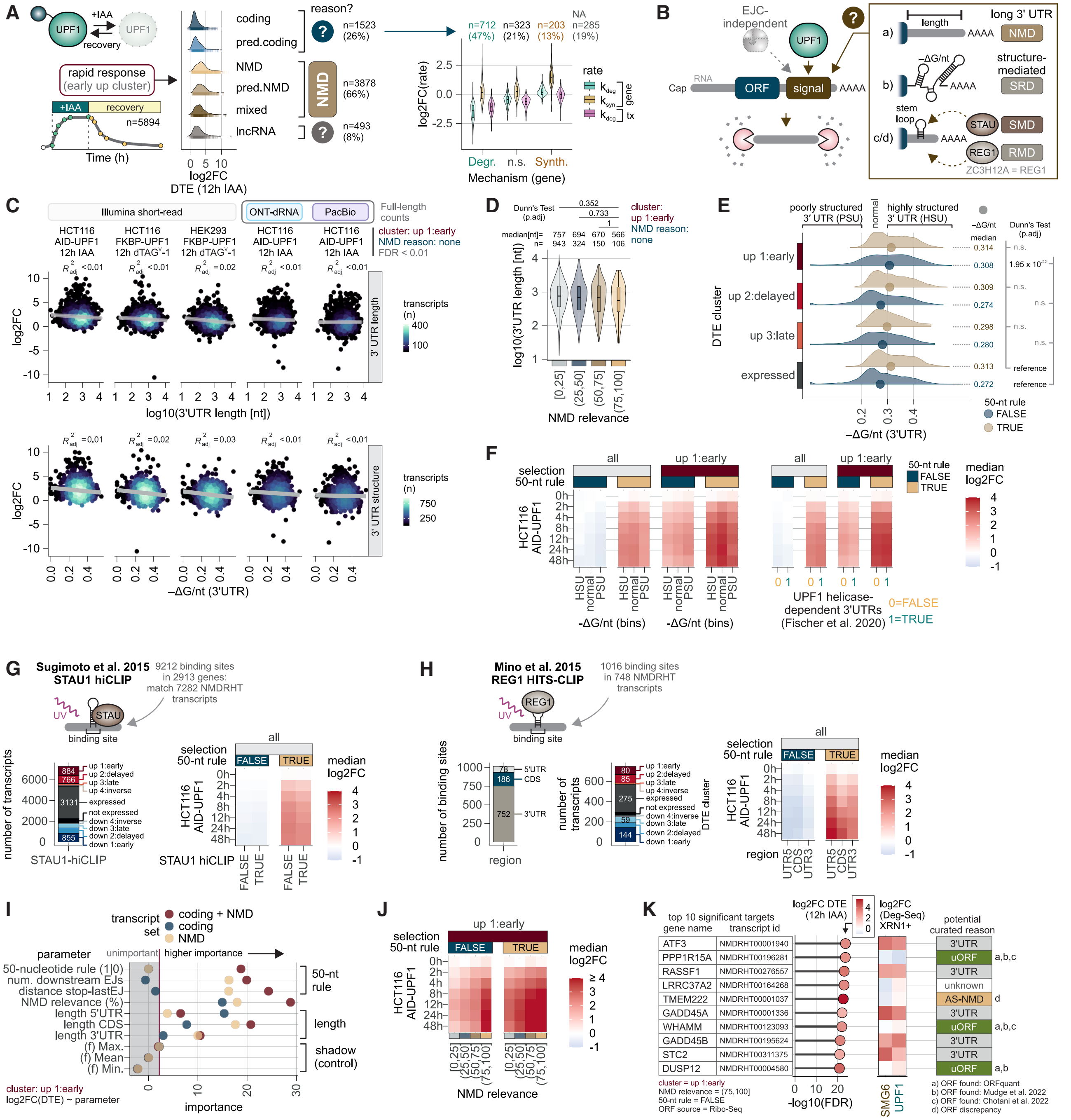

Figure 6. Investigation of non-canonical UPF1-regulated transcripts

(A) (Left) Partitioning of early upregulated cluster transcripts and expression changes per ORF status. (Right) Violin boxplot of $\log_2$FC of differential degradation (kdeg; gene or transcript level) or synthesis (ksyn; gene) rate constants of non-NMD-annotated transcripts (NMD reason = none) per gene-level bakR mechanistic conclusion.

(B) Scheme of EJC-independent degradation of UPF1-regulated mRNAs.

(C) (Top) Correlation between DTE and 3′ UTR length across 12 h UPF1-depleted conditions from short- or long-read sequencing data. (Bottom) Correlation between DTE and length-normalized, minimum thermodynamic free energy ($-\Delta G$/nt) of the 3′ UTR. For long-read data, only full-length counts were used. Early upregulated non-NMD transcripts (FDR < 0.01) are shown. The adjusted R^2 from the linear fit is indicated.

(D) Violin boxplot of 3′ UTR length per NMD relevance bin for early upregulated non-NMD transcripts. Median 3′ UTR length and number of transcripts per bin are indicated. Significance was determined using a two-sided Dunn's test of multiple comparisons with the high NMD relevance bin as reference.

(legend continued on next page)

(Figure S5E). Consistently, most upregulated and highly NMD-relevant transcripts contained NMD-activating features, with AS-NMD as the predominant mechanism (Figure 5D).

NMD activation typically triggers endonucleolytic cleavage of target mRNAs, followed by rapid degradation of decay intermediates (Figure 1A).[26,33,34,73,115] Using HeLa Degradome-seq data,[115] we observed 3′ fragment accumulation upon XRN1 depletion (Figure S5F), with cleavage enriched near stop codons in highly NMD-relevant or faster upregulated clusters (DTE cluster; Figure S5G), supporting the NMDRHT annotation.

When comparing transcript-level expression changes based on NMDRHT with GENCODE gene-level expression changes, we observed only modest correlation, particularly for NMD-sensitive transcripts (50-nt rule; Figure 5E). This suggests that the increased abundance of PTC-containing mRNAs does not necessarily translate to proportional gene-level expression changes, potentially due to global mRNA buffering[116] or isoform switching. Differential transcript usage (DTU) analysis revealed increased isoform fractions for many NMD-annotated transcripts (Figure S5H), particularly AS-NMD transcripts (Figure 5F). Although DTE and DTU were moderately correlated (Figure S5I), we found no clear global dependency of gene expression changes based on switching isoforms (Figure 5G).

When analyzing kinetic parameters, we observed good correlation between gene- and transcript-level differential degradation rates in UPF1-depleted SLAM-seq data (Figure 5H). However, some stabilized NMD-sensitive transcripts exhibited striking differences between gene- and transcript-level analyses (Figure 5I). Although only 24% of NMD-annotated transcripts could be characterized (Figure S5J), selected mRNAs were determined as stabilized, whereas the gene was not (Figure 5J). Together, these findings emphasize the importance of analyzing NMD at the transcript level, as many events remain undetectable on the gene level.

A subset of UPF1-sensitive transcripts is regulated by non-canonical or undetected features

While two-thirds of rapidly upregulated UPF1-dependent transcripts followed the −50-nt rule (Figures 6A and S5C), a subset of transcript isoforms lacking NMD-activating features still exhibited rapid upregulation upon UPF1 loss (upregulated early cluster; Figures 6A and S5C). SLAM-seq kinetics revealed prominent stabilization of coding transcripts (decreased k_{deg}; Figure 6A), while less data were available for lncRNAs (Figure S6A). Functional enrichment analysis did not identify any degradation- or synthesis-associated Gene Ontology biological processes (Figure S6B) among these transcripts. Given the high proportion of stabilized transcripts, we hypothesized that UPF1 degrades these mRNAs independently of EJC-induced NMD.

We explored alternative UPF1-dependent decay mechanisms, including long 3′ UTR NMD,[29,30] structure-mediated RNA decay (SRD),[55] and STAU- or regnase-1-mediated mRNA decay (SMD/RMD)[54,117] (Figure 6B).

Early upregulated transcripts lacking 50-nt-rule features had significantly shorter, not longer, 3′ UTR, independent of kinetic mechanisms (Figure S6C). Moreover, no correlation was observed between 3′ UTR length and transcript upregulation after 12 h UPF1 depletion across degron systems and cell lines (Figure 6C). This trend was consistent when analyzing full-length transcript counts using Bambu[103] (Figures S6D and S6E). Furthermore, highly NMD-relevant transcripts exhibited shorter 3′ UTRs (Figure 6D), consistent with a recent study,[27] suggesting 3′ UTR length does not explain EJC-independent transcript upregulation.

Next, we assessed whether 3′ UTR structure influences UPF1-dependent transcript expression using a metric from the SRD study.[55] Interestingly, early upregulated non-NMD transcripts displayed significantly more structured 3′ UTRs, resembling NMD-annotated isoforms (Figure 6E). However, no direct correlation was found between transcript upregulation and 3′ UTR structure (Figure 6C), nor did expression levels differ between highly and poorly structured 3′ UTRs, including those in the early upregulated transcripts (Figures 6E and 6F).

Fischer and colleagues identified UPF1 helicase-dependent binding in structured 3′ UTRs using CLIP-seq data involving an ATPase-deficient helicase mutant.[55,61] We hypothesized that transcripts containing these regions would be particularly UPF1-sensitive. In NMDRHT, 3,571 transcripts contained UPF1 helicase-dependent 3′ UTRs and exhibited increased secondary structure (Figure S6F) but did not show significant temporal expression changes upon UPF1 depletion (Figure 6F).

We also examined the involvement of STAU1 (via SMD) and regnase-1 (REG1; via RMD) (Figure 6B) using STAU1 hiCLIP,[118] REG1 RIP-seq, and REG1 HITS-CLIP data.[117] After controlling for NMD-activating features, we found no enrichment of upregulated transcripts in STAU1- or REG1-bound mRNAs, indicating the observed regulation is NMD-dependent (Figures 6G, 6H, and S6G).

(E) Ridgeplot of the predicted 3′ UTR structure of the indicated DTE cluster transcripts, stratified by the 50-nt rule. Significance was determined using a two-sided Dunn's test of multiple comparisons.

(F) (Left) Heatmap of median DTE of NMDRHT-annotated transcripts, stratified by UPF1 depletion time, predicted structure bins (from E), all versus early upregulated DTE cluster and 50-nt rule. (Right) Same as in the left panel but stratified by UPF1 helicase-dependent 3′ UTRs.

(G) (Top) Scheme of STAU1 binding site determination. (Left) Number of NMDRHT transcripts matching published STAU1 binding sites per DTE cluster. (Right) Heatmap of median DTE of NMDRHT-annotated transcripts, stratified by UPF1 depletion time, predicted STAU1 binding sites, and 50-nt rule.

(H) (Top) Scheme of REG1 binding site determination. (Left) Number of REG1-binding sites per NMDRHT-transcript region. (Middle) Number of NMDRHT transcripts matching published REG1 binding sites per DTE cluster. (Right) Heatmap of median DTE of NMDRHT-annotated transcripts, stratified by UPF1 depletion time, predicted REG1 binding region, and 50-nt rule.

(I) Importance of transcript features for DTE from early upregulated transcripts per transcript set.

(J) Heatmap of median DTE of early upregulated NMDRHT-annotated transcripts, stratified by UPF1 depletion time, NMD relevance bin, and 50-nt rule.

(K) (Left) Selection of the top 10 most significant early upregulated transcripts (by FDR; 12 h IAA) with high NMD relevance, lacking the 50-nt NMD feature and Ribo-seq supported ORFs. (Middle) Differential Degradome-seq counts in a 200-nt window around the stop codon, for XRN1 versus XRN1 + SMG6 or XRN1 + UPF1 KD. (Right) Potential curated reason.

Please cite this article in press as: Boehm et al., Rapid UPF1 depletion illuminates the temporal dynamics of the NMD-regulated human transcriptome, Molecular Cell (2025), https://doi.org/10.1016/j.molcel.2025.08.015

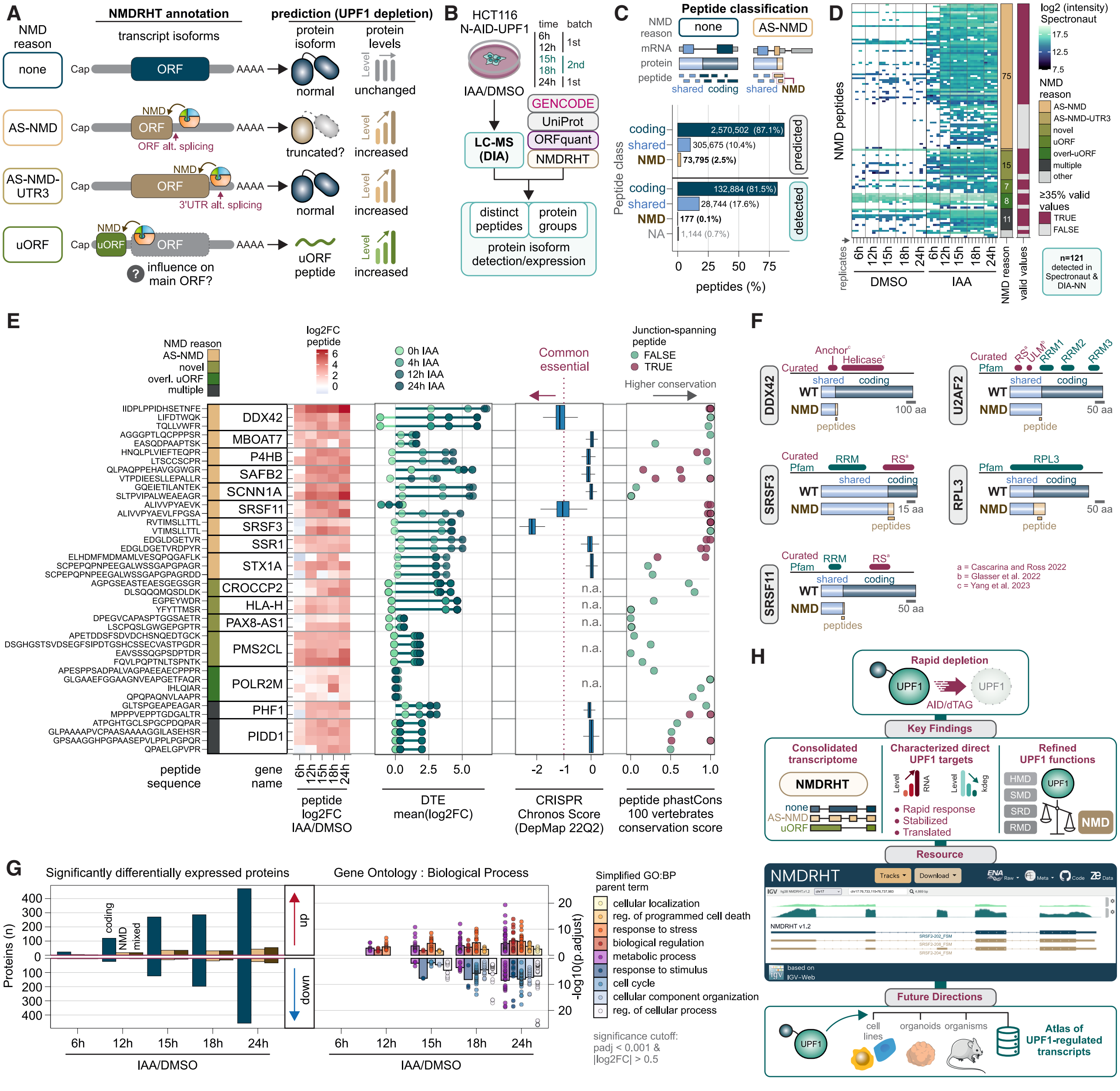

Figure 7. Detection of peptides encoded by NMD-sensitive transcripts

(A) Scheme of predicted protein isoforms and protein expression levels depending on the NMDRHT-based NMD reason.

(B) Overview of peptide and protein group detection using multiple data sources and data-independent acquisition (DIA) liquid chromatography-mass spectrometry (LC-MS).

(C) (Top) Representation of tryptic peptides generated from protein isoforms and their classification. C-terminal peptides from AS-NMD-encoded proteins may be used as distinct identifiers. (Bottom) Fractions and numbers of predicted and detected peptides per peptide class.

(D) Intensity of NMD-informative peptides detected by Spectronaut per replicate, treatment, and time course. Classification of peptides according to NMD reason, and peptides with >35% valid values across conditions are indicated.

(E) (Left) Differential expression of high-quality NMD-informative peptides (detected by both Spectronaut and DIA-NN, >1 peptide per gene). (Middle left) Mean DTE of transcripts encoding for the respective proteins/peptides. (Middle right) Gene essentiality based on DepMap 22Q2 Chronos score. (Right) Aggregated phastCons 100 vertebrate conservation score of sequence encoding for the respective peptide, stratified by whether the peptide is splice junction-spanning.

(F) Representation of selected essential proteins whose NMD-informative peptide is highly conserved between vertebrates. Positions of the NMD-informative peptide and protein domains/regions from the protein families (Pfam) database or external sources are indicated.

(legend continued on next page)

Please cite this article in press as: Boehm et al., Rapid UPF1 depletion illuminates the temporal dynamics of the NMD-regulated human transcriptome, Molecular Cell (2025), https://doi.org/10.1016/j.molcel.2025.08.015

Furthermore, several transcripts previously linked to long 3′ UTR-mediated NMD,[119] SMD,[120–123] RMD,[117,124] or SRD[55] remained largely unaffected by UPF1 depletion or were upregulated due to EJC-dependent NMD (50-nt rule; Figure S6H). For instance, ARF1, a well-established STAU1-bound target,[118,120,125] was downregulated upon UPF1 loss, consistent with previous studies questioning functional SMD relevance.[122,126] Collectively, no EJC-independent pathway explained the expression changes of seemingly UPF1-regulated protein-coding transcripts.

To explore other potential explanations, we performed random forest classification-based feature selection,[127] incorporating NMDRHT-transcript properties, published RNA metabolic labeling, and UPF1-centric data sources (Figure S6I).[92,93,126] As expected, the 50-nt rule and its sub-features were top predictors for coding and NMD-annotated transcripts (Figures 6I and S6I), reinforcing the dominant role of EJC-dependent NMD.

Surprisingly, NMD relevance was also highly ranked for transcripts not fulfilling the 50-nt rule (Figures 6I, S6I, and S6J). Accordingly, early transcripts without NMDRHT-annotated NMD features were more strongly upregulated and stabilized when their NMD relevance was higher (Figures 6J, S6K, and S6L), suggesting UPF1 targets them for degradation via non-canonical or undetected features such as uORFs or 3′ UTR elements.

To investigate this, we manually inspected the 10 most significantly upregulated early transcripts with high NMD relevance, Ribo-seq-supported ORFs, but no apparent NMD feature (Figure 6K). Three transcripts contain uORFs detected by ORFquant (rejected in Ribo-TISH due to small size; Figure S4N), a standardized Ribo-seq ORFs catalog,[128] and/or a comprehensive map of human small ORFs[129] (Figure 6K). The TMEM222 isoform was likely misclassified due to discrepancies in ORF annotation. No clear degradation feature was identified for LRRC37A2, but five of the remaining transcripts appeared to undergo NMD via their 3′ UTR. These transcripts were stabilized, exhibited strong SMG6- and UPF1-dependent Degradome-seq coverage near the normal stop codon (Figures 6K and S5E), and had been previously identified as NMD targets.[73,80,115,130–132] In summary, no single NMD-independent mechanism explained the upregulation of these transcripts. Instead, previously undetected features, like uORFs or 3′ UTR elements, appear to drive their UPF1-dependent regulation.

Cellular proteome changes upon UPF1 depletion

Given the extensive transcriptomic alterations following UPF1 loss, we investigated how NMD inhibition impacts the cellular proteome. We hypothesized that distinct NMD-activating features would result in the accumulation of specific protein isoforms or peptides after UPF1 depletion (Figure 7A). For example, AS-NMD transcripts were expected to encode truncated proteins due to shortened ORFs (Figure S7A), with disrupted functional protein domains or altered intrinsic disordered regions (Figure S7B).

To identify protein isoforms from NMD-annotated transcripts, we re-analyzed our proteomics time course and additional 15- and 18-h UPF1 depletion samples at the peptide level using Spectronaut (Figures 7B and S7C). Detection of NMD-specific protein isoforms by mass spectrometry is inherently challenging, as less than 3% of all theoretically detectable tryptic peptides are NMD-specific (Figure 7C). AS-NMD-encoded proteins, for instance, typically contain unique sequence identifiers only within C-terminal peptides.

Unexpectedly, Spectronaut detected only 177 NMD-informative peptides, less than 0.1% of all identified peptides (Figure 7C). This discrepancy between detected and predicted peptides could not be explained by known technical limitations such as poor detection of C-terminal peptides,[133,134] difficulty in identifying junction-spanning peptides,[135] or generally low predicted peptide detectability[136] (Figures S7D and S7E). Reanalyzing the data with alternative software (data-independent acquisition [DIA]-NN)[137] yielded similar results, showing strong agreement with Spectronaut and high sample-wise correlation (Figures S7F and S7G). Notably, 121 NMD-classified peptides were found by both methods and thus considered as reliably detected. Most detected NMD peptides were associated with alternatively spliced transcripts (AS-NMD; 75 out of 121 peptides) and were barely detectable in control conditions but accumulated upon UPF1 depletion (Figure 7D). 87 peptides with sufficient valid values across all conditions ($\geq$35%) were selected for further in-depth analysis.

Among these, we identified highly conserved, NMD-isoform-encoded peptides from essential genes (Figures 7E and S7H). These include single peptides from AS-NMD targets RPL3 (large ribosomal subunit) and U2AF2 (splicing factor) (Figure S7H) and multiple peptides from DDX42 (helicase; U2 small nuclear ribonucleoprotein particle [snRNP] assembly), SRSF3, and SRSF11 (both splicing regulators) (Figure 7E). The NMD-activating AS events disrupted key functional domains, e.g., arginine/serine-rich (RS) domains in SRSF3 and SRSF11,[138] the helicase domain in DDX42,[139] or RNA recognition motif (RRM) domains in U2AF2[140] (Figure 7F). The 87 NMD peptides were enriched for proteins involved in RNA processing and splicing (Figure S7I). Prolonged UPF1 depletion resulted in thousands of significantly (false discovery rate [FDR] < 0.0001) differentially spliced intron clusters containing at least one GENCODE-unannotated junction (Figure S7J), suggesting that the accumulation of truncated, dysfunctional proteins may exacerbate splicing errors and disrupt gene expression homeostasis.

Surprisingly, we detected two peptides for the GENCODE-annotated lncRNA CROCCP2 (Figure 7E), a human-specific gene expressed in the fetal cortex[141] that promotes cortical progenitor expansion.[142] Beyond CROCCP2, several human-specific and

(G) (Left) Number of significantly differentially expressed proteins (protein group analysis), stratified by up-/downregulation, NMD reason, and UPF1 depletion time course. (Right) Simplified Gene Ontology: biological process analysis showing the significantly enriched parent terms per up-/downregulated proteins per time point.

(H) Overview of key findings of this study, the availability of the data as an easily explorable resource, and future directions to comprehensively identify UPF1-regulated transcripts.

Please cite this article in press as: Boehm et al., Rapid UPF1 depletion illuminates the temporal dynamics of the NMD-regulated human transcriptome, Molecular Cell (2025), https://doi.org/10.1016/j.molcel.2025.08.015

duplicated gene family members were upregulated in UPF1-depleted cells, including the neuroblastoma breakpoint family (NBPF) (Figure S7K). NBPF genes encode proteins with up to hundreds of Olduvai domains (formerly DUF1220), the largest human-specific coding region expansion in the genome.[143] The copy number of Olduvai protein domains has been linked to primate brain size,[144] as well as autistic spectrum disorders.[145] NBPF genes are expressed during human corticogenesis[141] and may contribute to neural stem cell proliferation.[146] Our data suggest these recently evolved and brain-associated genes are constitutively transcribed in non-neuronal cells but normally degraded by UPF1 via NMD.

At the grouped protein level, UPF1-depletion primarily affected the expression of protein encoded by non-NMD-annotated mRNAs (Figure 7G). Gene Ontology analysis revealed dysregulation of metabolic processes, upregulation of stress response and apoptosis factors, and downregulated cell cycle components (Figure 7G). Together, these findings highlight the critical role of UPF1 in maintaining cellular homeostasis and highlight the experimental challenges associated with prolonged UPF1 inactivation.

DISCUSSION

UPF1 is the most extensively studied NMD factor, with over 650 publications since its discovery in 1991.[147] While it is non-essential in yeast and *C. elegans*, its role in higher eukaryotes has primarily been investigated using dominant-negative mutants or siRNA KDs,[131,148] methods lacking temporal resolution. In this study, we applied time-resolved UPF1 depletion using degrons in two cell lines, enabling high-resolution analysis of UPF1-dependent gene expression. Beyond providing distinct biological insights, our datasets serve as a valuable resource.

Unlike conventional KDs, our approach enables the direct observation of UPF1 depletion effects while minimizing secondary influences. Molecular changes are captured as they occur, providing a refined view of UPF1's role in gene regulation. However, while this approach effectively distinguishes NMD substrates from indirectly affected transcripts, the biological basis of the different response classes of UPF1-regulated mRNAs remains to be fully understood.

Prolonged UPF1 depletion led to a progressive increase in transcriptome alterations, including changes in gene and transcript expression as well as the activation of cryptic splice sites. These late-occurring changes are largely driven by secondary effects rather than direct NMD regulation. As a result, classical KOs and prolonged siRNA KDs of UPF1 likely introduce widespread nonspecific gene expression changes, making them less suitable for studies requiring a clear distinction between direct NMD effects and broader regulatory consequences.

A key advantage of the degron system is its reversibility.[77] Upon auxin removal, upregulated NMD substrates undergo rapid degradation. Whether the same mRNAs are initially stabilized and later retargeted remains uncertain. However, this possibility is supported by previous studies suggesting that NMD can occur during each round of translation, even for mRNAs that temporarily evade degradation.[149–151] This feature opens avenues for new experimental designs leveraging advanced high-throughput technologies to study cellular and organismal recovery following acute transcriptome perturbations.

To enable precise NMD analyses, we have established a rigorously curated transcriptome optimized for studying NMD-regulated isoforms. Unlike conventional reference annotations such as GENCODE, which include numerous unverifiable transcripts, our dataset focuses on experimentally confirmed and functionally relevant NMD-activating features. This refined resource eliminates confounding noise, facilitating more accurate assessments of NMD's impact on gene expression. We provide an interactively explorable web application based on igv.js[152] at https://nmdrht.uni-koeln.de (Figure 7H).

Our results demonstrate that NMD substrates constitute the most abundant and robust class of UPF1-regulated transcripts, overlapping with substrates of other NMD factors (Figure 7H). Although we found no clear evidence for additional UPF1-dependent mechanisms, such pathways may exist below our current detection threshold. Some UPF1-dependent transcripts may harbor previously unrecognized sequence elements and/or structural features conferring NMD sensitivity, highlighting the need for further investigation. Future studies integrating additional high-resolution datasets will improve NMD-target identification and advance our understanding of the fundamental principles governing mRNA surveillance (Figure 7H). Since early UPF1 KD studies,[131] technological innovations have revolutionized the field, with degron-based approaches setting a new standard for precision in NMD research. When combined with cutting-edge transcriptomic techniques such as SLAM-seq and Ribo-seq, these tools now allow unprecedented precision in dissecting NMD across diverse biological systems.

Limitations of the study

Our study primarily used HCT116 and HEK293 cells, well-established NMD models, along with HUVEC and HFF cells. While these models offer valuable insights, UPF1- and NMD-dependent regulation may differ across cell types, tissues, or developmental stages. Future studies in broader biological contexts could extend the relevance of our findings, especially regarding cell-type-specific splicing and expression.

The use of engineered degron cell lines enabled precise temporal control of UPF1 depletion. While individual cell lines exhibited some transcriptional clonal variation, inherent to the degron-tagging procedure and selection process, we employed different degron tags in two cell lines and used independent measures like SLAM-seq-based RNA turnover to ensure reproducibility and reliability of our observations.

Our temporal profiling approach offers a framework for distinguishing direct NMD-target transcripts from transcriptional changes, although the boundary between immediate and secondary effects remains inherently ambiguous. The 8–12 h window identified in our dataset appears well-suited for capturing early, primary responses, providing a strong foundation for future time-resolved studies.

Overall, while there are areas for continued refinement and broader validation, our approach establishes a robust platform for studying NMD and sets the stage for deeper exploration of its regulatory complexity across biological systems.

RESOURCE AVAILABILITY

Lead contact

Further information and requests for reagents should be directed to and will be fulfilled by the lead contact, Niels H. Gehring (ngehring@uni-koeln.de).

Materials availability

All cell lines and plasmids generated in this study are listed in Table S1 and are available upon request to the lead contact.

Data and code availability

- This study analyzes publicly available data, which are listed in Table S1. RNA-seq data generated in this study have been deposited at BioStudies/ArrayExpress and are publicly available as of the date of publication. Accession numbers (ArrayExpress: E-MTAB-13839, E-MTAB-13788, E-MTAB-13789, E-MTAB-13787, E-MTAB-13829, E-MTAB-13836, E-MTAB-14755, E-MTAB-14725, and E-MTAB-13837) are described in detail in Table S1. The mass spectrometry proteomics data have been deposited to the ProteomeXchange Consortium via the PRIDE[153] partner repository with the dataset identifier PRIDE: PXD061797. All original western blot and quantitative reverse-transcription PCR (RT-qPCR) images have been deposited at Mendeley Data: https://doi.org/10.17632/t9vzn5vwsz.1.
- Original code has been deposited at GitHub: https://github.com/boehmv/2025_UPF1_NMDRHT and Zenodo: https://doi.org/10.5281/zenodo.15047819. All are publicly available as of the date of publication.
- Any additional information required to reanalyze the data reported in this study is available from the lead contact upon request.

ACKNOWLEDGMENTS

We thank Juliane Hancke and Silke Modersohn for technical assistance as well as members of the Gehring and Landthaler labs for discussions and reading of the manuscript. We thank the MDC/BIH Genomics Technology Platform for sequencing. This work was supported by grants from the Deutsche Forschungsgemeinschaft (LA 2941/6-1 to M.L.; GE 2014/4-1, GE 2014/6-2, GE 2014/13-1, and INST 216/1321-1 [CRC1678 project A08] to N.H.G.); and the Center for Molecular Medicine Cologne (CMMC) (C 05 to N.H.G.).

AUTHOR CONTRIBUTIONS

Conceptualization, M.L., N.H.G., and V.B.; methodology, D.W., N.B., M.L., and N.H.G.; software, V.B. and O.P.; formal analysis, V.B.; investigation, D.W. (low-throughput assays and sample preparation for RNA-seq), P.O.W. (initial test-RNA-seq, SLAM-seq, and proteomics sample preparation), L.G.T.A. (ribosome profiling), M.R. (ribosome profiling), M.F. (RNA sequencing), O.P. (proteomics), L.R. (proteomics sample preparation), S.D.G. (SLAM-seq), K.P. (low-throughput assays), and N.B. (AID-tagged cells); resources and data curation, V.B., K.B., O.P., P.M., and E.W.; writing – original draft, review and editing, V.B., N.H.G., and M.L.; visualization, V.B.; supervision and funding acquisition, N.H.G. and M.L.

DECLARATION OF INTERESTS

The authors declare no competing interests.

STAR★METHODS

Detailed methods are provided in the online version of this paper and include the following:

- KEY RESOURCES TABLE
- EXPERIMENTAL MODEL AND STUDY PARTICIPANT DETAILS
  - Cell culture
- METHOD DETAILS
  - Protein structure modeling
  - Essentiality and loss-of-function data
  - siRNA-mediated knockdowns
  - Immunoblot analysis and antibodies
  - RNA extraction for low-throughput assays
  - (Semi-)quantitative RT-PCR
  - Whole proteome analysis
  - Peptide analyses
  - Protein abundance and half-life data
  - Generation of AtAFB2-expressing HCT116 cells
  - Endogenous tagging vectors
  - Generation of homozygously tagged cell lines
  - Knock-in cells using CRIS-PITCh v2
  - Public high-throughput-sequencing data
  - Generated high-throughput-sequencing data
  - Computational analyses of RNA-Seq data
  - Analysis of SLAM-seq data
  - Ribosome profiling
  - Gene ontology
  - Time course analysis
  - Histone mRNA analyses
  - NMDRHT - transcriptome assembly
  - RNA properties and structure prediction
  - Additional data sources
  - Feature selection
  - Data Presentation
- QUANTIFICATION AND STATISTICAL ANALYSIS
- ADDITIONAL RESOURCES

SUPPLEMENTAL INFORMATION

Supplemental information can be found online at https://doi.org/10.1016/j.molcel.2025.08.015.

Received: June 6, 2025
Revised: August 6, 2025
Accepted: August 15, 2025

REFERENCES

1. Doma, M.K., and Parker, R. (2007). RNA quality control in eukaryotes. Cell *131*, 660–668. https://doi.org/10.1016/j.cell.2007.10.041.
2. Monaghan, L., Longman, D., and Cáceres, J.F. (2023). Translation-coupled mRNA quality control mechanisms. EMBO J. *42*, e114378. https://doi.org/10.15252/embj.2023114378.
3. Chang, Y.F., Imam, J.S., and Wilkinson, M.F. (2007). The nonsense-mediated decay RNA surveillance pathway. Annu. Rev. Biochem. *76*, 51–74. https://doi.org/10.1146/annurev.biochem.76.050106.093909.
4. Mort, M., Ivanov, D., Cooper, D.N., and Chuzhanova, N.A. (2008). A meta-analysis of nonsense mutations causing human genetic disease. Hum. Mutat. *29*, 1037–1047. https://doi.org/10.1002/humu.20763.
5. Miller, J.N., and Pearce, D.A. (2014). Nonsense-mediated decay in genetic disease: friend or foe? Mutat. Res. Rev. Mutat. Res. *762*, 52–64. https://doi.org/10.1016/j.mrrev.2014.05.001.
6. Holbrook, J.A., Neu-Yilik, G., Hentze, M.W., and Kulozik, A.E. (2004). Nonsense-mediated decay approaches the clinic. Nat. Genet. *36*, 801–808. https://doi.org/10.1038/ng1403.
7. Campbell, A.E., Dyle, M.C., Albanese, R., Matheny, T., Sudheendran, K., Cortázar, M.A., Forman, T., Fu, R., Gillen, A.E., Caruthers, M.H., et al. (2023). Compromised nonsense-mediated RNA decay results in

truncated RNA-binding protein production upon DUX4 expression. Cell Rep. *42*, 112642. https://doi.org/10.1016/j.celrep.2023.112642.

8. Le Hir, H., Saulière, J., and Wang, Z. (2016). The exon junction complex as a node of post-transcriptional networks. Nat. Rev. Mol. Cell Biol. *17*, 41–54. https://doi.org/10.1038/nrm.2015.7.
9. Woodward, L.A., Mabin, J.W., Gangras, P., and Singh, G. (2017). The exon junction complex: a lifelong guardian of mRNA fate. Wiley Interdiscip. Rev. RNA *8*, e1411. https://doi.org/10.1002/wrna.1411.
10. Boehm, V., Britto-Borges, T., Steckelberg, A.L., Singh, K.K., Gerbracht, J.V., Gueney, E., Blazquez, L., Altmüller, J., Dieterich, C., and Gehring, N.H. (2018). Exon Junction Complexes Suppress Spurious Splice Sites to Safeguard Transcriptome Integrity. Mol. Cell *72*, 482–495.e7. https://doi.org/10.1016/j.molcel.2018.08.030.
11. Kim, V.N., Kataoka, N., and Dreyfuss, G. (2001). Role of the nonsense-mediated decay factor hUpf3 in the splicing-dependent exon-exon junction complex. Science *293*, 1832–1836. https://doi.org/10.1126/science.1062829.
12. Lykke-Andersen, J., Shu, M.D., and Steitz, J.A. (2001). Communication of the position of exon-exon junctions to the mRNA surveillance machinery by the protein RNPS1. Science *293*, 1836–1839. https://doi.org/10.1126/science.1062786.
13. Gehring, N.H., Neu-Yilik, G., Schell, T., Hentze, M.W., and Kulozik, A.E. (2003). Y14 and hUpf3b form an NMD-activating complex. Mol. Cell *11*, 939–949. https://doi.org/10.1016/s1097-2765(03)00142-4.
14. Nagy, E., and Maquat, L.E. (1998). A rule for termination-codon position within intron-containing genes: when nonsense affects RNA abundance. Trends Biochem. Sci. *23*, 198–199. https://doi.org/10.1016/s0968-0004(98)01208-0.
15. Frankish, A., Carbonell-Sala, S., Diekhans, M., Jungreis, I., Loveland, J. E., Mudge, J.M., Sisu, C., Wright, J.C., Arnan, C., Barnes, I., et al. (2023). GENCODE: reference annotation for the human and mouse genomes in 2023. Nucleic Acids Res. *51*, D942–D949. https://doi.org/10.1093/nar/gkac1071.
16. Martin, F.J., Amode, M.R., Aneja, A., Austine-Orimoloye, O., Azov, A.G., Barnes, I., Becker, A., Bennett, R., Berry, A., Bhai, J., et al. (2023). Ensembl 2023. Nucleic Acids Res. *51*, D933–D941. https://doi.org/10.1093/nar/gkac958.
17. Nilsen, T.W., and Graveley, B.R. (2010). Expansion of the eukaryotic proteome by alternative splicing. Nature *463*, 457–463. https://doi.org/10.1038/nature08909.
18. Marasco, L.E., and Kornblihtt, A.R. (2023). The physiology of alternative splicing. Nat. Rev. Mol. Cell Biol. *24*, 242–254. https://doi.org/10.1038/s41580-022-00545-z.
19. Lareau, L.F., and Brenner, S.E. (2015). Regulation of splicing factors by alternative splicing and NMD is conserved between kingdoms yet evolutionarily flexible. Mol. Biol. Evol. *32*, 1072–1079. https://doi.org/10.1093/molbev/msv002.
20. Lareau, L.F., Inada, M., Green, R.E., Wengrod, J.C., and Brenner, S.E. (2007). Unproductive splicing of SR genes associated with highly conserved and ultraconserved DNA elements. Nature *446*, 926–929. https://doi.org/10.1038/nature05676.
21. Ni, J.Z., Grate, L., Donohue, J.P., Preston, C., Nobida, N., O'Brien, G., Shiue, L., Clark, T.A., Blume, J.E., and Ares, M., Jr. (2007). Ultraconserved elements are associated with homeostatic control of splicing regulators by alternative splicing and nonsense-mediated decay. Genes Dev. *21*, 708–718. https://doi.org/10.1101/gad.1525507.
22. García-Moreno, J.F., and Romão, L. (2020). Perspective in Alternative Splicing Coupled to Nonsense-Mediated mRNA Decay. Int. J. Mol. Sci. *21*, 9424. https://doi.org/10.3390/ijms21249424.
23. Lewis, B.P., Green, R.E., and Brenner, S.E. (2003). Evidence for the widespread coupling of alternative splicing and nonsense-mediated mRNA decay in humans. Proc. Natl. Acad. Sci. USA *100*, 189–192. https://doi.org/10.1073/pnas.0136770100.
24. Fair, B., Buen Abad Najar, C.F., Zhao, J., Lozano, S., Reilly, A., Mossian, G., Staley, J.P., Wang, J., and Li, Y.I. (2024). Global impact of unproductive splicing on human gene expression. Nat. Genet. *56*, 1851–1861. https://doi.org/10.1038/s41588-024-01872-x.
25. Leclair, N.K., Brugiolo, M., Urbanski, L., Lawson, S.C., Thakar, K., Yurieva, M., George, J., Hinson, J.T., Cheng, A., Graveley, B.R., et al. (2020). Poison Exon Splicing Regulates a Coordinated Network of SR Protein Expression during Differentiation and Tumorigenesis. Mol. Cell *80*, 648–665.e9. https://doi.org/10.1016/j.molcel.2020.10.019.
26. Boehm, V., Kueckelmann, S., Gerbracht, J.V., Kallabis, S., Britto-Borges, T., Altmüller, J., Krüger, M., Dieterich, C., and Gehring, N.H. (2021). SMG5-SMG7 authorize nonsense-mediated mRNA decay by enabling SMG6 endonucleolytic activity. Nat. Commun. *12*, 3965. https://doi.org/10.1038/s41467-021-24046-3.
27. Karousis, E.D., Gypas, F., Zavolan, M., and Mühlemann, O. (2021). Nanopore sequencing reveals endogenous NMD-targeted isoforms in human cells. Genome Biol. *22*, 223. https://doi.org/10.1186/s13059-021-02439-3.
28. He, F., and Jacobson, A. (2015). Nonsense-Mediated mRNA Decay: Degradation of Defective Transcripts Is Only Part of the Story. Annu. Rev. Genet. *49*, 339–366. https://doi.org/10.1146/annurev-genet-112414-054639.
29. Bühler, M., Steiner, S., Mohn, F., Paillusson, A., and Mühlemann, O. (2006). EJC-independent degradation of nonsense immunoglobulin-mu mRNA depends on 3′ UTR length. Nat. Struct. Mol. Biol. *13*, 462–464. https://doi.org/10.1038/nsmb1081.
30. Hogg, J.R., and Goff, S.P. (2010). Upf1 senses 3′UTR length to potentiate mRNA decay. Cell *143*, 379–389. https://doi.org/10.1016/j.cell.2010.10.005.
31. Karousis, E.D., and Mühlemann, O. (2019). Nonsense-Mediated mRNA Decay Begins Where Translation Ends. Cold Spring Harb. Perspect. Biol. *11*, a032862. https://doi.org/10.1101/cshperspect.a032862.
32. Yamashita, A., Ohnishi, T., Kashima, I., Taya, Y., and Ohno, S. (2001). Human SMG-1, a novel phosphatidylinositol 3-kinase-related protein kinase, associates with components of the mRNA surveillance complex and is involved in the regulation of nonsense-mediated mRNA decay. Genes Dev. *15*, 2215–2228. https://doi.org/10.1101/gad.913001.
33. Eberle, A.B., Lykke-Andersen, S., Mühlemann, O., and Jensen, T.H. (2009). SMG6 promotes endonucleolytic cleavage of nonsense mRNA in human cells. Nat. Struct. Mol. Biol. *16*, 49–55. https://doi.org/10.1038/nsmb.1530.
34. Huntzinger, E., Kashima, I., Fauser, M., Saulière, J., and Izaurralde, E. (2008). SMG6 is the catalytic endonuclease that cleaves mRNAs containing nonsense codons in metazoan. RNA *14*, 2609–2617. https://doi.org/10.1261/rna.1386208.
35. Loh, B., Jonas, S., and Izaurralde, E. (2013). The SMG5-SMG7 heterodimer directly recruits the CCR4-NOT deadenylase complex to mRNAs containing nonsense codons via interaction with POP2. Genes Dev. *27*, 2125–2138. https://doi.org/10.1101/gad.226951.113.
36. Okada-Katsuhata, Y., Yamashita, A., Kutsuzawa, K., Izumi, N., Hirahara, F., and Ohno, S. (2012). N- and C-terminal Upf1 phosphorylations create binding platforms for SMG-6 and SMG-5:SMG-7 during NMD. Nucleic Acids Res. *40*, 1251–1266. https://doi.org/10.1093/nar/gkr791.
37. Chakrabarti, S., Bonneau, F., Schüssler, S., Eppinger, E., and Conti, E. (2014). Phospho-dependent and phospho-independent interactions of the helicase UPF1 with the NMD factors SMG5-SMG7 and SMG6. Nucleic Acids Res. *42*, 9447–9460. https://doi.org/10.1093/nar/gku578.
38. Han, X., Wei, Y., Wang, H., Wang, F., Ju, Z., and Li, T. (2018). Nonsense-mediated mRNA decay: a 'nonsense' pathway makes sense in stem cell biology. Nucleic Acids Res. *46*, 1038–1051. https://doi.org/10.1093/nar/gkx1272.
39. Medghalchi, S.M., Frischmeyer, P.A., Mendell, J.T., Kelly, A.G., Lawler, A. M., and Dietz, H.C. (2001). Rent1, a trans-effector of nonsense-mediated

mRNA decay, is essential for mammalian embryonic viability. Hum. Mol. Genet. *10*, 99–105. https://doi.org/10.1093/hmg/10.2.99.

40. Wittkopp, N., Huntzinger, E., Weiler, C., Saulière, J., Schmidt, S., Sonawane, M., and Izaurralde, E. (2009). Nonsense-mediated mRNA decay effectors are essential for zebrafish embryonic development and survival. Mol. Cell. Biol. *29*, 3517–3528. https://doi.org/10.1128/MCB.00177-09.
41. Metzstein, M.M., and Krasnow, M.A. (2006). Functions of the nonsense-mediated mRNA decay pathway in Drosophila development. PLoS Genet. *2*, e180. https://doi.org/10.1371/journal.pgen.0020180.
42. Petrić Howe, M., and Patani, R. (2023). Nonsense-mediated mRNA decay in neuronal physiology and neurodegeneration. Trends Neurosci. *46*, 879–892. https://doi.org/10.1016/j.tins.2023.07.001.
43. Jaffrey, S.R., and Wilkinson, M.F. (2018). Nonsense-mediated RNA decay in the brain: emerging modulator of neural development and disease. Nat. Rev. Neurosci. *19*, 715–728. https://doi.org/10.1038/s41583-018-0079-z.
44. Bartha, I., di Iulio, J., Venter, J.C., and Telenti, A. (2018). Human gene essentiality. Nat. Rev. Genet. *19*, 51–62. https://doi.org/10.1038/nrg.2017.75.
45. Dempster, J.M., Boyle, I., Vazquez, F., Root, D., Boehm, J.S., Hahn, W.C., Tsherniak, A., and McFarland, J.M. (2021). Chronos: a CRISPR cell population dynamics model. Genome Biol. *22*, 343. https://doi.org/10.1101/2021.02.25.432728.
46. Dempster, J.M., Rossen, J., Kazachkova, M., Pan, J., Kugener, G., Root, D.E., and Tsherniak, A. (2019). Extracting Biological Insights from the Project Achilles Genome-Scale CRISPR Screens in Cancer Cell Lines. Preprint at bioRxiv. https://doi.org/10.1101/720243.
47. DepMap, B. (2023). This DepMap release contains data from CRISPR knockout screens from project Achilles, as well as genomic characterization data from the CCLE project. For more information, please see README.txt. figshare. https://depmap.org/portal/data_page/?tab=allData&releasename=DepMap+Public+22Q2&filename=CCLE_expression.csv.
48. Meyers, R.M., Bryan, J.G., McFarland, J.M., Weir, B.A., Sizemore, A.E., Xu, H., Dharia, N.V., Montgomery, P.G., Cowley, G.S., Pantel, S., et al. (2017). Computational correction of copy number effect improves specificity of CRISPR-Cas9 essentiality screens in cancer cells. Nat. Genet. *49*, 1779–1784. https://doi.org/10.1038/ng.3984.
49. Pacini, C., Dempster, J.M., Boyle, I., Gonçalves, E., Najgebauer, H., Karakoc, E., van der Meer, D., Barthorpe, A., Lightfoot, H., Jaaks, P., et al. (2021). Integrated cross-study datasets of genetic dependencies in cancer. Nat. Commun. *12*, 1661. https://doi.org/10.1038/s41467-021-21898-7.
50. Tsherniak, A., Vazquez, F., Montgomery, P.G., Weir, B.A., Kryukov, G., Cowley, G.S., Gill, S., Harrington, W.F., Pantel, S., Krill-Burger, J.M., et al. (2017). Defining a Cancer Dependency Map. Cell *170*, 564–576.e16. https://doi.org/10.1016/j.cell.2017.06.010.
51. Kim, Y.K., and Maquat, L.E. (2019). UPFront and center in RNA decay: UPF1 in nonsense-mediated mRNA decay and beyond. RNA *25*, 407–422. https://doi.org/10.1261/rna.070136.118.
52. Lavysh, D., and Neu-Yilik, G. (2020). UPF1-Mediated RNA Decay-Danse Macabre in a Cloud. Biomolecules *10*, 999. https://doi.org/10.3390/biom10070999.
53. Cho, H., Park, O.H., Park, J., Ryu, I., Kim, J., Ko, J., and Kim, Y.K. (2015). Glucocorticoid receptor interacts with PNRC2 in a ligand-dependent manner to recruit UPF1 for rapid mRNA degradation. Proc. Natl. Acad. Sci. USA *112*, E1540–E1549. https://doi.org/10.1073/pnas.1409612112.
54. Kim, Y.K., Furic, L., Desgroseillers, L., and Maquat, L.E. (2005). Mammalian Staufen1 recruits Upf1 to specific mRNA 3′UTRs so as to elicit mRNA decay. Cell *120*, 195–208. https://doi.org/10.1016/j.cell.2004.11.050.
55. Fischer, J.W., Busa, V.F., Shao, Y., and Leung, A.K.L. (2020). Structure-Mediated RNA Decay by UPF1 and G3BP1. Mol. Cell *78*, 70–84.e6. https://doi.org/10.1016/j.molcel.2020.01.021.
56. Kaygun, H., and Marzluff, W.F. (2005). Regulated degradation of replication-dependent histone mRNAs requires both ATR and Upf1. Nat. Struct. Mol. Biol. *12*, 794–800. https://doi.org/10.1038/nsmb972.
57. Gowravaram, M., Schwarz, J., Khilji, S.K., Urlaub, H., and Chakrabarti, S. (2019). Insights into the assembly and architecture of a Staufen-mediated mRNA decay (SMD)-competent mRNP. Nat. Commun. *10*, 5054. https://doi.org/10.1038/s41467-019-13080-x.
58. Chapman, J.H., Craig, J.M., Wang, C.D., Gundlach, J.H., Neuman, K.C., and Hogg, J.R. (2022). UPF1 mutants with intact ATPase but deficient helicase activities promote efficient nonsense-mediated mRNA decay. Nucleic Acids Res. *50*, 11876–11894. https://doi.org/10.1093/nar/gkac1026.
59. Hurt, J.A., Robertson, A.D., and Burge, C.B. (2013). Global analyses of UPF1 binding and function reveal expanded scope of nonsense-mediated mRNA decay. Genome Res. *23*, 1636–1650. https://doi.org/10.1101/gr.157354.113.
60. Zünd, D., Gruber, A.R., Zavolan, M., and Mühlemann, O. (2013). Translation-dependent displacement of UPF1 from coding sequences causes its enrichment in 3′ UTRs. Nat. Struct. Mol. Biol. *20*, 936–943. https://doi.org/10.1038/nsmb.2635.
61. Lee, S.R., Pratt, G.A., Martinez, F.J., Yeo, G.W., and Lykke-Andersen, J. (2015). Target Discrimination in Nonsense-Mediated mRNA Decay Requires Upf1 ATPase Activity. Mol. Cell *59*, 413–425. https://doi.org/10.1016/j.molcel.2015.06.036.
62. Chen, S., Francioli, L.C., Goodrich, J.K., Collins, R.L., Kanai, M., Wang, Q., Alföldi, J., Watts, N.A., Vittal, C., Gauthier, L.D., et al. (2024). A genomic mutational constraint map using variation in 76,156 human genomes. Nature *625*, 92–100. https://doi.org/10.1038/s41586-023-06045-0.
63. Azzalin, C.M., and Lingner, J. (2006). The human RNA surveillance factor UPF1 is required for S phase progression and genome stability. Curr. Biol. *16*, 433–439. https://doi.org/10.1016/j.cub.2006.01.018.
64. Lou, C.H., Shao, A., Shum, E.Y., Espinoza, J.L., Huang, L., Karam, R., and Wilkinson, M.F. (2014). Posttranscriptional control of the stem cell and neurogenic programs by the nonsense-mediated RNA decay pathway. Cell Rep. *6*, 748–764. https://doi.org/10.1016/j.celrep.2014.01.028.
65. Mourtada-Maarabouni, M., and Williams, G.T. (2013). Growth arrest on inhibition of nonsense-mediated decay is mediated by noncoding RNA GAS5. BioMed Res. Int. *2013*, 358015. https://doi.org/10.1155/2013/358015.
66. Nelson, J.O., Moore, K.A., Chapin, A., Hollien, J., and Metzstein, M.M. (2016). Degradation of Gadd45 mRNA by nonsense-mediated decay is essential for viability. eLife *5*, e12876. https://doi.org/10.7554/eLife.12876.
67. Colombo, M., Karousis, E.D., Bourquin, J., Bruggmann, R., and Mühlemann, O. (2017). Transcriptome-wide identification of NMD-targeted human mRNAs reveals extensive redundancy between SMG6- and SMG7-mediated degradation pathways. RNA *23*, 189–201. https://doi.org/10.1261/rna.059055.116.
68. Huth, M., Santini, L., Galimberti, E., Ramesmayer, J., Titz-Teixeira, F., Sehlke, R., Oberhuemer, M., Stummer, S., Herzog, V., Garmhausen, M., et al. (2022). NMD is required for timely cell fate transitions by fine-tuning gene expression and regulating translation. Genes Dev. *36*, 348–367. https://doi.org/10.1101/gad.347690.120.
69. Britto-Borges, T., Gehring, N.H., Boehm, V., and Dieterich, C. (2024). NMDtxDB: data-driven identification and annotation of human NMD target transcripts. RNA *30*, 1277–1291. https://doi.org/10.1261/rna.080066.124.

Please cite this article in press as: Boehm et al., Rapid UPF1 depletion illuminates the temporal dynamics of the NMD-regulated human transcriptome, Molecular Cell (2025), https://doi.org/10.1016/j.molcel.2025.08.015

70. Mendell, J.T., ap Rhys, C.M.J., and Dietz, H.C. (2002). Separable roles for rent1/hUpf1 in altered splicing and decay of nonsense transcripts. Science *298*, 419–422. https://doi.org/10.1126/science.1074428.

71. Hannus, M., Beitzinger, M., Engelmann, J.C., Weickert, M.T., Spang, R., Hannus, S., and Meister, G. (2014). siPools: highly complex but accurately defined siRNA pools eliminate off-target effects. Nucleic Acids Res. *42*, 8049–8061. https://doi.org/10.1093/nar/gku480.

72. Sureau, A., Gattoni, R., Dooghe, Y., Stévenin, J., and Soret, J. (2001). SC35 autoregulates its expression by promoting splicing events that destabilize its mRNAs. EMBO J. *20*, 1785–1796. https://doi.org/10.1093/emboj/20.7.1785.

73. Lykke-Andersen, S., Chen, Y., Ardal, B.R., Lilje, B., Waage, J., Sandelin, A., and Jensen, T.H. (2014). Human nonsense-mediated RNA decay initiates widely by endonucleolysis and targets snoRNA host genes. Genes Dev. *28*, 2498–2517. https://doi.org/10.1101/gad.246538.114.

74. Zecha, J., Meng, C., Zolg, D.P., Samaras, P., Wilhelm, M., and Kuster, B. (2018). Peptide Level Turnover Measurements Enable the Study of Proteoform Dynamics. Mol. Cell. Proteomics *17*, 974–992. https://doi.org/10.1074/mcp.RA118.000583.

75. Wang, D., Eraslan, B., Wieland, T., Hallström, B., Hopf, T., Zolg, D.P., Zecha, J., Asplund, A., Li, L.H., Meng, C., et al. (2019). A deep proteome and transcriptome abundance atlas of 29 healthy human tissues. Mol. Syst. Biol. *15*, e8503. https://doi.org/10.15252/msb.20188503.

76. Nishimura, K., Fukagawa, T., Takisawa, H., Kakimoto, T., and Kanemaki, M. (2009). An auxin-based degron system for the rapid depletion of proteins in nonplant cells. Nat. Methods *6*, 917–922. https://doi.org/10.1038/nmeth.1401.

77. Li, S., Prasanna, X., Salo, V.T., Vattulainen, I., and Ikonen, E. (2019). An efficient auxin-inducible degron system with low basal degradation in human cells. Nat. Methods *16*, 866–869. https://doi.org/10.1038/s41592-019-0512-x.

78. Nabet, B., Roberts, J.M., Buckley, D.L., Paulk, J., Dastjerdi, S., Yang, A., Leggett, A.L., Erb, M.A., Lawlor, M.A., Souza, A., et al. (2018). The dTAG system for immediate and target-specific protein degradation. Nat. Chem. Biol. *14*, 431–441. https://doi.org/10.1038/s41589-018-0021-8.

79. Nabet, B., Ferguson, F.M., Seong, B.K.A., Kuljanin, M., Leggett, A.L., Mohardt, M.L., Robichaud, A., Conway, A.S., Buckley, D.L., Mancias, J.D., et al. (2020). Rapid and direct control of target protein levels with VHL-recruiting dTAG molecules. Nat. Commun. *11*, 4687. https://doi.org/10.1038/s41467-020-18377-w.

80. Viegas, M.H., Gehring, N.H., Breit, S., Hentze, M.W., and Kulozik, A.E. (2007). The abundance of RNPS1, a protein component of the exon junction complex, can determine the variability in efficiency of the Nonsense Mediated Decay pathway. Nucleic Acids Res. *35*, 4542–4551. https://doi.org/10.1093/nar/gkm461.

81. Gopalsamy, A., Bennett, E.M., Shi, M., Zhang, W.G., Bard, J., and Yu, K. (2012). Identification of pyrimidine derivatives as hSMG-1 inhibitors. Bioorg. Med. Chem. Lett. *22*, 6636–6641. https://doi.org/10.1016/j.bmcl.2012.08.107.

82. Kueckelmann, S., Theunissen, S., Lackmann, J.-W., Franitza, M., Becker, K., Boehm, V., and Gehring, N.H. (2024). SMG1:SMG8:SMG9-complex integrity maintains robustness of nonsense-mediated mRNA decay. Preprint at bioRxiv. https://doi.org/10.1101/2024.04.15.589496.

83. Kishor, A., Ge, Z., and Hogg, J.R. (2019). hnRNP L-dependent protection of normal mRNAs from NMD subverts quality control in B cell lymphoma. EMBO J. *38*, e99128. https://doi.org/10.15252/embj.201899128.

84. Longman, D., Jackson-Jones, K.A., Maslon, M.M., Murphy, L.C., Young, R.S., Stoddart, J.J., Hug, N., Taylor, M.S., Papadopoulos, D.K., and Cáceres, J.F. (2020). Identification of a localized nonsense-mediated decay pathway at the endoplasmic reticulum. Genes Dev. *34*, 1075–1088. https://doi.org/10.1101/gad.338061.120.

85. Fritz, S.E., Ranganathan, S., Wang, C.D., and Hogg, J.R. (2022). An alternative UPF1 isoform drives conditional remodeling of nonsense-mediated mRNA decay. EMBO J. *41*, e108898. https://doi.org/10.15252/embj.2021108898.

86. Hug, N., Aitken, S., Longman, D., Raab, M., Armes, H., Mann, A.R., Rio-Machin, A., Fitzgibbon, J., Rouault-Pierre, K., and Cáceres, J.F. (2022). A dual role for the RNA helicase DHX34 in NMD and pre-mRNA splicing and its function in hematopoietic differentiation. RNA *28*, 1224–1238. https://doi.org/10.1261/rna.079277.122.

87. Lee, S., Hwang, Y., Kim, T.H., Jeong, J., Choi, D., and Hwang, J. (2022). UPF1 Inhibits Hepatocellular Carcinoma Growth through DUSP1/p53 Signal Pathway. Biomedicines *10*, 793. https://doi.org/10.3390/biomedicines10040793.

88. He, P.C., Wei, J., Dou, X., Harada, B.T., Zhang, Z., Ge, R., Liu, C., Zhang, L.S., Yu, X., Wang, S., et al. (2023). Exon architecture controls mRNA m^{6}A suppression and gene expression. Science *379*, 677–682. https://doi.org/10.1126/science.abj9090.

89. Kanemaki, M.T. (2022). Ligand-induced degrons for studying nuclear functions. Curr. Opin. Cell Biol. *74*, 29–36. https://doi.org/10.1016/j.ceb.2021.12.006.

90. Fischer, D.S., Theis, F.J., and Yosef, N. (2018). Impulse model-based differential expression analysis of time course sequencing data. Nucleic Acids Res. *46*, e119. https://doi.org/10.1093/nar/gky675.

91. Chechik, G., and Koller, D. (2009). Timing of gene expression responses to environmental changes. J. Comput. Biol. *16*, 279–290. https://doi.org/10.1089/cmb.2008.13TT.

92. Kurosaki, T., Li, W., Hoque, M., Popp, M.W.L., Ermolenko, D.N., Tian, B., and Maquat, L.E. (2014). A post-translational regulatory switch on UPF1 controls targeted mRNA degradation. Genes Dev. *28*, 1900–1916. https://doi.org/10.1101/gad.245506.114.

93. Mukherjee, N., Calviello, L., Hirsekorn, A., de Pretis, S., Pelizzola, M., and Ohler, U. (2017). Integrative classification of human coding and noncoding genes through RNA metabolism profiles. Nat. Struct. Mol. Biol. *24*, 86–96. https://doi.org/10.1038/nsmb.3325.

94. Herzog, V.A., Reichholf, B., Neumann, T., Rescheneder, P., Bhat, P., Burkard, T.R., Wlotzka, W., von Haeseler, A., Zuber, J., and Ameres, S. L. (2017). Thiol-linked alkylation of RNA to assess expression dynamics. Nat. Methods *14*, 1198–1204. https://doi.org/10.1038/nmeth.4435.

95. Schofield, J.A., Duffy, E.E., Kiefer, L., Sullivan, M.C., and Simon, M.D. (2018). TimeLapse-seq: adding a temporal dimension to RNA sequencing through nucleoside recoding. Nat. Methods *15*, 221–225. https://doi.org/10.1038/nmeth.4582.

96. Vock, I.W., and Simon, M.D. (2023). bakR: uncovering differential RNA synthesis and degradation kinetics transcriptome-wide with Bayesian hierarchical modeling. RNA *29*, 958–976. https://doi.org/10.1261/rna.079451.122.

97. Calviello, L., Sydow, D., Harnett, D., and Ohler, U. (2019). Ribo-seQC: comprehensive analysis of cytoplasmic and organellar ribosome profiling data. Preprint at bioRxiv. https://doi.org/10.1101/601468.

98. Choe, J., Ahn, S.H., and Kim, Y.K. (2014). The mRNP remodeling mediated by UPF1 promotes rapid degradation of replication-dependent histone mRNA. Nucleic Acids Res. *42*, 9334–9349. https://doi.org/10.1093/nar/gku610.

99. Soneson, C., Love, M.I., and Robinson, M.D. (2015). Differential analyses for RNA-seq: transcript-level estimates improve gene-level inferences. F1000Res *4*, 1521. https://doi.org/10.12688/f1000research.7563.2.

100. Baldoni, P.L., Chen, Y., Hediyeh-Zadeh, S., Liao, Y., Dong, X., Ritchie, M. E., Shi, W., and Smyth, G.K. (2024). Dividing out quantification uncertainty allows efficient assessment of differential transcript expression with edgeR. Nucleic Acids Res. *52*, e13. https://doi.org/10.1093/nar/gkad1167.

101. Pardo-Palacios, F.J., Wang, D., Reese, F., Diekhans, M., Carbonell-Sala, S., Williams, B., Loveland, J.E., De María, M., Adams, M.S., Balderrama-Gutierrez, G., et al. (2024). Systematic assessment of long-read RNA-seq

methods for transcript identification and quantification. Nat. Methods *21*, 1349–1363. https://doi.org/10.1038/s41592-024-02298-3.

102. Su, Y., Yu, Z., Jin, S., Ai, Z., Yuan, R., Chen, X., Xue, Z., Guo, Y., Chen, D., Liang, H., et al. (2024). Comprehensive assessment of mRNA isoform detection methods for long-read sequencing data. Nat. Commun. *15*, 3972. https://doi.org/10.1038/s41467-024-48117-3.

103. Chen, Y., Sim, A., Wan, Y.K., Yeo, K., Lee, J.J.X., Ling, M.H., Love, M.I., and Göke, J. (2023). Context-aware transcript quantification from long-read RNA-seq data with Bambu. Nat. Methods *20*, 1187–1195. https://doi.org/10.1038/s41592-023-01908-w.

104. Kovaka, S., Zimin, A.V., Pertea, G.M., Razaghi, R., Salzberg, S.L., and Pertea, M. (2019). Transcriptome assembly from long-read RNA-seq alignments with StringTie2. Genome Biol. *20*, 278. https://doi.org/10.1186/s13059-019-1910-1.

105. Prjibelski, A.D., Mikheenko, A., Joglekar, A., Smetanin, A., Jarroux, J., Lapidus, A.L., and Tilgner, H.U. (2023). Accurate isoform discovery with IsoQuant using long reads. Nat. Biotechnol. *41*, 915–918. https://doi.org/10.1038/s41587-022-01565-y.

106. Dong, X., Du, M.R.M., Gouil, Q., Tian, L., Jabbari, J.S., Bowden, R., Baldoni, P.L., Chen, Y., Smyth, G.K., Amarasinghe, S.L., et al. (2023). Benchmarking long-read RNA-sequencing analysis tools using in silico mixtures. Nat. Methods *20*, 1810–1821. https://doi.org/10.1038/s41592-023-02026-3.

107. Pardo-Palacios, F.J., Arzalluz-Luque, A., Kondratova, L., Salguero, P., Mestre-Tomás, J., Amorín, R., Estevan-Morió, E., Liu, T., Nanni, A., McIntyre, L., et al. (2024). SQANTI3: curation of long-read transcriptomes for accurate identification of known and novel isoforms. Nat. Methods *21*, 793–797. https://doi.org/10.1038/s41592-024-02229-2.

108. Chao, K.H., Mao, A., Salzberg, S.L., and Pertea, M. (2024). Splam: a deep-learning-based splice site predictor that improves spliced alignments. Genome Biol. *25*, 243. https://doi.org/10.1186/s13059-024-03379-4.

109. French, C.E., Wei, G., Lloyd, J.P.B., Hu, Z., Brooks, A.N., and Brenner, S. E. (2020). Transcriptome analysis of alternative splicing-coupled nonsense-mediated mRNA decay in human cells reveals broad regulatory potential. Preprint at bioRxiv. https://doi.org/10.1101/2020.07.01.183327.

110. Lindeboom, R.G.H., Supek, F., and Lehner, B. (2016). The rules and impact of nonsense-mediated mRNA decay in human cancers. Nat. Genet. *48*, 1112–1118. https://doi.org/10.1038/ng.3664.

111. Rivas, M.A., Pirinen, M., Conrad, D.F., Lek, M., Tsang, E.K., Karczewski, K.J., Maller, J.B., Kukurba, K.R., DeLuca, D.S., Fromer, M., et al. (2015). Human genomics. Effect of predicted protein-truncating genetic variants on the human transcriptome. Science *348*, 666–669. https://doi.org/10.1126/science.1261877.

112. Calviello, L., Hirsekorn, A., and Ohler, U. (2020). Quantification of translation uncovers the functions of the alternative transcriptome. Nat. Struct. Mol. Biol. *27*, 717–725. https://doi.org/10.1038/s41594-020-0450-4.

113. Zhang, P., He, D., Xu, Y., Hou, J., Pan, B.F., Wang, Y., Liu, T., Davis, C.M., Ehli, E.A., Tan, L., et al. (2017). Genome-wide identification and differential analysis of translational initiation. Nat. Commun. *8*, 1749. https://doi.org/10.1038/s41467-017-01981-8.

114. Cmero, M., Davidson, N.M., and Oshlack, A. (2019). Using equivalence class counts for fast and accurate testing of differential transcript usage. F1000Res *8*, 265. https://doi.org/10.12688/f1000research.18276.2.

115. Schmidt, S.A., Foley, P.L., Jeong, D.H., Rymarquis, L.A., Doyle, F., Tenenbaum, S.A., Belasco, J.G., and Green, P.J. (2015). Identification of SMG6 cleavage sites and a preferred RNA cleavage motif by global analysis of endogenous NMD targets in human cells. Nucleic Acids Res. *43*, 309–323. https://doi.org/10.1093/nar/gku1258.

116. Berry, S., and Pelkmans, L. (2022). Mechanisms of cellular mRNA transcript homeostasis. Trends Cell Biol. *32*, 655–668. https://doi.org/10.1016/j.tcb.2022.05.003.

117. Mino, T., Murakawa, Y., Fukao, A., Vandenbon, A., Wessels, H.H., Ori, D., Uehata, T., Tartey, S., Akira, S., Suzuki, Y., et al. (2015). Regnase-1 and Roquin Regulate a Common Element in Inflammatory mRNAs by Spatiotemporally Distinct Mechanisms. Cell *161*, 1058–1073. https://doi.org/10.1016/j.cell.2015.04.029.

118. Sugimoto, Y., Vigilante, A., Darbo, E., Zirra, A., Militti, C., D'Ambrogio, A., Luscombe, N.M., and Ule, J. (2015). hiCLIP reveals the in vivo atlas of mRNA secondary structures recognized by Staufen 1. Nature *519*, 491–494. https://doi.org/10.1038/nature14280.

119. Toma, K.G., Rebbapragada, I., Durand, S., and Lykke-Andersen, J. (2015). Identification of elements in human long 3′ UTRs that inhibit nonsense-mediated decay. RNA *21*, 887–897. https://doi.org/10.1261/rna.048637.114.

120. Kim, Y.K., Furic, L., Parisien, M., Major, F., DesGroseillers, L., and Maquat, L.E. (2007). Staufen1 regulates diverse classes of mammalian transcripts. EMBO J. *26*, 2670–2681. https://doi.org/10.1038/sj.emboj.7601712.

121. Gong, C., Kim, Y.K., Woeller, C.F., Tang, Y., and Maquat, L.E. (2009). SMD and NMD are competitive pathways that contribute to myogenesis: effects on PAX3 and myogenin mRNAs. Genes Dev. *23*, 54–66. https://doi.org/10.1101/gad.1717309.

122. Ricci, E.P., Kucukural, A., Cenik, C., Mercier, B.C., Singh, G., Heyer, E.E., Ashar-Patel, A., Peng, L., and Moore, M.J. (2014). Staufen1 senses overall transcript secondary structure to regulate translation. Nat. Struct. Mol. Biol. *21*, 26–35. https://doi.org/10.1038/nsmb.2739.

123. Zheng, D., Cho, H., Wang, W., Rambout, X., Tian, B., and Maquat, L.E. (2020). 3′READS + RIP defines differential Staufen1 binding to alternative 3′UTR isoforms and reveals structures and sequence motifs influencing binding and polysome association. RNA *26*, 1621–1636. https://doi.org/10.1261/rna.076133.120.

124. Mino, T., Iwai, N., Endo, M., Inoue, K., Akaki, K., Hia, F., Uehata, T., Emura, T., Hidaka, K., Suzuki, Y., et al. (2019). Translation-dependent unwinding of stem-loops by UPF1 licenses Regnase-1 to degrade inflammatory mRNAs. Nucleic Acids Res. *47*, 8838–8859. https://doi.org/10.1093/nar/gkz628.

125. Yadav, D.K., Zigáčková, D., Zlobina, M., Klumpler, T., Beaumont, C., Kubíčková, M., Vaňáčová, Š., and Lukavsky, P.J. (2020). Staufen1 reads out structure and sequence features in ARF1 dsRNA for target recognition. Nucleic Acids Res. *48*, 2091–2106. https://doi.org/10.1093/nar/gkz1163.

126. Imamachi, N., Salam, K.A., Suzuki, Y., and Akimitsu, N. (2017). A GC-rich sequence feature in the 3′ UTR directs UPF1-dependent mRNA decay in mammalian cells. Genome Res. *27*, 407–418. https://doi.org/10.1101/gr.206060.116.

127. Kursa, M.B., and Rudnicki, W.R. (2010). Feature Selection with the Boruta Package. J. Stat. Software *36*, 1–13. https://doi.org/10.18637/jss.v036.i11.

128. Mudge, J.M., Ruiz-Orera, J., Prensner, J.R., Brunet, M.A., Calvet, F., Jungreis, I., Gonzalez, J.M., Magrane, M., Martinez, T.F., Schulz, J.F., et al. (2022). Standardized annotation of translated open reading frames. Nat. Biotechnol. *40*, 994–999. https://doi.org/10.1038/s41587-022-01369-0.

129. Chothani, S.P., Adami, E., Widjaja, A.A., Langley, S.R., Viswanathan, S., Pua, C.J., Zhihao, N.T., Harmston, N., D'Agostino, G., Whiffin, N., et al. (2022). A high-resolution map of human RNA translation. Mol. Cell *82*, 2885–2899.e8. https://doi.org/10.1016/j.molcel.2022.06.023.

130. Tani, H., Imamachi, N., Salam, K.A., Mizutani, R., Ijiri, K., Irie, T., Yada, T., Suzuki, Y., and Akimitsu, N. (2012). Identification of hundreds of novel UPF1 target transcripts by direct determination of whole transcriptome stability. RNA Biol. *9*, 1370–1379. https://doi.org/10.4161/rna.22360.

131. Mendell, J.T., Sharifi, N.A., Meyers, J.L., Martinez-Murillo, F., and Dietz, H.C. (2004). Nonsense surveillance regulates expression of diverse classes of mammalian transcripts and mutes genomic noise. Nat. Genet. *36*, 1073–1078. https://doi.org/10.1038/ng1429.

132. Sieber, J., Hauer, C., Bhuvanagiri, M., Leicht, S., Krijgsveld, J., Neu-Yilik, G., Hentze, M.W., and Kulozik, A.E. (2016). Proteomic Analysis Reveals Branch-specific Regulation of the Unfolded Protein Response by Nonsense-mediated mRNA Decay. Mol. Cell. Proteomics *15*, 1584–1597. https://doi.org/10.1074/mcp.M115.054056.

133. Huang, Y., Triscari, J.M., Tseng, G.C., Pasa-Tolic, L., Lipton, M.S., Smith, R.D., and Wysocki, V.H. (2005). Statistical characterization of the charge state and residue dependence of low-energy CID peptide dissociation patterns. Anal. Chem. *77*, 5800–5813. https://doi.org/10.1021/ac0480949.

134. Koudelka, T., Winkels, K., Kaleja, P., and Tholey, A. (2022). Shedding light on both ends: An update on analytical approaches for N- and C-terminomics. Biochim. Biophys. Acta Mol. Cell Res. *1869*, 119137. https://doi.org/10.1016/j.bbamcr.2021.119137.

135. Sinitcyn, P., Richards, A.L., Weatheritt, R.J., Brademan, D.R., Marx, H., Shishkova, E., Meyer, J.G., Hebert, A.S., Westphall, M.S., Blencowe, B.J., et al. (2023). Global detection of human variants and isoforms by deep proteome sequencing. Nat. Biotechnol. *41*, 1776–1786. https://doi.org/10.1038/s41587-023-01714-x.

136. Riley, R.M., Spencer Miko, S.E., S.E., Morin, R.D., Morin, G.B., and Negri, G.L. (2023). PeptideRanger: An R Package to Optimize Synthetic Peptide Selection for Mass Spectrometry Applications. J. Proteome Res. *22*, 526–531. https://doi.org/10.1021/acs.jproteome.2c00538.

137. Demichev, V., Messner, C.B., Vernardis, S.I., Lilley, K.S., and Ralser, M. (2020). DIA-NN: neural networks and interference correction enable deep proteome coverage in high throughput. Nat. Methods *17*, 41–44. https://doi.org/10.1038/s41592-019-0638-x.

138. Cascarina, S.M., and Ross, E.D. (2022). Expansion and functional analysis of the SR-related protein family across the domains of life. RNA *28*, 1298–1314. https://doi.org/10.1261/rna.079170.122.

139. Yang, F., Bian, T., Zhan, X., Chen, Z., Xing, Z., Larsen, N.A., Zhang, X., and Shi, Y. (2023). Mechanisms of the RNA helicases DDX42 and DDX46 in human U2 snRNP assembly. Nat. Commun. *14*, 897. https://doi.org/10.1038/s41467-023-36489-x.

140. Glasser, E., Maji, D., Biancon, G., Puthenpeedikakkal, A.M.K., Cavender, C.E., Tebaldi, T., Jenkins, J.L., Mathews, D.H., Halene, S., and Kielkopf, C.L. (2022). Pre-mRNA splicing factor U2AF2 recognizes distinct conformations of nucleotide variants at the center of the pre-mRNA splice site signal. Nucleic Acids Res. *50*, 5299–5312. https://doi.org/10.1093/nar/gkac287.

141. Suzuki, I.K., Gacquer, D., Van Heurck, R., Kumar, D., Wojno, M., Bilheu, A., Herpoel, A., Lambert, N., Cheron, J., Polleux, F., et al. (2018). Human-Specific NOTCH2NL Genes Expand Cortical Neurogenesis through Delta/Notch Regulation. Cell *173*, 1370–1384.e16. https://doi.org/10.1016/j.cell.2018.03.067.

142. Van Heurck, R., Bonnefont, J., Wojno, M., Suzuki, I.K., Velez-Bravo, F.D., Erkol, E., Nguyen, D.T., Herpoel, A., Bilheu, A., Beckers, S., et al. (2023). CROCCP2 acts as a human-specific modifier of cilia dynamics and mTOR signaling to promote expansion of cortical progenitors. Neuron *111*, 65–80.e6. https://doi.org/10.1016/j.neuron.2022.10.018.

143. Astling, D.P., Heft, I.E., Jones, K.L., and Sikela, J.M. (2017). High resolution measurement of DUF1220 domain copy number from whole genome sequence data. BMC Genomics *18*, 614. https://doi.org/10.1186/s12864-017-3976-z.

144. Dumas, L.J., O'Bleness, M.S., Davis, J.M., Dickens, C.M., Anderson, N., Keeney, J.G., Jackson, J., Sikela, M., Raznahan, A., Giedd, J., et al. (2012). DUF1220-domain copy number implicated in human brain-size pathology and evolution. Am. J. Hum. Genet. *91*, 444–454. https://doi.org/10.1016/j.ajhg.2012.07.016.

145. Davis, J.M., Heft, I., Scherer, S.W., and Sikela, J.M. (2019). A Third Linear Association Between Olduvai (DUF1220) Copy Number and Severity of the Classic Symptoms of Inherited Autism. Am. J. Psychiatry *176*, 643–650. https://doi.org/10.1176/appi.ajp.2018.18080993.

146. Keeney, J.G., Davis, J.M., Siegenthaler, J., Post, M.D., Nielsen, B.S., Hopkins, W.D., and Sikela, J.M. (2015). DUF1220 protein domains drive proliferation in human neural stem cells and are associated with increased cortical volume in anthropoid primates. Brain Struct. Funct. *220*, 3053–3060. https://doi.org/10.1007/s00429-014-0814-9.

147. Leeds, P., Peltz, S.W., Jacobson, A., and Culbertson, M.R. (1991). The product of the yeast UPF1 gene is required for rapid turnover of mRNAs containing a premature translational termination codon. Genes Dev. *5*, 2303–2314. https://doi.org/10.1101/gad.5.12a.2303.

148. Sun, X., Perlick, H.A., Dietz, H.C., and Maquat, L.E. (1998). A mutated human homologue to yeast Upf1 protein has a dominant-negative effect on the decay of nonsense-containing mRNAs in mammalian cells. Proc. Natl. Acad. Sci. USA *95*, 10009–10014. https://doi.org/10.1073/pnas.95.17.10009.

149. Durand, S., and Lykke-Andersen, J. (2013). Nonsense-mediated mRNA decay occurs during eIF4F-dependent translation in human cells. Nat. Struct. Mol. Biol. *20*, 702–709. https://doi.org/10.1038/nsmb.2575.

150. Hoek, T.A., Khuperkar, D., Lindeboom, R.G.H., Sonneveld, S., Verhagen, B.M.P., Boersma, S., Vermeulen, M., and Tanenbaum, M.E. (2019). Single-Molecule Imaging Uncovers Rules Governing Nonsense-Mediated mRNA Decay. Mol. Cell *75*, 324–339.e11. https://doi.org/10.1016/j.molcel.2019.05.008.

151. Rufener, S.C., and Mühlemann, O. (2013). eIF4E-bound mRNPs are substrates for nonsense-mediated mRNA decay in mammalian cells. Nat. Struct. Mol. Biol. *20*, 710–717. https://doi.org/10.1038/nsmb.2576.

152. Robinson, J.T., Thorvaldsdottir, H., Turner, D., and Mesirov, J.P. (2023). igv.js: an embeddable JavaScript implementation of the Integrative Genomics Viewer (IGV). Bioinformatics *39*, btac830. https://doi.org/10.1093/bioinformatics/btac830.

153. Perez-Riverol, Y., Bandla, C., Kundu, D.J., Kamatchinathan, S., Bai, J., Hewapathirana, S., John, N.S., Prakash, A., Walzer, M., Wang, S., et al. (2025). The PRIDE database at 20 years: 2025 update. Nucleic Acids Res. *53*, D543–D553. https://doi.org/10.1093/nar/gkae1011.

154. Oberacker, P., Stepper, P., Bond, D.M., Höhn, S., Focken, J., Meyer, V., Schelle, L., Sugrue, V.J., Jeunen, G.J., Moser, T., et al. (2019). Bio-On-Magnetic-Beads (BOMB): Open platform for high-throughput nucleic acid extraction and manipulation. PLoS Biol. *17*, e3000107. https://doi.org/10.1371/journal.pbio.3000107.

155. Wallmeroth, D., Lackmann, J.W., Kueckelmann, S., Altmüller, J., Dieterich, C., Boehm, V., and Gehring, N.H. (2022). Human UPF3A and UPF3B enable fault-tolerant activation of nonsense-mediated mRNA decay. EMBO J. *41*, e109191. https://doi.org/10.15252/embj.2021109191.

156. Gerbracht, J.V., Boehm, V., Britto-Borges, T., Kallabis, S., Wiederstein, J. L., Ciriello, S., Aschemeier, D.U., Krüger, M., Frese, C.K., Altmüller, J., et al. (2020). CASC3 promotes transcriptome-wide activation of nonsense-mediated decay by the exon junction complex. Nucleic Acids Res. *48*, 8626–8644. https://doi.org/10.1093/nar/gkaa564.

157. Zhu, A., Ibrahim, J.G., and Love, M.I. (2019). Heavy-tailed prior distributions for sequence count data: removing the noise and preserving large differences. Bioinformatics *35*, 2084–2092. https://doi.org/10.1093/bioinformatics/bty895.

158. Langmead, B., and Salzberg, S.L. (2012). Fast gapped-read alignment with Bowtie 2. Nat. Methods *9*, 357–359. https://doi.org/10.1038/nmeth.1923.

159. Silvestre-Ryan, J., Fletcher, D.A., and Holmes, I. (2022). CellScape: Protein structure visualization with vector graphics cartoons. Preprint at bioRxiv. https://doi.org/10.1101/2022.06.14.495869.

160. Pettersen, E.F., Goddard, T.D., Huang, C.C., Meng, E.C., Couch, G.S., Croll, T.I., Morris, J.H., and Ferrin, T.E. (2021). UCSF ChimeraX: Structure visualization for researchers, educators, and developers. Protein Sci. *30*, 70–82. https://doi.org/10.1002/pro.3943.

161. Gu, Z., Eils, R., and Schlesner, M. (2016). Complex heatmaps reveal patterns and correlations in multidimensional genomic data. Bioinformatics *32*, 2847–2849. https://doi.org/10.1093/bioinformatics/btw313.

162. Love, M.I., Huber, W., and Anders, S. (2014). Moderated estimation of fold change and dispersion for RNA-seq data with DESeq2. Genome Biol. *15*, 550. https://doi.org/10.1186/s13059-014-0550-8.

163. Robinson, M.D., McCarthy, D.J., and Smyth, G.K. (2010). edgeR: a Bioconductor package for differential expression analysis of digital gene expression data. Bioinformatics *26*, 139–140. https://doi.org/10.1093/bioinformatics/btp616.

164. Vock, I.W., Mabin, J.W., Machyna, M., Zhang, A., Hogg, J.R., and Simon, M.D. (2024). Expanding and improving analyses of nucleotide recoding RNA-seq experiments with the EZbakR suite. Preprint at bioRxiv. https://doi.org/10.1101/2024.10.14.617411.

165. Hamid, F., Alasoo, K., Vilo, J., and Makeyev, E. (2022). Functional Annotation of Custom Transcriptomes. Methods Mol. Biol. *2537*, 149–172. https://doi.org/10.1007/978-1-0716-2521-7_9.

166. Pertea, G., and Pertea, M. (2020). GFF Utilities: GffRead and GffCompare. F1000Res *9*, ISCBCommJ-304. https://doi.org/10.12688/f1000research.23297.2.

167. Kolberg, L., Raudvere, U., Kuzmin, I., Adler, P., Vilo, J., and Peterson, H. (2023). g:Profiler-interoperable web service for functional enrichment analysis and gene identifier mapping (2023 update). Nucleic Acids Res. *51*, W207–W212. https://doi.org/10.1093/nar/gkad347.

168. Robinson, J.T., Thorvaldsdóttir, H., Winckler, W., Guttman, M., Lander, E.S., Getz, G., and Mesirov, J.P. (2011). Integrative genomics viewer. Nat. Biotechnol. *29*, 24–26. https://doi.org/10.1038/nbt.1754.

169. Jones, P., Binns, D., Chang, H.Y., Fraser, M., Li, W., McAnulla, C., McWilliam, H., Maslen, J., Mitchell, A., Nuka, G., et al. (2014). InterProScan 5: genome-scale protein function classification. Bioinformatics *30*, 1236–1240. https://doi.org/10.1093/bioinformatics/btu031.

170. Vitting-Seerup, K., and Sandelin, A. (2017). The Landscape of Isoform Switches in Human Cancers. Mol. Cancer Res. *15*, 1206–1220. https://doi.org/10.1158/1541-7786.MCR-16-0459.

171. Li, Y.I., Knowles, D.A., Humphrey, J., Barbeira, A.N., Dickinson, S.P., Im, H.K., and Pritchard, J.K. (2018). Annotation-free quantification of RNA splicing using LeafCutter. Nat. Genet. *50*, 151–158. https://doi.org/10.1038/s41588-017-0004-9.

172. Li, H. (2018). Minimap2: pairwise alignment for nucleotide sequences. Bioinformatics *34*, 3094–3100. https://doi.org/10.1093/bioinformatics/bty191.

173. Ewels, P., Magnusson, M., Lundin, S., and Käller, M. (2016). MultiQC: summarize analysis results for multiple tools and samples in a single report. Bioinformatics *32*, 3047–3048. https://doi.org/10.1093/bioinformatics/btw354.

174. Pérez-Silva, J.G., Araujo-Voces, M., and Quesada, V. (2018). nVenn: generalized, quasi-proportional Venn and Euler diagrams. Bioinformatics *34*, 2322–2324. https://doi.org/10.1093/bioinformatics/bty109.

175. Varabyou, A., Erdogdu, B., Salzberg, S.L., and Pertea, M. (2023). Investigating Open Reading Frames in Known and Novel Transcripts using ORFanage. Nat Comput. Sci. *3*, 700–708. https://doi.org/10.1038/s43588-023-00496-1.

176. Tjeldnes, H., Labun, K., Torres Cleuren, Y., Chyżyńska, K., Świrski, M., and Valen, E. (2021). ORFik: a comprehensive R toolkit for the analysis of translation. BMC Bioinformatics *22*, 336. https://doi.org/10.1186/s12859-021-04254-w.

177. Herrmann, C.J., Schmidt, R., Kanitz, A., Artimo, P., Gruber, A.J., and Zavolan, M. (2020). PolyASite 2.0: a consolidated atlas of polyadenylation sites from 3′ end sequencing. Nucleic Acids Res. *48*, D174–D179. https://doi.org/10.1093/nar/gkz918.

178. Abugessaisa, I., Noguchi, S., Hasegawa, A., Kondo, A., Kawaji, H., Carninci, P., and Kasukawa, T. (2019). refTSS: A Reference Data Set for Human and Mouse Transcription Start Sites. J. Mol. Biol. *431*, 2407–2422. https://doi.org/10.1016/j.jmb.2019.04.045.

179. Lorenz, R., Bernhart, S.H., Höner Zu Siederdissen, C., Tafer, H., Flamm, C., Stadler, P.F., and Hofacker, I.L. (2011). ViennaRNA Package 2.0. Algorithms Mol. Biol. *6*, 26. https://doi.org/10.1186/1748-7188-6-26.

180. Sayols, S. (2023). rrvgo: a Bioconductor package for interpreting lists of Gene Ontology terms. MicroPubl Biol. *2023*. https://doi.org/10.17912/micropub.biology.000811.

181. Liao, Y., Smyth, G.K., and Shi, W. (2014). featureCounts: an efficient general purpose program for assigning sequence reads to genomic features. Bioinformatics *30*, 923–930. https://doi.org/10.1093/bioinformatics/btt656.

182. Patro, R., Duggal, G., Love, M.I., Irizarry, R.A., and Kingsford, C. (2017). Salmon provides fast and bias-aware quantification of transcript expression. Nat. Methods *14*, 417–419. https://doi.org/10.1038/nmeth.4197.

183. Dobin, A., Davis, C.A., Schlesinger, F., Drenkow, J., Zaleski, C., Jha, S., Batut, P., Chaisson, M., and Gingeras, T.R. (2013). STAR: ultrafast universal RNA-seq aligner. Bioinformatics *29*, 15–21. https://doi.org/10.1093/bioinformatics/bts635.

184. Smith, T., Heger, A., and Sudbery, I. (2017). UMI-tools: modeling sequencing errors in Unique Molecular Identifiers to improve quantification accuracy. Genome Res. *27*, 491–499. https://doi.org/10.1101/gr.209601.116.

185. Jumper, J., Evans, R., Pritzel, A., Green, T., Figurnov, M., Ronneberger, O., Tunyasuvunakool, K., Bates, R., Žídek, A., Potapenko, A., et al. (2021). Highly accurate protein structure prediction with AlphaFold. Nature *596*, 583–589. https://doi.org/10.1038/s41586-021-03819-2.

186. Varadi, M., Anyango, S., Deshpande, M., Nair, S., Natassia, C., Yordanova, G., Yuan, D., Stroe, O., Wood, G., Laydon, A., et al. (2022). AlphaFold Protein Structure Database: massively expanding the structural coverage of protein-sequence space with high-accuracy models. Nucleic Acids Res. *50*, D439–D444. https://doi.org/10.1093/nar/gkab1061.

187. Chakrabarti, S., Jayachandran, U., Bonneau, F., Fiorini, F., Basquin, C., Domcke, S., Le Hir, H., and Conti, E. (2011). Molecular mechanisms for the RNA-dependent ATPase activity of Upf1 and its regulation by Upf2. Mol. Cell *41*, 693–703. https://doi.org/10.1016/j.molcel.2011.02.010.

188. Ritchie, M.E., Phipson, B., Wu, D., Hu, Y., Law, C.W., Shi, W., and Smyth, G.K. (2015). limma powers differential expression analyses for RNA-sequencing and microarray studies. Nucleic Acids Res. *43*, e47. https://doi.org/10.1093/nar/gkv007.

189. Sakuma, T., Nakade, S., Sakane, Y., Suzuki, K.T., and Yamamoto, T. (2016). MMEJ-assisted gene knock-in using TALENs and CRISPR-Cas9 with the PITCh systems. Nat. Protoc. *11*, 118–133. https://doi.org/10.1038/nprot.2015.140.

190. Barrett, T., Wilhite, S.E., Ledoux, P., Evangelista, C., Kim, I.F., Tomashevsky, M., Marshall, K.A., Phillippy, K.H., Sherman, P.M., Holko, M., et al. (2013). NCBI GEO: archive for functional genomics data sets–update. Nucleic Acids Res. *41*, D991–D995. https://doi.org/10.1093/nar/gks1193.

191. Sarkans, U., Gostev, M., Athar, A., Behrangi, E., Melnichuk, O., Ali, A., Minguet, J., Rada, J.C., Snow, C., Tikhonov, A., et al. (2018). The BioStudies database-one stop shop for all data supporting a life sciences study. Nucleic Acids Res. *46*, D1266–D1270. https://doi.org/10.1093/nar/gkx965.

192. Sarkans, U., Füllgrabe, A., Ali, A., Athar, A., Behrangi, E., Diaz, N., Fexova, S., George, N., Iqbal, H., Kurri, S., et al. (2021). From

Please cite this article in press as: Boehm et al., Rapid UPF1 depletion illuminates the temporal dynamics of the NMD-regulated human transcriptome, Molecular Cell (2025), https://doi.org/10.1016/j.molcel.2025.08.015

ArrayExpress to BioStudies. Nucleic Acids Res. *49*, D1502–D1506. https://doi.org/10.1093/nar/gkaa1062.

193. R Core Team (2023). R: A Language and Environment for Statistical Computing (R Foundation for Statistical Computing).
194. Yang, L., Duff, M.O., Graveley, B.R., Carmichael, G.G., and Chen, L.L. (2011). Genomewide characterization of non-polyadenylated RNAs. Genome Biol. *12*, R16. https://doi.org/10.1186/gb-2011-12-2-r16.
195. Zhu, A., Srivastava, A., Ibrahim, J.G., Patro, R., and Love, M.I. (2019). Nonparametric expression analysis using inferential replicate counts. Nucleic Acids Res. *47*, e105. https://doi.org/10.1093/nar/gkz622.
196. Anders, S., Reyes, A., and Huber, W. (2012). Detecting differential usage of exons from RNA-seq data. Genome Res. *22*, 2008–2017. https://doi.org/10.1101/gr.133744.111.
197. Nersisyan, L., Ropat, M., and Pelechano, V. (2020). Improved computational analysis of ribosome dynamics from 5′P degradome data using fivepseq. NAR Genom. Bioinform. *2*, lqaa099. https://doi.org/10.1093/nargab/lqaa099.
198. Mabin, J.W., Vock, I.W., Machyna, M., Haque, N., Thakran, P., Zhang, A., Rai, G., Leibler, I.N.-M., Inglese, J., Simon, M.D., et al. (2025). Uncovering the isoform-resolution kinetic landscape of nonsense-mediated mRNA decay with EZbakR. Preprint at bioRxiv. https://doi.org/10.1101/2025.03.12.642874.
199. Ingolia, N.T., Ghaemmaghami, S., Newman, J.R.S., and Weissman, J.S. (2009). Genome-wide analysis in vivo of translation with nucleotide resolution using ribosome profiling. Science *324*, 218–223. https://doi.org/10.1126/science.1168978.
200. Chothani, S., Adami, E., Ouyang, J.F., Viswanathan, S., Hubner, N., Cook, S.A., Schafer, S., and Rackham, O.J.L. (2019). deltaTE: Detection of Translationally Regulated Genes by Integrative Analysis of Ribo-seq and RNA-seq Data. Curr. Protoc. Mol. Biol. *129*, e108. https://doi.org/10.1002/cpmb.108.
201. Seal, R.L., Denny, P., Bruford, E.A., Gribkova, A.K., Landsman, D., Marzluff, W.F., McAndrews, M., Panchenko, A.R., Shaytan, A.K., and Talbert, P.B. (2022). A standardized nomenclature for mammalian histone genes. Epigenetics Chromatin *15*, 34. https://doi.org/10.1186/s13072-022-00467-2.
202. Wickham, H. (2016). ggplot2: Elegant Graphics for Data Analysis (Springer-Verlag).

Please cite this article in press as: Boehm et al., Rapid UPF1 depletion illuminates the temporal dynamics of the NMD-regulated human transcriptome, Molecular Cell (2025), https://doi.org/10.1016/j.molcel.2025.08.015

STAR★METHODS

KEY RESOURCES TABLE

REAGENT or RESOURCE	SOURCE	IDENTIFIER
Antibodies		
Goat polyclonal anti-UPF1	Bethyl	Cat# A300-038A-M; RRID:AB_2778977
Mouse monoclonal anti-alpha-Tubulin (clone B-5-1-2)	Sigma-Aldrich	Cat# T6074; RRID:AB_477582
Mouse monoclonal anti-V5, HRP	Invitrogen	Cat# R961-25 (formerly 46-0708); RRID: AB_2556565
Rabbit polyclonal anti-V5	QED Bioscience	Cat# 18870-01; RRID:AB_215340
Mouse monoclonal anti-Myc (9B11)	Cell Signaling Technology	Cat# 2276 (also 2276S); RRID:AB_331783
Peroxidase-AffiniPure Goat Anti-Rabbit	Jackson ImmunoResearch Labs	Cat# 111-035-006; RRID:AB_2337936
Peroxidase-AffiniPure Goat Anti-Mouse	Jackson ImmunoResearch Labs	Cat# 115-035-003; RRID:AB_10015289
Peroxidase-AffiniPure Donkey Anti-Goat	Jackson ImmunoResearch Labs	Cat# 705-035-147; RRID:AB_2313587
Chemicals, peptides, and recombinant proteins		
1-Bromo-3-chloropropane	Sigma-Aldrich	Cat# B9673-200ml
4-Thiouridine	Abcam	Cat# ab143718
Blasticidin	Invivogen	Cat# ant-bl
DMEM, high glucose, GlutaMAX	Gibco	Cat# 61965059
DPBS	Gibco	Cat# 14190094
EGM Endothelial Cell Growth Medium BulletKit	Lonza	Cat# CC-3124
Fetal Bovine Serum, Value	Gibco	Cat# A5256701
GlycoBlue	Ambion	Cat# AM9515
GoScript Reverse Transcriptase	Promega	Cat# A5003
Hygromycin B Gold	Invivogen	Cat# ant-hg
Indole-3-acetic acid (IAA)	Sigma-Aldrich	Cat# I5148
Iodoacetamide	Sigma-Aldrich	Cat# I6125
Lipofectamine 2000	Invitrogen	Cat# 11668019
Lipofectamine RNAiMAX	Invitrogen	Cat# 13778150
McCoy's 5A (Modified) Medium, GlutaMAX	Gibco	Cat# 36600088
MEM NEAA	Sigma-Aldrich	Cat# M7145-100ml
MyTaq Red Mix	Meridian (Bioline)	Cat# BIO-25044
Penicillin-Streptomycin	Gibco	Cat# 15140163
Phire Direct PCR Kit	Thermo Fisher Scientific	Cat# F140WH
PrimeTime Gene Expression Master Mix	IDT	Cat# 1055772
Puromycin	Invivogen	Cat# ant-pr
Q5 High-fidelity DNA polymerase	NEB	Cat# M0491L
QuickExtract DNA Extraction Solution	Lucigen	Cat# QE09050
RNase I	Invitrogen	Cat# AM2295
RNasin RNase Inhibitor	Promega	Cat# N2515
SUPERase·In	Invitrogen	Cat# AM2696
TRI reagent	Oberacker et al.[154]	In-house prepared
Trizol LS	Invitrogen	Cat# 10296010
TRIzol Reagent	Invitrogen	Cat# 15596026
Turbo DNase	Invitrogen	Cat# AM2239
Critical commercial assays		
Direct-zol RNA MiniPrep kit	Zymo Research	Cat# R2052
Direct RNA Sequencing Kit	Oxford Nanopore Technologies	Cat# SQK-RNA004

(Continued on next page)

Please cite this article in press as: Boehm et al., Rapid UPF1 depletion illuminates the temporal dynamics of the NMD-regulated human transcriptome, Molecular Cell (2025), https://doi.org/10.1016/j.molcel.2025.08.015

Continued

REAGENT or RESOURCE	SOURCE	IDENTIFIER
Dynabeads mRNA Purification Kit	Invitrogen	Cat# 61006
ECL Select Western Blotting Detection Reagent	Cytiva	Cat# RPN2235
ERCC RNA Spike-In Mix	Invitrogen	Cat# 4456740
Iso-Seq Express 2.0 Kit	PacBio	Cat# 103-071-500
Kinnex Concatenation Kit	PacBio	Cat# 103-072-000
Microspin S-400 HR	Cytiva	Cat# 27-5140-01
NEBNext Poly (A) mRNA magnetic isolation module	New England Biolabs	Cat# E7490L
NEBNext Ultra II Directional RNA Library Prep Kit	New England Biolabs	Cat# E7760L
PacBio Revio 25M SMRT Cell	PacBio	Cat# 102-202-200
Pierce Detergent Compatible Bradford Assay Reagent	Thermo Fisher Scientific	Cat# 23246
PromethION RNA flow cell	Oxford Nanopore Technologies	Cat# FLO-PRO004RA
RNA Clean & Concentrator kit	Zymo Research	Cat# R1014
Western Lightning Plus-ECL	Perkin Elmer (now Revvity)	Cat# NEL103001EA
Deposited data		
phospho-UPF1 RIP-Seq from HEK293 cells	Kurosaki et al.[92]	GEO: GSE60045
Degradome-Seq from HeLa cells	Schmidt et al.[115]	GEO: GSE61398
UPF1 knockdown in HEK293 cells	Kishor et al.[83]	GEO: GSE109143
UPF1 knockdown in HeLa cells (total)	Longman et al.[84]	GEO: GSE152435
UPF1 knockdown in HeLa cells (cytoplasmic)	Longman et al.[84]	GEO: GSE152436
UPF1 knockdown in HEK293 cells	Fritz et al.[85]	GEO: GSE176197
UPF1 knockdown in K562 cells	Hug et al.[86]	GEO: GSE204987
UPF1 knockdown in Huh7 cells	Lee et al.[87]	GEO: GSE185655
UPF1 knockdown in HepG2 cells	He et al.[88]	GEO: GSE162199
SMG5, SMG6, SMG7 knockout/knockdown in HEK293 cells	Boehm et al.[26]	ArrayExpress: E-MTAB-9330
UPF3A/B double knockout in HEK293 cells	Wallmeroth et al.[155]	ArrayExpress: E-MTAB-10716
CASC3 knockout in HEK293 cells	Gerbracht et al.[156]	ArrayExpress: E-MTAB-8461
SMG6+SMG7 knockdown in HEK293, HeLa, MCF7 and U2OS cells	Britto-Borges et al.[69]	SRA: PRJNA105403
SMG1 inhibition in HCT116 cells	Kueckelmann et al.[82]	ArrayExpress: E-MTAB-13949
Initial Test-RNA-Seq of +/- IAA-treated HCT116 control, N-AID-UPF1 and C-AID-UPF1 cells	This paper	ArrayExpress: E-MTAB-13839
RNA-Seq of control and 0-48h IAA-treated N-AID-UPF1 in HCT116 cells	This paper	ArrayExpress: E-MTAB-13788
RNA-Seq of N-AID-UPF1 recovery for up to 48h after 24h IAA-treatment in HCT116 cells	This paper	ArrayExpress: E-MTAB-13789
RiboMinus RNA-Seq of control and 12h or 48h IAA-treated N-AID-UPF1 in HCT116 cells	This paper	ArrayExpress: E-MTAB-13787
RNA-Seq of FKBP-tagged UPF1 in Flp-In T-REx-293 and HCT116 cells +/- dTAG^V-1 treatment for 12h	This paper	ArrayExpress: E-MTAB-13829
SLAM-Seq of control and N-AID-UPF1 +/- IAA for 0, 12 and 24h	This paper	ArrayExpress: E-MTAB-13836
RNA-Seq of SMG1 inhibition in HUVEC and HFF cells	This paper	ArrayExpress: E-MTAB-14755
long-read RNA-Seq of IAA-treated N-AID-UPF1 in HCT116 cells with DirectRNA (ONT) and Kinnex full-length RNA kit (PacBio)	This paper	ArrayExpress: E-MTAB-14725

(*Continued on next page*)

Please cite this article in press as: Boehm et al., Rapid UPF1 depletion illuminates the temporal dynamics of the NMD-regulated human transcriptome, Molecular Cell (2025), https://doi.org/10.1016/j.molcel.2025.08.015

Continued

REAGENT or RESOURCE	SOURCE	IDENTIFIER
Ribo-Seq of N-AID-UPF1 in HCT116 +/- IAA for 12h	This paper	ArrayExpress: E-MTAB-13837
Raw and analyzed proteomic data	This paper	PRIDE: PXD061797
Original western blot and RT-PCR images	This paper	https://doi.org/10.17632/t9vzn5vwsz.1
Experimental models: Cell lines		
HCT116	ATCC	Cat# CCL-247; RRID:CVCL_0291
HCT116 pSH-EFIRES-P-AtAFB2-mCherry clone 1	This paper	N/A
HCT116 pSH-EFIRES-P-AtAFB2-mCherry UPF1-nterm BSD/Hygro P2A V5 AID7 (U1A3n2)	This paper	N/A
HCT116 pSH-EFIRES-P-AtAFB2-mCherry UPF1-cterm AID7-v5 P2A BSD/Hygro (U1D9c7)	This paper	N/A
HCT-116 FKBP12-UPF1, clone A2	This paper	N/A
Flp-In-T-REx-293	Thermo Fisher Scientific	Cat# R78007; RRID:CVCL_U427
Flp-In-T-REx-293 FKBP12-UPF1, clone 13	This paper	N/A
TERT-HFF	Ximbio	Cat# 154459
HUVEC/TERT 2	ATCC	Cat# CRL-4053; RRID:CVCL_9Q53
Oligonucleotides		
Primer, siRNA, sgRNA sequences	This paper	See Table S1
Recombinant DNA		
pSH-EFIRES-P-AtAFB2-mCherry	Addgene	Cat# 129716; RRID:Addgene_129716
pCas9-sgAAVS1	Addgene	Cat# 129726; RRID:Addgene_129726
pUC57-Kan-UPF1-N-term-AID-V5-P2A-BSD	Biocat	Gene synthesis
pUC57-Kan-UPF1-N-term-AID-V5-P2A-Hygro	Biocat	Gene synthesis
pUC57-Kan-UPF1-C-term-AID-V5-P2A-BSD	Biocat	Gene synthesis
pUC57-Kan-UPF1-C-term-AID-V5-P2A-Hygro	Biocat	Gene synthesis
pSpCas9(BB)-2A-GFP	Addgene	Cat# 48138; RRID:Addgene_48138
pCRIS-PITChv2	Addgene	Cat# 91796; RRID:Addgene_91796
pX330-BbsI-PITCh	Addgene	Cat# 127875; RRID:Addgene_127875
Software and algorithms		
Apeglm 1.22.1	Zhu et al.[157]	https://github.com/azhu513/apeglm
bakR 1.0.0	Vock and Simon[96]	https://github.com/simonlabcode/bakR
bam2bakR 2.0.0	Vock and Simon[96]	https://github.com/simonlabcode/bam2bakR
Bambu 3.2.6	Chen et al.[103]	https://github.com/GoekeLab/bambu
Boruta 8.0.0	Kursa and Rudnicki[127]	https://gitlab.com/mbq/Boruta/
Bowtie2 2.5.0	Langmead and Salzberg[158]	https://github.com/BenLangmead/bowtie2
CellScape	Silvestre-Ryan et al.[159]	https://github.com/jordisr/cellscape
ChimeraX 1.6.1	Pettersen et al.[160]	https://www.cgl.ucsf.edu/chimerax/
ComplexHeatmap 2.18.0	Gu et al.[161]	https://github.com/jokergoo/ComplexHeatmap
DESeq2 1.40.1	Love et al.[162]	https://github.com/thelovelab/DESeq2
DIA-NN 2.0	Demichev et al.[137]	https://github.com/vdemichev/DiaNN
edgeR 3.42.4	Robinson et al.[163]	https://bioconductor.org/packages/release/bioc/html/edgeR.html
ezBakR 0.0.0.9000	Vock et al.[164]	https://github.com/isaacvock/EZbakR
factR 1.2.0	Hamid et al.[165]	https://github.com/fursham-h/factR
fastq2EZbakR 0.2.0	Vock et al.[164]	https://github.com/isaacvock/fastq2EZbakR
Gffcompare 1.12.9	Pertea and Pertea[166]	https://ccb.jhu.edu/software/stringtie/gffcompare.shtml
gprofiler2 0.2.2	Kolberg et al.[167]	https://cran.r-project.org/web/packages/gprofiler2/index.html

(*Continued on next page*)

Please cite this article in press as: Boehm et al., Rapid UPF1 depletion illuminates the temporal dynamics of the NMD-regulated human transcriptome, Molecular Cell (2025), https://doi.org/10.1016/j.molcel.2025.08.015

Continued

REAGENT or RESOURCE	SOURCE	IDENTIFIER
IGV (Integrative Genomics Viewer) 2.14.1	Robinson et al.[168]	https://igv.org/
Image Lab 6.0.1	Bio-Rad	N/A
ImpulseDE2 0.99.10	Fischer et al.[90]	https://github.com/YosefLab/ImpulseDE2
InterProScan 5.72-103.0	Jones et al.[169]	https://www.ebi.ac.uk/interpro/
IsoformSwitchAnalyzeR 1.18.0	Vitting-Seerup and Sandelin[170]	https://github.com/kvittingseerup/IsoformSwitchAnalyzeR
IsoQuant 3.4.1	Prjibelski et al.[105]	https://github.com/ablab/IsoQuant
LeafCutter 0.2.9	Li et al.[171]	https://github.com/davidaknowles/leafcutter
minimap2 2.26-r1175	Li[172]	https://github.com/lh3/minimap2
MultiQC 1.14	Ewels et al.[173]	https://github.com/MultiQC/MultiQC
nVennR 0.2.3	Pérez-Silva et al.[174]	https://github.com/vqf/nVennR
ORFanage 1.2.0	Varabyou et al.[175]	https://github.com/alevar/ORFanage
ORFik 1.20.2	Tjeldnes et al.[176]	https://github.com/Roleren/ORFik
ORFquant 1.02.0	Calviello et al.[112]	https://github.com/lcalviell/ORFquant
PeptideRanger 0.1.0	Riley et al.[136]	https://github.com/rr-2/PeptideRanger
PolyASite 2.0	Herrmann et al.[177]	https://www.polyasite.unibas.ch/
refTSS v4.1	Abugessaisa et al.[178]	https://reftss.riken.jp/
R 4.3.0	R-project	https://www.r-project.org/
Ribo-TISH 0.2.7	Zhang et al.[113]	https://github.com/zhpn1024/ribotish
Ribo-seQC 0.99.0	Calviello et al.[97]	https://github.com/lcalviell/Ribo-seQC
RNAfold 2.6.4	Lorenz et al.[179]	https://github.com/ViennaRNA/ViennaRNA
Rrvgo 1.12.2	Sayols[180]	https://github.com/ssayols/rrvgo
Rsubread 2.14.2	Liao et al.[181]	https://bioconductor.org/packages/release/bioc/html/Rsubread.html
Salmon 1.9.0	Patro et al.[182]	https://github.com/COMBINE-lab/salmon
Spectronaut 19	Biognosys	https://biognosys.com/software/spectronaut/
Splam 1.0.12	Chao et al.[108]	https://github.com/Kuanhao-Chao/splam
SQANTI3 5.2	Pardo-Palacios et al.[107]	https://github.com/ConesaLab/SQANTI3
STAR 2.7.10b	Dobin et al.[183]	https://github.com/alexdobin/STAR
StringTie2 2.2.3	Kovaka et al.[104]	https://ccb.jhu.edu/software/stringtie/
Tximport 1.28.0	Soneson et al.[99]	https://github.com/thelovelab/tximport
UMI-tools 1.1.2	Smith et al.[184]	https://github.com/CGATOxford/UMI-tools

EXPERIMENTAL MODEL AND STUDY PARTICIPANT DETAILS

Cell culture

Flp-In T-REx-293 (human, female, embryonic kidney, epithelial; Thermo Fisher Scientific, cat. no. R78007; RRID:CVCL_U427) cells were cultured in high glucose DMEM with GlutaMAX supplement (Gibco) and HCT116 (human, male, colorectal carcinoma, epithelial; ATCC, cat. no. CCL-247; RRID:CVCL_0291) cells were cultured in McCoy's 5A (Modified) Medium with GlutaMAX supplement (Gibco) or 2 mM L-glutamine (Gibco). Media were supplemented with 9-10% fetal bovine serum (Gibco) and 1x Penicillin Streptomycin (Gibco). HFF (TERT-HFF; Ximbio Cat# 154459) cell lines were cultured in DMEM + 10% FBS, + 1% MEM Sigma, Cat# M7145-100ml) and HUVEC (HUVEC/TERT 2; ATCC Cat# CRL-4053; RRID:CVCL_9Q53) cell lines were cultured in EGM Endothelial Cell Growth Medium BulletKit (Lonza, Cat# CC-3124) supplemented with 10% FBS and 20 µg/ml G418. All cells were cultivated at 37°C and 5% CO2 in a humidified incubator. The generation of degron-tagged cell lines is described below and all cell lines are summarized in Table S1.

METHOD DETAILS

Protein structure modeling

The AlphaFold[185] structure prediction of UPF1 (AF-Q92900-F1-model_v4) was downloaded from the AlphaFold Protein Structure Database (AlphaFold DB, https://alphafold.ebi.ac.uk)[186] and overlayed in ChimeraX 1.6.1[160] with a crystal structure of a

Please cite this article in press as: Boehm et al., Rapid UPF1 depletion illuminates the temporal dynamics of the NMD-regulated human transcriptome, Molecular Cell (2025), https://doi.org/10.1016/j.molcel.2025.08.015

UPF1-RNA-ADP:AlF4$^-$ complex (PDB: https://doi.org/10.2210/pdb2XZO/pdb)[187] using the Matchmaker function to estimate RNA and ADP/ATP binding sites in the AlphaFold model. The final cartoon was generated using CellScape (https://github.com/jordisr/cellscape).[159]

Essentiality and loss-of-function data

The pan-cancer CRISPR Chronos scores (DepMap Public 23Q2+ Score, Chronos) were downloaded (https://depmap.org/portal/download/custom/)[47] on 2023-11-16 and the human population data on loss-of-function tolerance from gnomAD v4 (gnomad.v4.0.constraint_metrics.tsv) were downloaded from https://gnomad.broadinstitute.org/downloads on 2023-11-17. Both datasets were analyzed using R version 4.3.0. For additional analyses, the R package depmap (https://doi.org/10.18129/B9.bioc.depmap) was used with the DepMap Public 22Q2 data.

siRNA-mediated knockdowns

Cells were seeded at a density of 2.5 x 10^5 cells per well in a 6-well plate and reverse transfected with 2.5 µl Lipofectamine RNAiMAX and 60 pmol of the respective siRNAs according to the manufacturer's protocol. For the combined SMG6+SMG7 knockdown 30 pmol of both SMG6 and SMG7 siRNAs were used. All siRNAs used in this study are listed in Table S1.

Immunoblot analysis and antibodies

SDS-polyacrylamide gel electrophoresis and immunoblot analysis were performed using protein samples harvested with RIPA buffer (50 mM Tris/HCl pH 8.0, 0.1% SDS, 150 mM NaCl, 1% IGEPAL, 0.5% deoxycholate). For protein quantification, the Pierce Detergent Compatible Bradford Assay Reagent (Thermo Fisher Scientific) was used. All antibodies (see Table S1) were diluted in 50 mM Tris [pH 7.2], 150 mM NaCl with 0.2% Tween-20 and 5% skim milk powder. Detection was performed with Western Lightning Plus-ECL (PerkinElmer) or ECL Select Western Blotting Detection Reagent (Cytiva) and the Vilber Fusion FX6 Edge imaging system (Vilber Lourmat).

RNA extraction for low-throughput assays

Cells were harvested with 1 ml in-house prepared TRI reagent per 6 well[154] and RNA was isolated according to standard protocols. 150 µl 1-Bromo-3-chloropropane (Sigma-Aldrich) was used to induce phase separation and the washed RNA pellet was dissolved in 20 µl RNase-free water by incubating for 10 min on a shaking 65 °C heat block.

(Semi-)quantitative RT-PCR

Reverse transcription was performed with 0.75-2 µg of total RNA in a 20 µl reaction volume with either 10 µM VNN-(dT)20 primer (standard approach) or 0.5 µg random hexamers (for histone mRNAs) and the GoScript Reverse Transcriptase (Promega). 40-80 ng cDNA was used as template in end-point PCRs using the MyTaq Red Mix (Bioline) and 0.2 µM final concentration of sense and antisense primer. After 30 PCR cycles, the samples were resolved by electrophoresis on ethidium bromide-stained, 1% agarose TBE gels, visualized by trans-UV illumination using the Gel Doc XR+ (Bio-Rad) and quantified using the Image Lab software (version 6.0.1, Bio-Rad). Probe-based multiplex quantitative RT-PCRs were performed with the PrimeTime Gene Expression Master Mix (IDT), 2% of cDNA per reaction, and the CFX96 Touch Real-Time PCR Detection System (Bio-Rad). PrimeTime qPCR Assays containing primers and probes were purchased from IDT (B2M = Hs.PT.58v.18759587, ZFAS1 = Hs.PT.58.25163607, GAS5 = Hs.PT.58.24767969, H3-3A = NM_002107 Assay Set 4, H2AC18 = NM_003516 Assay Set 1, H1-2 = NM_005319 Assay Set 3) and used at 1x final concentration according to the manufacturer's instruction. Each biological replicate was repeated in technical triplicates and the average Ct (threshold cycle) value was measured. The housekeeping gene B2M (FAM-labelled) Ct values were subtracted from the target (ZFAS1, Cy5-labelled or GAS5, SUN-labelled) values to receive the ΔCt. For histone mRNAs, H3-3A (FAM-labelled) was used as control and H2AC18 (SUN-labelled) as well as H1-2 (Cy5-labelled) as targets. To calculate the mean log2 fold changes three biologically independent experiments were used. The log2 fold changes are visualized as single data points and mean (depicted as bars). All primers used in this study are listed in Table S1.

Whole proteome analysis

2.5 – 3.0 x 10^5 cells were seeded in 6-well plates one day before starting the depletion experiment. UPF1 depletion was induced with 500 µM indole-3-acetic acid (IAA; Sigma-Aldrich; Cat# I5148) or DMSO as control for various time points (between 0 and 24 hours before harvesting). All cells were harvested at the same time to minimize differences in cell numbers. Cells were washed twice with ice-cold Dulbecco's phosphate-buffered saline (DPBS; Gibco; Cat#14190-094) and then scraped in 2 mL of ice-cold DPBS. The cells were collected and pelleted (300 x g; 5 min; 4 °C), washed three times with ice-cold DPBS, transferred to a 96-well plate and frozen at -80 °C until further use.

The samples underwent lysis and digestion in SDC-buffer. Briefly, a pellet of one million HCT116 cells underwent lysis in 2x SDC-buffer comprising 2% (w/v) sodium deoxycholate (SDC; Sigma-Aldrich), 20 mM dithiothreitol (Sigma-Aldrich), 80 mM chloroacetamide (Sigma-Aldrich), and 200 mM Tris-HCl (pH 8). Following heating at 95°C for 10 minutes, the lysates underwent enzymatic

Please cite this article in press as: Boehm et al., Rapid UPF1 depletion illuminates the temporal dynamics of the NMD-regulated human transcriptome, Molecular Cell (2025), https://doi.org/10.1016/j.molcel.2025.08.015

digestion employing endopeptidase LysC (Wako) and sequence grade trypsin (Promega) at a protein:enzyme ratio of 50:1, with digestion occurring overnight at 37°C. The resulting peptides were desalted through automated pipetting facilitated by the AssayMAP Bravo robotic system (Agilent Technologies).

For reversed-phase liquid chromatography coupled with mass spectrometry (LC-MS) analysis, 1 μg of peptides from each sample replicate was injected. Samples from the 6, 12, and 24-hour time points were analyzed using the EASY-nLC 1200 system (Thermo Fisher Scientific), while a second batch of samples, including the 15 and 18-hour time points, was processed on the Vanquish Neo HPLC system (Thermo Fisher Scientific). Both batches used the same 98-minute active gradient for peptide separation. Mass spectrometric analysis was performed on an Exploris 480 instrument (Thermo Fisher Scientific) in data-independent acquisition (DIA) mode, using staggered 12 m/z isolation windows.

Label-free quantification was performed using Spectronaut (v19, Biognosys) with the directDIA workflow, applying default settings for Pulsar search and DIA analysis. Spectra were matched against the UniProt human database (release 2022-03), including isoforms, a curated set of distinct ORFs derived from the NMDRHT annotation and ORFquant prediction (see below and code sections), and common protein contaminants. Protein data were exported with decoy filtering and a Q value filter. For the initial dataset (Figure 1), analysis was conducted using only the UniProt human database (release 2022-03), common contaminants and first batch of samples (6, 12, and 24-hour time points).

As alternative analysis software package, DIA-NN (v2.0)[137] was used for analysis with a library-free search strategy. Search parameters allowed up to two missed cleavages and included variable modifications of oxidized methionine and acetylated N-termini, with a maximum of five variable modifications per peptide. The peptide length range was set to 7–52 amino acids, and charge states were restricted to 2–6 to align with the Spectronaut analysis. A precursor m/z range of 350–1650 was applied. A false discovery rate (FDR) threshold of 0.01 was enforced at the precursor level, and spectra were searched against the same databases used for Spectronaut. Peptidoform-level scoring was performed, and match-between-runs (MBR) was enabled. Peptide-level quantification was based on the report.parquet output, with the maximum Precursor.Normalised value for each unique peptide sequence used as its intensity in each run.

Protein-level analysis was conducted using R version 4.4.1. MaxLFQ-normalized intensities were log2 transformed and filtered to retain proteins with at least three valid value replicates per experimental group. Any remaining missing values were imputed using a randomized Gaussian distribution, with a down-shift (width = 0.3, shift = 1.8), based on empirically derived means and standard deviations from each replicate. Note that for the initial analysis (Figure 1) no imputation was applied. For differential abundance analysis, the limma package[188] was employed to compute two-sample moderated t-statistics. Nominal p-values were adjusted for multiple testing using the Benjamini-Hochberg method to control the false discovery rate. We considered proteins to be significantly differentially expressed at an adjusted p-value threshold of 0.001, with log fold change (logFC) values calculated to quantify expression differences between conditions.

Peptide analyses

Peptide data were exported from Spectronaut version 19 (Biognosys AG), utilizing MS2Quantity as the intensity metric for distinct peptide sequences. Peptides with intensity values less than or equal to 100 were replaced with "NA". No further normalization was applied; however, one outlier replicate (12h_Depl_A) was excluded before downstream analysis. For statistical analysis, peptide intensity values were log2-transformed. Peptides were filtered to retain those with more than 35% valid intensity measurements across all samples ($\geq$ 16 samples out of 43). This filtering step resulted in the retention of approximately 92% of all peptide sequences. To identify differentially expressed peptides, moderated analysis of variance (ANOVA) and F-tests were performed using the empirical Bayes method implemented in the R limma package.[188] Multiple testing corrections were applied using the Benjamini-Hochberg procedure to control the false discovery rate (FDR).

Prediction of theoretically possible tryptic peptides was performed using the R package "cleaver" with two distinct rule sets. Peptides from different ORF sources were compared and those exclusively found from NMD-annotated ORFs were designated as "NMD". Predicted peptide detectability was determined using PeptideRanger (version 0.1.0)[136] and the ProteomicsDB-trained random forest classifier.

Protein abundance and half-life data

The following data from published studies were used to assess protein abundance and half-lifes: HeLa cells (Supplemental Table 134915_1_supp_65961_p3f7xq of publication)[74] and 29 human tissues (Table EV5 of publication).[75] All datasets were analyzed using R version 4.3.0.

Generation of AtAFB2-expressing HCT116 cells

As parental cells for auxin-mediated degradation, HCT116 cells were generated to stably express the auxin receptor F-box protein AtAFB2 through integration into the adeno-associated virus integration site 1 (AAVS1) safe harbor locus by Cas9/CRISPR-mediated homologous recombination. 3.0×10^5 cells were seeded in a 24-well plate and transfected at 80–95% confluency using 4 μl Lipofectamine 2000 (Life Technologies) and 0.8 μg plasmids. Cells were co-transfected with pSH-EFIRES-P-AtAFB2-mCherry expressing the auxin receptor F-box protein and pCas9-sgAAVS1 at a ratio of 2:1. pSH-EFIRES-P-AtAFB2-mCherry (Addgene plasmid # 129716; http://n2t.net/addgene:129716; RRID:Addgene_129716) and pCas9-sgAAVS1-1 (Addgene plasmid # 129726; http://n2t.net/addgene:129726; RRID:Addgene_129726) was a gift from Elina Ikonen. After 2 days, the cells were transferred to a 10-cm dish and kept in medium containing 1 μg/mL puromycin (Invivogen, ant-pr) to select for successful AtAFB2 integration. After another 15 days with continuous medium change ever 3-4 days, individual colonies were picked, and transferred to a 96-well plate. Successful integration was tested by genomic PCR using Phire Direct PCR Kit (Thermo Fisher Scientific). Positive clones expressing AtAFB2-mCherry were subsequently expanded and used for subsequent generation of the UPF1-degron cell lines.

Endogenous tagging vectors

Degron tagging of endogenous loci was conducted by CRISPR–Cas9-mediated HDR. Donor vectors with two homology arms flanking the degron tag (AID = miniIAA7 = *At*IAA7 amino acids 37–104), and Cas9 vectors with specific sgRNAs were constructed for N- and C-terminal tagging of UPF1. For the N-terminal donor vector (UPF1 N-term AID in pUC57-Kan), homology arms were constructed by gene synthesis (Biocat) with around 500 bp upstream and downstream of the start codon. Between these homology arms cloning sites (XmnI and BglII) were also introduced, which were later used to insert a N-terminal tagging cassette with a selection marker and degron. The N-terminal tagging cassette [Blasticidin(BSD)/Hygromycin(Hygro)-P2A-V5-MiniIAA7(AID)] was synthesized with flanking restriction sites, XmnI and BamHI (see Figure 2A) in plasmid pUC57-Kan (Biocat). The C-terminal donor vector (UPF1 C-term AID in pUC57-Kan) was similarly synthesized as the N-terminal donor vector except that the homology arms were flanking the stop codon, which was completely replaced by cloning sites, NheI and SspI. The C-terminal tagging cassette (AID7-V5-P2A-BSD/Hygro) was also synthesized with these flanking restriction sites in the plasmid pUC57-Kan (see Figure 2A), respectively. To create the final targeting vector (N- and C-terminal), the donor vectors and the tagging cassette vectors were digested at their introduced restriction sites (see above). The restricted N- and C-terminal tagging cassette (BSD/Hygro-P2A-V5-AID and AID-V5-P2A-BSD/Hyg) was ligated to the digested donor vector (UPF1 N-term AID in pUC57-Kan and UPF1 C-term AID in pUC57-Kan), so that the tagging cassette was between the homology arms. This cloning procedure resulted in 4 targeting vectors (UPF1-N-term-AID-V5-P2A-BSD, UPF1-N-term-AID-V5-P2A-Hygro, UPF1-C-term-AID-V5-P2A-BSD, and UPF1-C-term-AID-V5-P2A-Hygro) which were used to tag endogenous loci of UPF1. SgRNAs were synthesized as two unphosphorylated primers, annealed and inserted into BbsI-cut px458-Cas9 vector. pSpCas9(BB)-2A-GFP (PX458) was a gift from Feng Zhang (Addgene plasmid # 48138; http://n2t.net/addgene:48138; RRID:Addgene_48138). Information about endogenous targets, HDR templates, primers for HDR templates and sgRNAs is provided in Table S1.

Generation of homozygously tagged cell lines

HCT116 cell-lines expressing AtAFB2 were used to create the UPF1-degron cell lines. The transfection was similar to the generation of HCT116 + AtAFB2 cell-line (see above). A cloned px458-Cas9 + sgRNA plasmid was co-transfected with two homology arm plasmids containing the mAID7-BSD/Hygro-resistance. Two days after transfection, the cells were transferred to a 10-cm dish containing 100 μg/mL hygromycin B Gold (Invivogen) and 5 μg/mL blasticidin (Invivogen) to select for successful AID7 (degron) integration. After two to three weeks of selection colonies were picked and transferred to 96 well plate. For successful biallelic integration clones were tested by genomic PCR using primers binding in the BSD/Hygro resistance sequence and the genomic region upstream of the homology arm (see “other sequences” in Table S1). Two single clones were selected for each target. The functionality of these cell clones was tested by inducing the degradation of the AID-tagged UPF1 by treatment with 500 μM indole-3-acetic acid (IAA; from 500 mM stock in H_2O; Sigma-Aldrich, cat. no. I5148) for 24h and subsequent Western Blot analysis with an anti-V5-HRP-antibody (Invitrogen, 46-0708). The sgRNAs, and primers for genomic PCR are listed in Table S1.

Knock-in cells using CRIS-PITCh v2

For FKBP12^{F36V}-tagging of UPF1, the knock-ins were performed using the CRIS-PITCh v2 system[189] consisting of a pX330-BbsI-PITCh encoding the gene specific sgRNA (5′-CCCGTACGCCTCCACGCTCA-3′) and the pCRIS-PITChv2-PurR-FKBP (UPF1 N) donor plasmid (based on Addgene #91796). pX330-BbsI-PITCh was a gift from Peter Kaiser (Addgene plasmid # 127875; http://n2t.net/addgene:127875; RRID:Addgene_127875) and pCRIS-PITChv2-dTAG-Puro (BRD4) was a gift from James Bradner & Behnam Nabet (Addgene plasmid # 91796; http://n2t.net/addgene:91796; RRID:Addgene_91796). The latter contains two 40 bp-long N-terminal UPF1 microhomologies flanking a puromycin resistance gene, a T2A signal, the FKBP12^{F36V} tag, and a linker region.

One day prior transfection 2.5 x 10^5 Flp-In T-REx-293 or HCT116 were seeded in 6-wells. Per well 1.0 μg of pX330-BbsI-PITCh and 0.5 μg pCRIS-PITChv2 donor plasmid were transfected using a calcium phosphate-based system with BES-buffered saline (BBS). Additionally, 0.1 μg of pCI-maxGFP was transfected as visual control for transfection efficiency. For BBS-transfection, HCT116 cells were temporarily cultured in high glucose DMEM with GlutaMAX supplement (Gibco). Two days after transfection, the cells were transferred to a 10-cm dish. After a total of 3-5 days post transfection the cell culture medium was supplemented with 2 μg/ml or 1.5 μg/ml puromycin (InvivoGen) for the Flp-In T-REx-293 and HCT116 cell, respectively, to select for successful knock-ins. Surviving colonies were picked and genomic DNA was extracted using QuickExtract DNA Extraction Solution (Lucigen) according to manufacturer’s instruction. Correct integration was screened via genomic PCR, followed by Sanger sequencing (Eurofins Genomics). The sgRNAs, and primers for genomic PCR are listed in Table S1.

Please cite this article in press as: Boehm et al., Rapid UPF1 depletion illuminates the temporal dynamics of the NMD-regulated human transcriptome, Molecular Cell (2025), https://doi.org/10.1016/j.molcel.2025.08.015

Public high-throughput-sequencing data

Publicly available RNA-Seq datasets were obtained from Gene Expression Omnibus (GEO)[190] or BioStudies/ArrayExpress[191,192] with accession IDs as detailed in Table S1. These included phospho-UPF1 RIP-Seq from HEK293 cells[92] (GEO: GSE60045); Degradome-Seq from HeLa cells[115] (GEO: GSE61398); UPF1 knockdown in HEK293 cells[83] (GEO: GSE109143); UPF1 knockdown in HeLa cells[84] (GEO: GSE152435); UPF1 knockdown in HEK293 cells[85] (GEO: GSE176197); UPF1 knockdown in K562 cells[86] (GEO: GSE204987); UPF1 knockdown in Huh7 cells[87] (GEO: GSE185655); UPF1 knockdown in HepG2 cells[88] (GEO: GSE162199); SMG5, SMG6, SMG7 knockout/knockdown in HEK293 cells[26] (BioStudies: E-MTAB-9330); UPF3A/B double knockout in HEK293 cells[155] (BioStudies: E-MTAB-10716); CASC3 knockout in HEK293 cells[156] (BioStudies: E-MTAB-8461) and SMG6+SMG7 knockdown in HEK293, HeLa, MCF7 and U2OS cells[69] (Sequence Read Archive (SRA): PRJNA105403). Available data from the preprint on SMG1 inhibition in HCT116 cells[82] (BioStudies: E-MTAB-13949) were used as well.

Generated high-throughput-sequencing data

Different high-throughput sequencing datasets were generated in this study as listed in Table S1: #11) Initial Test-RNA-Seq of +/- IAA-treated HCT116 control, N-AID-UPF1 and C-AID-UPF1 cells, #12) RNA-Seq of control and 0-48h IAA-treated N-AID-UPF1 in HCT116 cells, #13) RNA-Seq of N-AID-UPF1 recovery for up to 48h after 24h IAA-treatment in HCT116 cells, #14) RiboMinus RNA-Seq of control and 12h or 48h IAA-treated N-AID-UPF1 in HCT116 cells, #15-16) RNA-Seq of FKBP-tagged UPF1 in Flp-In T-REx-293 and HCT116 cells +/- dTAG^{V}-1 treatment for 12h, #17) SLAM-Seq of control and N-AID-UPF1 +/- IAA for 0, 12 and 24h, #19-20) RNA-Seq of SMG1 inhibition in HUVEC and HFF cells, #25-26) long-read RNA-Seq of IAA-treated N-AID-UPF1 in HCT116 cells with DirectRNA (ONT) as well as Kinnex full-length RNA kit (PacBio), and #27) Ribo-Seq of N-AID-UPF1 in HCT116 +/- IAA for 12h.

For datasets #11, #19 and #20, total RNA was extracted by lysing cells with TRIzol Reagent (Invitrogen). Libraries were constructed using the NEBNext Ultra II Directional RNA Library Prep Kit (New England Biolabs) and sequenced on a NovaSeq6000 device (Illumina). For datasets #12-16, cells were lysed using 1 ml in-house prepared TRI reagent per 6 well.[154] The RNA was extracted and purified using the Direct-zol RNA MiniPrep kit including the recommended DNase I treatment (Zymo Research; Cat# R2052) according to manufacturer's instructions. For datasets #12-13, libraries were prepared using the Illumina Stranded TruSeq RNA sample preparation kit. Library preparation started with 500ng total RNA. After poly-A selection (using poly-T oligo-attached magnetic beads), mRNA was purified and fragmented using divalent cations under elevated temperature. The RNA fragments underwent reverse transcription using random primers, followed by second strand cDNA synthesis with DNA Polymerase I and RNase H. After end repair and A-tailing, indexing adapters were ligated. The products were then purified and amplified (15 cycles) to create the final cDNA libraries. After library validation and quantification (Agilent Tape Station), equimolar amounts of library were pooled. The pool was quantified by using the Peqlab KAPA Library Quantification Kit and the Applied Biosystems 7900HT Sequence Detection System. The pool was sequenced on an Illumina NovaSeq6000 sequencing instrument with a PE100 protocol aiming for 75 million clusters per sample. Libraries for dataset #14 were prepared from 500ng total RNA. Enzymatic depletion of ribosomal RNA with the Illumina Ribo-Zero Plus rRNA Depletion Kit was followed by library preparation with the Illumina® Stranded Total RNA sample preparation kit. The depleted RNA was fragmented and reverse transcribed with random hexamer primers, second strand synthesis with dUTPs was followed by A-tailing, adapter ligation and library amplification (12 cycles). Next library validation and quantification (Agilent Tape Station) was performed, followed by pooling of equimolar amounts of library. The pool itself was then quantified using the Peqlab KAPA Library Quantification Kit and the Applied Biosystems 7900HT Sequence Detection System and sequenced on an Illumina NovaSeq6000 sequencing instrument with an PE100 protocol aiming for 100 million clusters per sample. Libraries for datasets #15-16 were prepared from 500ng total RNA with the Illumina Stranded mRNA Preparation kit. After poly-A selection (using Oligo (dT) magnetic beads), mRNA was purified, fragmented and reverse transcribed with random hexamer primers. Second strand synthesis with dUTPs was followed by A-tailing, adapter ligation and library amplification (12 cycles) to create the final cDNA libraries. After library validation and quantification (Agilent Tape Station), equimolar amounts of library were pooled. The pool was quantified by using the Peqlab KAPA Library Quantification Kit and the Applied Biosystems 7900HT Sequence Detection System. The pool was sequenced on an Illumina NovaSeq6000 sequencing instrument with a PE100 protocol aiming for 75 million clusters per sample.

For dataset #16, thiol modification was performed as previously described.[94] Shortly, we mixed 1 μg of RNA with 10 mM Iodoacetamide (Sigma-Aldrich; Cat#I6125), 50 mM $NaPO_4$ (pH 8) and 50 % DMSO. The reaction was performed at 50°C for 15 minutes, protected from light. Alkylation was quenched with 20mM DTT. RNA was precipitated by adding 2.5 volumes of 100% EtOH and 1 μg GlycoBlue (Ambion; Cat# AM9515) and incubating -80°C for 30 minutes. After cold centrifugation at 16,000 x g for 30 minutes, the pellet was washed with 75% EtOH, re-centrifuged for 10 minutes, air-dried for 5-10 minutes, and resuspended in 5-10 μl of H2O. Poly (A) mRNA isolation and library preparation was carried out with 500 ng RNA as input using the NEBNext Poly (A) mRNA magnetic isolation module (NEB; Cat#E7490L) and NEBNext Ultra II Directional RNA library preparation kit (NEB; Cat#E7760L) according to the manufacturer's instructions.

For dataset #25 (ONT-dRNA) total RNA was extracted using the Direct-zol RNA MiniPrep kit (Zymo Research; Cat# R2052) including the recommended DNase I treatment according to the manufacturer's instructions. Poly(A) mRNA was purified from total RNA using the Dynabeads mRNA Purification Kit (Invitrogen; Cat#61006). After one round of purification according to the manufacturer's instruction, the samples were incubated for a second round of binding to the same beads, repeating the protocol for a second time after the rebinding of the RNA to the beads. Successful enrichment for poly(A) RNA was confirmed by High Sensitivity RNA

Please cite this article in press as: Boehm et al., Rapid UPF1 depletion illuminates the temporal dynamics of the NMD-regulated human transcriptome, Molecular Cell (2025), https://doi.org/10.1016/j.molcel.2025.08.015

ScreenTape Analysis. ONT direct RNA sequencing libraries were prepared from 300 ng of poly(A) RNA using the Direct RNA Sequencing Kit (Oxford Nanopore Technologies, #SQK-RNA004) following the manufacturer's instructions. Each ONT direct RNA sequencing library was loaded onto a PromethION RNA flow cell (Oxford Nanopore Technologies, #FLO-PRO004RA). Run limit was set to 72 hours, base-calling was performed with the High-accuracy model (130 bps) with the following software versions: MinKNOW (24.02.19), Bream (7.9.8), Configuration (5.9.18), Dorado (7.3.11), MinKNOW Core (5.9.12).

For dataset #26 (PacBio) total RNA was extracted using the Direct-zol RNA MiniPrep kit (Zymo Research; Cat# R2052) including the recommended DNase I treatment according to the manufacturer's instructions. The PacBio Kinnex full-length RNA sequencing library was constructed from four total RNA samples. First, each sample was processed into a PacBio barcoded Iso-Seq library, starting with 420 ng of total RNA and using the Iso-Seq Express 2.0 Kit (PacBio, #103-071-500). Then, 14 ng of each Iso-Seq library was additionally amplified to introduce Kinnex overhangs at the ends of the library molecules and pooled together to prepare one Kinnex library using the Kinnex Concatenation Kit (PacBio, #103-072-000). The Kinnex full-length RNA library was loaded onto a PacBio Revio 25M SMRT Cell (PacBio, #102-202-200). Desegmentation and demultiplexing of HiFi reads were performed using SMRT Link Version 13.1.0.221970. Generation of dataset #27 (Ribosome profiling) is described below in more detail.

For datasets #12-15 the ERCC RNA Spike-In Mix (Invitrogen, Cat# 4456740) were added to the samples before library preparation to provide a set of external RNA controls that enable performance assessment. The Spike-Ins were used for quality control purposes but not used for the final analyses.

Computational analyses of RNA-Seq data

For standard short-read RNA-Seq analyses, reads were aligned against the human genome (GRCh38, GENCODE release 42 transcript annotations[15] supplemented with SIRVomeERCCome annotations from Lexogen; obtained from https://www.lexogen.com/sirvs/download/) using the STAR read aligner (version 2.7.10b).[183] For long-read RNA-Seq data, reads were aligned against the human genome as described above using the minimap2 read aligner (version 2.26-r1175)[172] and the options "ax splice:hq -C5" for PacBio or "-ax splice -k14 -uf" for ONT-dRNA samples.

Transcript abundance estimates were computed with Salmon (version 1.9.0)[182] in mapping-based mode using a decoy-aware transcriptome (GENCODE release 42 or NMDRHT; see below) with the options --numGibbsSamples 30 --useVBOpt --gcBias --seqBias. After the import of transcript abundances in R (version 4.3.0)[193] using tximport (version 1.28.0),[99] differential gene expression (DGE) analysis was performed with the DESeq2 R package (version 1.40.1).[162] Genes with less than 10 counts in half the analyzed samples were pre-filtered and discarded. The DESeq2 log2FoldChange estimates were shrunk using the apeglm R package (version 1.22.1).[157] Differential transcript expression (DTE) analysis was performed using the edgeR R package (version 3.42.4),[100,163] accounting for mapping ambiguity by estimating the overdispersion based on 30 inferential replicate datasets drawn by Salmon using Gibbs sampling and subsequent count scaling. Lowly expressed transcripts were pre-filtered using the edgeR-internal functions. General significance cutoffs, as long as not indicated otherwise, were log2FoldChange > 1 & padj < 0.0001 for DESeq2 DGE and log2FC > 1 & FDR < 0.0001 for edgeR DTE.

To assess technical metrics for each RNA-Seq dataset, MultiQC (version 1.14)[173] was used to aggregate the output of Salmon (total reads, alignment rate, library type) and Bowtie2 (version 2.5.0)[158] (rRNA alignment rate). Non-poly(A) RNA genes were chosen based on published results[194] and Swish[195] was used to obtain log10-scaled expression values. Differential splicing was detected with LeafCutter (version 0.2.9)[171] with the significance threshold adjusted p-value (p.adjust) < 0.0001. Differential transcript usage was computed with IsoformSwitchAnalyzeR (version 1.18.0)[170] and the DEXSeq method.[188,196] Significance thresholds were |dIF| > 0.1 and adjusted p-value (isoform_switch_q_value) < 0.0001. Clustering of Z-scaled log2-transformed counts (obtained by variance stabilizing transformation for gene-level and edgeR::cpm for transcript-level) was performed with "ward.D2" hierarchical clustering with k = 4, as determined by elbow method.

Degradome-Seq data were subjected to adapter trimming and mapped with modified parameters (adopted from[197]) against the human genome with STAR as described above. Reads in a 200-nucleotide window around the stop codon were counted with ORFik (version 1.20.2)[176] and analyzed with edgeR. RIP-Seq reads from phospho-UPF1[92] were adapter-trimmed, filtered for ≥ 15 nucleotides and aligned against rRNA, tRNA, miRNA and snoRNA. The unaligned reads were mapped with STAR as described above and reads counted with featureCounts from the Rsubread package (version 2.14.2).[181] Final analysis was performed with DESeq2.

Analysis of SLAM-seq data

Reads were mapped with STAR as described above and used as input for bam2bakR (version 2.0.0)[95,96] to detect T-to-C mutations in mapped reads. The counts binomial data frame output was used for further analysis with bakR (version 1.0.0). The 'Stan' model was used to estimate mutation rates, followed by using the 'Hybrid' implementation to fit the data and perform differential kinetic analysis. The mechanistic dissection of gene expression regulation was performed with bakR combined with DESeq2 using the 'DissectMechanism' function. Three layers of basal conclusions were determined: a) degradation (k_{deg}) rates (significance cutoffs bakR_padj < 0.01 & |L2FC_kdeg| > 1), b) RNA expression levels (significance cutoffs DE_padj < 0.01 & |L2FC_RNA| > 1) and mechanistic conclusion (significance cutoffs mech_padj < 0.01). For final classification the following parameters were used: Stabilized (bakR_padj < 0.01 & L2FC_kdeg < -1 & DE_padj < 0.01 & L2FC_RNA > 1 & mech_padj < 0.01 & Mech_score < 0); Destabilized (bakR_padj < 0.01 & L2FC_kdeg > 1 & DE_padj < 0.01 & L2FC_RNA < -1 & mech_padj < 0.01 & Mech_score < 0); Increased Synthesis (not significant kdeg changes & DE_padj < 0.01 & L2FC_RNA > 1 & mech_padj < 0.01 & Mech_score > 0) and Decreased Synthesis (not significant kdeg changes & DE_padj < 0.01 & L2FC_RNA < -1 & mech_padj < 0.01 & Mech_score > 0).

For NMDRHT-transcript-level analyses (specifically for analyses on transcript equivalence classes; TEC), the EZbakR suite was used.[164] Reads were first processed with fastq2EZbakR (version 0.2.0) using the NMDRHT.v1.1 annotation as reference. The counts binomial data frame output was used for further analysis with EZbakR (version 0.0.0.9000) as detailed by the authors.[198] When estimating isoform fractions, a minimum TPM of 0.2 (instead of default 1) was set to include more NMD-annotated isoforms which are lowly expressed in control conditions.

Ribosome profiling

Ribo-Seq libraries were generated as previously described[199] with some modifications. N-AID-UPF1 HCT116 cells were treated with 500 μM IAA for 12 hours or were untreated (control). Afterwards, the cells were washed with PBS containing 100 μg ml^{-1} cycloheximide (Biochemika) before cell lysis. Samples were lysed in polysome buffer (100 mM Tris-HCl pH 7.4, 750 mM NaCl, 25 mM $MgCl_2$, 1 mM dithiothreitol (DTT), 1% Triton X-100, 100 μg ml^{-1} cycloheximide and 25 U ml^{-1} Turbo DNase (Thermo Fisher Scientific)) and directly frozen in liquid nitrogen. RNA was then digested with 2400 U ml^{-1} RNase I (Ambion) for 45 min in slow agitation at RT and digestion stopped with 640 U ml^{-1} SUPERase·In (Thermo Fisher Scientific). Monosomes were purified by size exclusion with Illustra MicroSpin S-400 HR columns (GE Healthcare) and extracted with 3 volumes of Trizol LS (Thermo Fisher Scientific), chloroform and the RNA Clean & Concentrator kit (Zymo Research). 5000 ng of the isolated monosomes were depleted of rRNA using a RiboPool kit for Ribosome Profiling (siTOOLs Biotech). The RNA was separated on a 17% Urea PAA gel, 27–30 nt RNA fragments were eluted from the gel and 5′ extremity phosphorylated with 10 U T4 polynucleotide kinase (New England Biolabs) for 1 h at 37 °C. For library generation, the NextFlex small RNA sequencing kit (PerkinElmer) was used according to the manufacturer's instructions. Each Ribo-seq library was prepared in triplicate and sequenced on a NovaSeq6000 device (Illumina) in two batches.

Ribo-Seq reads from both sequencing batches were combined, demultiplexed, adapter-trimmed, UMIs (random 4 bases at the 5′ and 3′ ends) extracted with UMI-tools (version 1.1.2),[184] length-filtered ($\geq$ 16 & $\leq$ 40 nts) and mapped with Bowtie2 (version 2.5.0)[158] against human rRNA, tRNA, miRNA and snoRNA. Unaligned reads were mapped with STAR as described above and mapped reads deduplicated with UMI-tools. Gene-level counts were computed with featureCounts from the Rsubread package (version 2.14.2)[181] and DESeq2 used for differential ribosome occupancy analysis. Translation efficiency was calculated with DESeq2 using the deltaTE method as described.[200] Classification was as follows: Concordant-up (padj_Ribo < 0.01 & padj_RNA < 0.0001 & L2FC_RNA*L2FC_Ribo > 0 & L2FC_RNA > 1); Concordant-down (padj_Ribo < 0.01 & padj_RNA < 0.0001 & L2FC_RNA*L2FC_Ribo > 0 & L2FC_RNA < -1); Discordant_up (padj_TE < 0.01 & L2FC_TE > 1); Discordant_down (padj_TE < 0.01 & L2FC_TE < -1). Quality control of Ribo-Seq reads was performed with Ribo-seQC (version 0.99.0)[97] and ORFquant (version 1.02.0)[112] used on condition-merged files for splice-aware quantification of translation. Alternatively, Ribo-TISH (version 0.2.7) was used to predict ORFs.

Gene ontology

Functional enrichments analysis of gene lists (for SLAM-seq ordered by p.adjust(ksyn)) was performed using g:profiler via the R package gprofiler2 (version 0.2.2),[167] using gene ontology biological process (GO:BP) as data source, a list of all expressed/detected genes as custom background, domain scope set to 'custom' and with g:SCS multiple testing correction method applying significance threshold of 0.05. If applicable, significant GO:BP terms were simplified using rrvgo (version 1.12.2).[180]

Time course analysis

ImpulseDE2 (version 0.99.10)[90] was used for the time course analysis of differential gene expression with default parameters. The option to identify transient expression changes was enabled and parameters for impulse and sigmoid models were extracted.

Histone mRNA analyses

The list of histone genes was obtained from the HUGO Gene Nomenclature Committee at the European Bioinformatics Institute (https://www.genenames.org/data/genegroup/#!/group/864), as previously defined[201] and matched using Ensembl gene IDs.

NMDRHT - transcriptome assembly

Mapped long-read RNA-Seq data were subjected to GENCODE-guided or de novo transcriptome assembly using bambu (version 3.2.6),[103] IsoQuant (version 3.4.1)[105] and StringTie2 (version 2.2.3).[104] To maximize transcript discovery, the novel discovery rate (NDR) for bambu was set to 1. For StringTie2, the condition matching Illumina short-read RNA-Seq data were provided as well and assembly was performed with the "—mix" option. Mapped short-read RNA-Seq data from nine datasets (combining all conditions within) to supplement transcript annotations from other cell lines, NMD-inhibition methods, or library preparations were also assembled guided or de novo using StringTie2. The resulting individual transcriptome assemblies were analyzed by SQANTI3 (version 5.2)[107] for quality control and statistics. Common abbreviations are full-splice match (FSM): matches all reference splice junctions perfectly; novel in catalog (NIC): novel isoform with a new combination of annotated splice sites; novel not in catalog (NNIC): novel isoform with at least one new splice site. Gffcompare (version 1.12.9)[166] was used to compare all transcriptome assemblies and identify unique intron chains (UIC). Transcripts found in at least two assemblies (UIC support $\geq$ 2) were further processed.

Please cite this article in press as: Boehm et al., Rapid UPF1 depletion illuminates the temporal dynamics of the NMD-regulated human transcriptome, Molecular Cell (2025), https://doi.org/10.1016/j.molcel.2025.08.015

A two-phase gene-wise filtering strategy was used to first select UICs from well-supported genes (high filter level; total UIC support $\geq$ 4), followed by otherwise missed genes with low-supported UICs (low filter level; total UIC support $\geq$ 2). The locus ID assigned by gffcompare was used as gene identifier and for each gene only transcripts with UIC support higher than the gene-wise mean UIC support were selected. This strategy resulted in removing low-support transcripts from genes for which high-support transcripts were found. As the individual transcriptomes differed in transcript boundaries, we performed majority voting on transcript start sites and transcript end sites, favoring de novo assembled and long-read-supported transcripts.

To recover ORF information, we used ORFanage (version 1.2.0)[175] in mode "ALL" and provided the ensemble-canonical ORFs as reference for ORF recovery. The recovered ORF coordinates were matched with the canonical ORF, filtered for best matching ORFs per transcript and start/stop codons characterized. Finally, the 50-nucleotide rule as predictor for NMD-sensitivity was determined by using factR (version 1.2.0)[165] and the resulting annotation exported as NMDRHT.v1.1.

For further supplementation of Ribo-Seq-supported ORFs, ORFquant and Ribo-TISH ORF prediction was performed using the NMDRHT.v1.1 annotation as reference. ORFquant output was expanded to include all "compatible" transcripts per predicted ORF and the overlap with Ribo-TISH was determined. For NMDRHT-supplementation, only ORFs found in both tools were selected. Based on the 50-nucleotide rule, ORF category determined by ORFquant and the relationship between predicted and canonical start/stop codons, the NMD reason was determined. For example, if the predicted stop codon is located more than 50 nucleotides upstream of the last exon-exon junction, the ORF was already annotated and the start/stop codon match the ensemble-canonical ORF, a 3′UTR splicing event occurred and NMD reason is consequently set to "AS_NMD_UTR3".

Since multiple ORFs can be predicted for an individual transcript, we determined the best high-quality ORF per transcript. We considered all ORFs from untreated (0h) and UPF1-depleted conditions (12h IAA) and determined the fraction of ORF-length-normalized P-site counts stratified by the 50-nucleotide rule. The rationale was to determine whether all predicted ORFs are NMD-sensitive or -insensitive, which allowed designating this transcript with the ORF status "NMD" or "coding", respectively. When both NMD-activating and -insensitive ORFs were found, we designated the transcript ORF status "mixed". Finally, we determined the most frequently used ORF per transcript based on ORF-length-normalized P-site counts, favoring NMD-activating ORFs in mixed ORF status cases. The NMDRHT annotation was supplemented with these ORFs, replacing the previously existing ORFanage-predicted ORFs when applicable. The resulting NMDRHT.v1.2 annotation was exported.

For quality control, splam (version 1.0.12)[108] was used on the GENCODE v42 and NMDRHT.v1.2 annotation to estimate splice site confidence. Distances between TSS/TES and references (refTSS v4.1 and PolyASite 2.0)[177,178] were used to judge the accuracy of transcript boundaries. InterProScan (version 5.72-103.0)[169] was used to predict Pfam domains or intrinsically disordered regions.

RNA properties and structure prediction

Most mRNA isoform properties were extracted from the NMDRHT.v1.2 annotation and reference genome using R packages. Structure prediction was performed using RNAfold (version 2.6.4).[179]

Additional data sources

Data from a previous NMD factor meta-analysis was downloaded (Table S2 from publication)[67] and matched via Ensembl gene IDs. Similarly, the data from STAU1 hiCLIP were obtained (Table S2 from publication)[118] and matched via Ensembl gene IDs.

UPF1 helicase-dependent targets (Table S1 from Fischer et al., 2020)[55] and REG-1 RIP-Seq data (Table S1 from publication)[117] were matched to ensembl transcript IDs using bioMart and manually curated to allow matching NMDRHT-transcripts. Coordinates of REG-1 HITS-CLIP data (Table S4 from Mino et al., 2015)[117] were lift over to hg38 and intersected with NMDRHT transcripts.

Feature selection

The Boruta R package (version 8.0.0)[127] was used to perform feature selection. For details, see the corresponding script section.

Data Presentation

Schematic representations and figures were prepared/assembled using CorelDraw 2017. Quantifications and calculations for other experiments were performed - if not indicated otherwise - with R (version 4.3.0) and all plots were generated using IGV (version 2.14.1),[168] ggplot2 (version 3.5.1),[202] nVennR (version 0.2.3)[174] or ComplexHeatmap (version 2.18.0).[161]

QUANTIFICATION AND STATISTICAL ANALYSIS

Most performed statistical tests are already implemented in the used bioinformatic tools. For differential gene expression (DGE) analysis, p-values were calculated by DESeq2 using a two-sided Wald test and corrected for multiple testing using the Benjamini-Hochberg method. For differential transcript expression (DTE) analysis, p-values were either calculated by Swish using a Mann–Whitney Wilcoxon test on inferential replicate count matrices and corrected for multiple testing using q-value approaches or by edgeR using quasi-likelihood F-tests. P-values were calculated for differential transcript usage (DTU) analysis by IsoformSwitchAnalyzeR using a DEXSeq-based test and corrected for multiple testing using the Benjamini-Hochberg method. For alternative splicing, p-values were calculated by LeafCutter using an asymptotic Chi-squared distribution and corrected for multiple testing using the Benjamini-Hochberg method. For differential kinetic analysis, p-values were calculated by bakR using a z-test and corrected for multiple testing using the Benjamini-Hochberg method. Other statistical tests performed independently of bioinformatic tools used either the R package rstatix or the limma package. Used cutoffs are described in the figures, figure legends or method section.

ADDITIONAL RESOURCES

We provide an interactively explorable web application based on igv.js at https://nmdrht.uni-koeln.de.